Bone Fracture Analysis of Diseased Femurs using CT-Image Based Finite Element Method

ゾウ, リン, タン

Bone Fracture Analysis of Diseased Femurs using CT-Image Based Finite Element Method

PhD Thesis

Submitted as partial fulfillment of the requirements for the degree

Doctorate of Philosophy

by

Zaw Linn Htun

3ES19117Y

Department of Molecular and Material Sciences

Interdisciplinary Graduate School of Engineering Sciences

Kyushu University

Japan

2022

ACKNOWLEDGEMENTS

First and foremost, I am extremely grateful to my supervisor, Associate Professor Dr. Mitsugu Todo, for allowing me to join his excellent lab and work on fascinating projects for the past three and half years. His contribution of knowledge and skills to me, his guidance throughout my study in Japan, are invaluable, and I will never forget his endless patience and support.

I would also like to offer my special thanks to the senior students of my laboratory for taking care of me since I arrived in Japan, and answering my endless questions; Mr. Kisaki Chihiro, Mr. Wu Shun, Ms. Kurita Hiroko, Mr. Hishyam, Mrs. Fatin and all the others. My thanks also go to the other lab members, who always assist at every stage of the research project and give advice; Mr. Bou, Mr. Aiman, Mr. Kakoi and everyone else. I would also like to thank Mr. Hayashi Daigo for his technical support on my study.

Without any support of Japan International Cooperation Agency (JICA) and ASEAN University Network/ Southeast Asia Engineering Education Development Network (AUN/SEED-Net), I would never have been able to come to Japan and conduct this research, and my life here. I am deeply thankful to JICA and AUN/SEED-net for offering the educational programs and financial support. I also would like to express my enormous thanks to our program officer, Ms. Sakono Akiko and all the others for their tireless support.

I would like to extend my sincere thanks to the staff and student members of the Kyushu University IGSES International Students Association, who have played an

enormous role in my university student life since entering Chikushi campus. Without their kind support and friendship, my study here may never have been complete. Thank you to Ms. Kojima, Ms. Nishiyama, Ms. Morikawa and everyone else who freely gave their time and energy to me.

I also like to unforgettably thank to my elementary teachers; Daw Aye Aye Myint and others, my university teachers; Associate Professor Dr. Lwin Lwin Than, Associate Professor Daw Lian Tial and others, my master degree supervisors; Professor Dr. Ahmad Fauzi Bin Mohd Noor and Professor Dr. Aye Aye Thant, for caring, guiding and inspiring me. Thank you indeed, all of you, for believing in me and giving me wings to soar.

Lastly, I would like to express my gratitude to my parents, my wife and my son. Without their tremendous understanding and encouragement, it would be impossible for me to complete my study.

Thank you very much!

Zaw Linn Htun

May 2022

ABSTRACT

Hip fracture has been considered as a high risk of morbidity and mortality in elderly patients. Recent years, the risk of hip fractures in elderly people has exponentially increased due to a progressive loss of bone mass and bone structure deterioration due to osteoporosis and increased incidental falls. Therefore, the prediction of femoral strength and fracture location of specific patient will be clinically very useful. It is also considered that some typical femoral diseases such as osteoarthritis (OA) and avascular necrosis (AVN) could also affect the strength and fracture behaviour of the femurs. Dual-energy X-ray absorptiometry (DEXA) and other diagnostic imaging methods have generally been used to predict the risk of bone fracture. However, these methods cannot provide a quantitative strength which is directly related to the fracture risk of the femur because the femoral strength depends on its three-dimensional (3D) geometry, heterogeneity, distributed mechanical properties, and loading conditions. To address these limitations, the computed tomography image based finite element method (CT-FEM) was utilized to estimate the mechanical strength of femurs in order to assess the hip fracture risk. The background of DEXA and the benefits of CT-FEM were fully explained in Chapter 1.

In Chapter 2, 130 computational femoral models were constructed using CT images of 73 patients and classified into three groups; the normal (contralateral) femora, the OA femora and the AVN femora. Then, CT-FEM combined with a damage mechanics analysis was applied to predict the fracture load as the femoral strength and the fracture location of the femoral models. Mechanical Finder v.11 software was used to simulate the models with regard to stance configuration. For each of the femoral models,

the average volumetric BMD (vBMD) in the femoral head and neck region was obtained as it has a strong correlation with the femoral strength. After a linear regression was fitted on the data, Pearson's correlation coefficient was found to be r = 0.71, 0.60 and 0.49 for the normal, OA and OA groups, respectively, indicating a high linear correlation between vBMD and resulted fracture load. Confidence interval (CI) statistics was also performed to precisely estimate the samples' mean and it was found that the average means of 95% confidence intervals were 3,590±675 N (mean±SD), 3,573±496 N and 3,734±744 N for the normal, OA and AVN models, respectively. In the case of fracture risk, the bone fracture mainly took place in the neck region for all types of femoral model. In addition, a combination of the head and neck fracture was also observed in all the models. A combination of neck and intertrochanteric fracture was also found in the normal and AVN groups.

The strength and fracture site of the bone were largely dependent on the load direction and boundary condition. Therefore, in Chapter 3, the three femoral groups were conducted in accordance with fall loading (sideways falling). The computational results exhibited that the fracture load tended to increase with increase of the vBMD estimated in the femoral head and neck region in all the three types of models, although OA and AVN models showed much wider scatter in the data than the normal type. For the fracture load, the average means of 95% confidence intervals of the normal, OA and AVN groups were 1,027±169 N, 1,207±162 N, 1,166±194 N, respectively. Under fall loading, the bone fracture mainly took place in the greater trochanter region for all types of femoral model. In addition, a combination of the greater trochanter and multifarious neck fracture was also observed in all the models. A combination of greater trochanter and intertrochanteric

fracture was also observed in the AVN group. It is, therefore, noteworthy that the fracture strength of the normal, OA and AVN models in sideways fall loading reduced to ≈ 34%, 34% and 31%, respectively, compared to the strength values resulted from stance configuration. Again, the main fracture site in sideways fall was estimated in the greater trochanter region whilst it was in the neck region in the standing.

Along with compressive linear loading analysis, it is also considered to perform the cyclic/fatigue loading to the models for a better clinical usage. Therefore, in Chapter 4, the standard models of elderly patients from each femoral group were analyzed by means of cyclic loading. The result showed that the normal and AVN models could bear the applied load until three cycles of a given loading range, and the average fracture load were 1,734±317 N and 1,536±279 N, respectively. As a matter of fact, the fracture loads were decreased to ≈ 26% for these models, and it was suggested that the femoral strength in cyclic analysis was ≈ 0.74 times of the previous linear analysis. However, in the OA models, the fracture was occurred at two cycles of applied loading range, and the average fracture load was 1,564±114 N. The average fracture load was largely decreased to ≈ 38% and it was supposed that its cyclic strength was ≈ 0.62 times of previous linear one. Regarding the fracture risk, the potential fracture sites in cyclic analysis agreed well with the previous linear analysis. Furthermore, fatigue failure elements resulted from repeated stresses might be one of the indicators for considering bone fracture sites specifically. Overall, the cyclic/fatigue process can result in more realistic FEM femoral models for real-life applications such as walking in daily activity. It is, therefore, believed that these data may be very functional for patient-specific clinical applications.

TABLE OF CONTENTS

ACKNOWLEDGEMENTS **2**

ABSTRACT **4**

TABLE OF CONTENTS **7**

LIST OF TABLES **10**

LIST OF FIGURES **11**

LIST OF SYMBOLS **15**

LIST OF ABBREVIATIONS **16**

CHAPTER 1: INTRODUCTION **17**

1.1 Femoral Fracture and Femoral Diseases **17**

1.1.1 Proximal Femoral Fracture Risk 19

1.1.2 Osteoarthritis 20

1.1.3 Avascular Necrosis 22

1.2 CT Image Based Finite Element Method **25**

1.2.1 CT-based Modelling 26

1.2.2 Boundary Conditions 28

1.2.3 Nonlinear Analysis 30

1.2.4 Evaluation of Material Property from CT Value 30

1.2.5 Fracture Analysis 32

1.2.6 Bone Strength Evaluation through Volumetric QCT 33

1.3 Problem statements **36**

1.4 Goal of study **37**

CHAPTER 2: BONE FRACTURE ANALYSIS UNDER STANCE CONFIGURATION **38**

2.1 Overview **38**

2.2 Analytical Methods 38
2.2.1 Finite Element Modelling 39
2.2.2 Mechanical Modelling and Material Properties 42
2.2.3 Element Failure Criteria 45
2.2.4 Boundary and Loading Conditions 45
2.3 Results and Discussion 47
2.3.1 Correlation Between Fracture Load and vBMD 47
2.3.2 Bone Fracture Behaviour 50
2.3.3 Comparison of Fracture Mechanism of Three models with same vBMD 53
2.4 Conclusion 56

CHAPTER 3: BONE FRACTURE ANALYSIS UNDER SIDEWAYS FALL 58
3.1 Overview 58
3.2 Analytical Methods 58
3.2.1 Finite Element Modelling 59
3.2.2 Mechanical Modelling and Material Properties 62
3.2.3 Element Failure Criteria 64
3.2.4 Boundary and Loading Conditions 64
3.3 Results and Discussion 66
3.3.1 Correlation Between Fracture Load and vBMD 66
3.3.2 Fracture Characteristics 70
3.3.3 Comparison of Fracture Mechanism of Three models with same vBMD 72
3.4 Conclusion 78

CHAPTER 4: BONE FRACTURE ANALYSIS UNDER CYCLIC LOADING 79
4.1 Overview 79
4.2 Analytical Methods 80
4.2.1 Modelling and Material Properties 80
4.2.2 Description of Loading Profiles 86
4.2.3 Determination of Cyclic Strengths 87
4.3 Results and Discussion 89
4.3.1 Cyclic Strength of different femoral models 89

4.3.2 Comparison of Fracture Mechanism under the Linear and Cyclic Loading 96
4.3.3 Failure Element Accumulation under the Linear and Cyclic Loading 101
4.4 Conclusion 104

CHAPTER 5: GENERAL CONCLUSION 105

SUPPLEMENTARY MATERIALS 108

REFERENCES 109

LIST OF TABLES

		Page
Table 2.1	Conversion of element’s density into Young's modulus and yield strength	43
Table 2.2	Mean fracture loads of individual femur group (unit: N) under stance configuration	50
Table 2.3	Classification of fracture regions under stance configuration	53
Table 3.1	Mean fracture loads of individual femoral group (unit: N) under sideways fall	69
Table 3.2	Classification of fracture regions under sideways fall	72

LIST OF FIGURES

		Page
Figure 1.1	Proximal femur location and anatomy	18
Figure 1.2	Description of osteoarthritis hip joint	22
Figure 1.3	Description of hip avascular necrosis	24
Figure 1.4	General usage of Mechanical Finder	25
Figure 1.5	Bone geometry and corresponding CT Iso-surface extracted by MF	26
Figure 1.6	Surface mesh and tetrahedral elements of a FE model with implants	27
Figure 1.7	Shell and truss elements generated by MF	28
Figure 1.8	Boundary condition in 3D FE model of a vertebral body (a), a femur (b) and a skull, showing muscle force with its direction (c).	29
Figure 1.9	Internal calculation process of material property of inhomogeneous materials	31
Figure 1.10	Determination of bone density in tetrahedral element from the CT value	32
Figure 1.11	Stress-strain curve at the fracture	33
Figure 2.1	Three different types of femoral models	39

Figure 2.2	Femoral finite element model. The triangular shell elements were used to model the outer cortex (a), and the trabecular bone and the inner portion of cortical bone were designed using linear tetrahedral elements (b).	41
Figure 2.3	Distribution of Young's modulus in the cross-sectional area	43
Figure 2.4	Boundary conditions: (a) fixed condition, (b) loading condition, and (c) angle specification in polar coordinate system to the bone axis.	46
Figure 2.5	Correlation between fracture load and volumetric bone mineral density, including 95% interval of prediction band (pink color) and confidence band (light red color)	48
Figure 2.6	Three different types of bone fracture behaviour. Fracture patterns were expressed as the distribution of failure elements	51
Figure 2.7	Failure elements against load steps in the three femoral models with the same vBMD	54
Figure 2.8	SED distribution patterns of three femoral models with the same vBMD	55
Figure 3.1	Three different types of femoral models	59
Figure 3.2	FE Femoral model. The triangular shell elements were used to model the outer cortex. (a), and the trabecular bone and the inner portion of cortical bone were designed using linear tetrahedral elements (b)	61
Figure 3.3	Distribution of Young's modulus in the cross-sectional area	63
Figure 3.4	Boundary conditions under fall configuration	65
Figure 3.5	Correlation between fracture load and volumetric bone mineral density, including 95% interval of prediction band (pink color) and confidence band (light red color)	68

Figure 3.6	Three different types of bone fracture behaviour. Fracture patterns were expressed as the distribution of failure elements	71
Figure 3.7	Comparison between the volumes of femoral head and neck region of three femoral models	73
Figure 3.8	Failure elements against load steps in the three femoral models with the same vBMD	74
Figure 3.9	SED distribution patterns of three femoral models with the same vBMD	74
Figure 3.10	Distribution patterns of compressive stress (minimum principal stress), maximum shear stress and failure elements of three femoral models	76
Figure 4.1	3D FE models of the standard normal femora	81
Figure 4.2	3D FE models of the standard OA femora	82
Figure 4.3	3D FE models of the standard AVN femora	83
Figure 4.4	Young's modulus distribution in the mid-section of standard normal femurs	84
Figure 4.5	Young's modulus distribution in the mid-section of standard OA femurs	85
Figure 4.6	Young's modulus distribution in the mid-section of standard OA femurs	85
Figure 4.7	Description of different loading profiles	86
Figure 4.8	Investigation of maximum applied load for cyclic analysis	88
Figure 4.9	Cancellation of cyclic strength determination in which the final fracture occurred during 1st cycle	88

Figure 4.10	Investigation for the cyclic strengths of standard normal femora.	91
Figure 4.11	Investigation for the cyclic strengths of standard OA femora	93
Figure 4.12	Investigation for the cyclic strengths of standard AVN femora	95
Figure 4.13	SED distributions in the mid-section of the normal-1 model	98
Figure 4.14	SED distributions in the mid-section of the OA-1 model	98
Figure 4.15	SED distributions in the mid-section of the AVN-1 model	99
Figure 4.16	Compressive stress ratios of the normal-1 model	100
Figure 4.17	Compressive stress ratios of the OA-1 model	100
Figure 4.18	Compressive stress ratios of the AVN-1 model	101
Figure 4.19	Accumulation of failure elements in the normal-1 model	102
Figure 4.20	Accumulation of failure elements in the OA-1 model	103
Figure 4.21	Accumulation of failure elements in the AVN-1 model	103

LIST OF SYMBOLS

%	Percentage
≈	Approximately
>	Greater than
<	Less than
mm	Millimetre
cm	Centimetre
m	Metre
g	Gram
mg	Milligram
mg/mm^3	Milligram Per Cubic Millimetre
g/cm^3	Gram Per Cubic Centimetre
MPa	Megapascal
GPa	Giggapascal
N	Newton
E	Young's Modulus
°	Degree

LIST OF ABBREVIATIONS

aBMD	Areal Bone Mineral Density
AVN	Avascular Necrosis
BMD	Bone Mineral Density
CT	Computed Tomography
DXA or DEXA	Dual-energy X-ray Absorptiometry
FEA	Finite Element Analysis
FEM	Finite Element Method
GT	Greater Trochanter
HU	Hounsfield units
OA	Osteoarthritis
SD	Standard Deviation
SED	Strain Energy Density
UTS	Ultimate Tensile Stress
vBMD	Volumetric Bone Mineral Density
YS	Yield Stress

CHAPTER 1

INTRODUCTION

1.1 Femoral Fracture and Femoral Diseases

The femur is the longest, largest, and strongest bone in the human body [1]. It spans from the hip joint, where it articulates with the pelvis, to the knee joint, where it articulates with the tibia and patella. The femur broadly consists of proximal and distal extremities joined by an almost cylindrical shaft. For the femoral strength evaluation and hip fracture research purposes, this study mainly emphasizes on the proximal femur, encompassing the proximal (superior) extremity and the top portion of the shaft. The anatomy of the femur is shown in Figure 1.1 [2]. The most proximal portion of the femur is the femoral head, a spheroidal section of bone covered with cartilage that slides against the acetabulum in the pelvis. The femoral neck can be considered as a longitudinally concave cylinder that connects the femoral head to the shaft [3]. The greater trochanter (GT) is a large protuberance that forms the most lateral and palpable portion of the femur. It serves as the point of attachment for several muscles that connect the femur to the pelvic bone. The lesser trochanter is a smaller feature protruding from the posteromedial shaft, just inferior to the GT. It provides attachment to large muscles connected to the iliac crest of the pelvic bone and to the transverse processes of the lumbar vertebrae. The two trochanters are connected anteriorly by the intertrochanteric line and posteriorly by the intertrochanteric crest. The circle created by the two trochanters and two intertrochanteric ridges provide attachment for a number of ligaments that connect to several locations in the pelvic bone, including those that form the hip joint capsule [4].

Internally, the proximal femur is composed mainly of trabecular bone surrounded by a thin layer of cortical bone. The cortical bone thickens inferiorly on the proximal end of the shaft, while trabecular bone becomes sparser in the same region. Gradually, the internal structure of the shaft turns into a thick cylinder of cortical bone mainly filled with marrow in the medullary cavity. The trabeculae at the head are arranged in such a way that they form a dense central wedge supported mainly against the upper and lower profiles of the neck [2]. The typical vertical loads applied when bearing the body weight are thus passed from the femoral head through the central wedge and toward the junction of the neck and shaft.

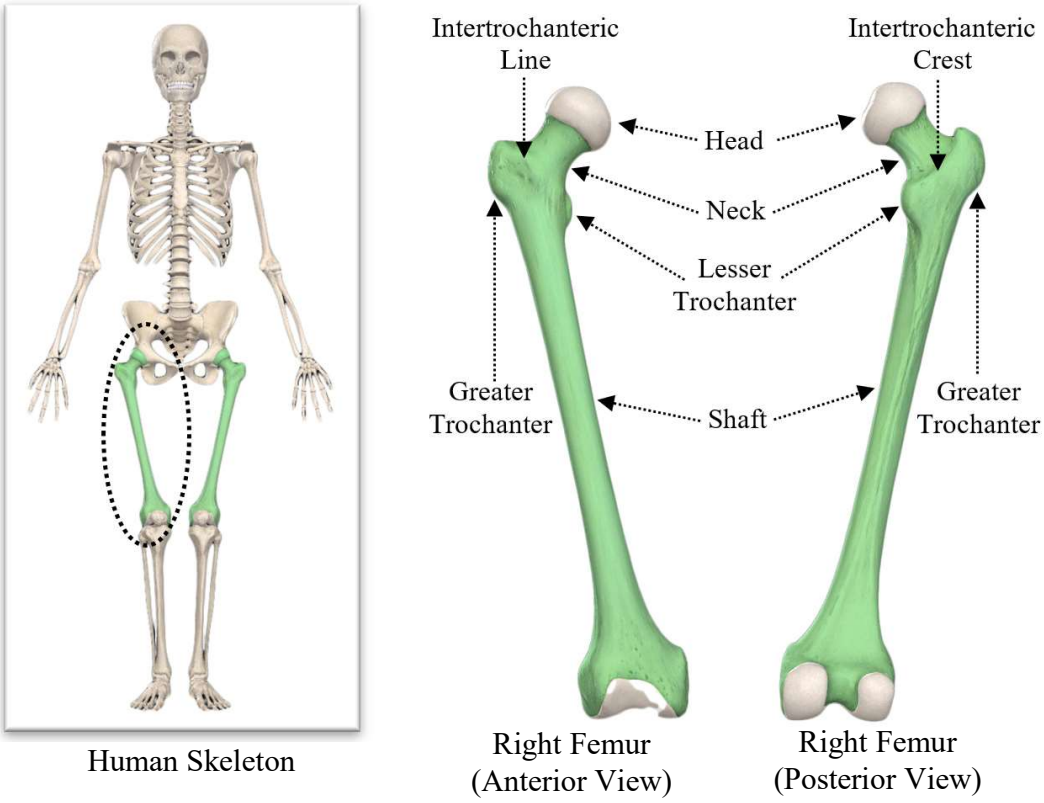

Figure 1.1: Proximal femur location and anatomy.

1.1.1 Proximal Femoral Fracture Risk

The proximal femoral fractures have been accounted for a large proportion of hospitalization among trauma cases [5]. Over 90% of these patients are aged above 50 years [6]. The incidence of femoral fracture is 2 to 3 times higher in females than male population [6]. Based on the anatomical locations, these fractures can generally be classified into: femoral neck fracture, intertrochanteric fracture and subtrochanteric fracture. Each of these fracture types requires special methods of treatment and have its own set of complications and controversies regarding optimal management. Along with the trauma cases, the common bone diseases such as osteoporosis (elderly patients whose bones have become weakened due to progressive loss of BMD), osteoarthritis (degenerative joint disease) and osteonecrosis (the death of bone tissue due to a lack of blood supply) will have a huge impact on the bone fracture mechanism. It is well known that the bone fracture is associated with its strength, and it is also greatly predominant by many factors; i.e., age, sex, BMD, bone geometry, impact direction and so on. Therefore, patient-specific fracture risk analysis may be very useful for prior clinical interventions.

To address the biomechanical issues, many studies have proven effective in determining relationships between proximal femur strength and all the aforementioned factors affecting the structural capacity of the proximal femur [7–15]. Therefore, it is a good option for applying biomechanical computed tomography (BCT) test to evaluate the femoral strength and fracture sites. The BCT test comprises a finite element analysis of bone strength using a clinical CT scan as an input [16]; and it also includes CT-based measurements of BMD. Utilizing the patient's CT scan, the BCT can perform a virtual stress test to compute a measurement of bone strength, which is the force required to

virtually break or fracture the patient's hip or spine in a standardized loading configuration. With nonlinear FEA, these virtual stress test models can provide spatial distributions of failed bone material and bone damage within the whole bone [16–18], which can provide insight into the type of fracture under the prescribed loading conditions. Hence, this technique with tremendous benefits encourages the researchers to conduct functional noninvasive studies of live patients (i.e., *in vivo* FE models*)* for preventive and diagnostic care concerning femoral fracture.

1.1.2 Osteoarthritis

Osteoarthritis (OA), also called degenerative arthritis or wear-and-tear arthritis, is the most common form of arthritis among over 100 different forms [19,20]. It is associated with a breakdown of cartilage in joints. To describe the OA, physicians often use various terms such as joint deterioration, joint degeneration, joint narrowing, bone-on-bone, calcium deposits, bone spurs, joint diminishment or even "just" arthritis. OA is a highly prevalent musculoskeletal disorder, that affected 303 million people globally in 2017 [21]. It can affect any joint, but preferentially affects the knee, hands, hip and spine. Progressive loss of articular cartilage is often accompanied by a reparative process that involves sclerosis and osteophyte formation as shown in Figure 1.2. OA has a considerable impact on the individual patient, resulting in pain and disability, and on society. According to a submission by Osteoarthritis Research Society International (OARSI) of a White Paper, OA has a large economic burden on patients and society, describing as a serious disease [21,22].

Hip OA and proximal femoral fractures mainly affect elderly patients. However, several authors have claimed that the prevalence of proximal fracture is clinically rare in hip OA patients, and they even have a better quality of bone [23–26]. They are less likely to be suffering from osteoporosis and less vulnerable to fractures of the proximal end of the femur [24]. On the other hand, OA was found to affect the fracture site, showing a higher prevalence in extracapsular than intracapsular regions [27,28]. This correlation becomes more significant with increasing the OA severity. Again, Robstad et al. also announced that patients with trochanteric fractures had a higher tendency of OA occurrence than those with femoral neck fractures. by comparing 349 patients with proximal femoral fractures and 112 patients with hip contusion [29]. It can therefore be considered that the hip osteoarthritis could represent a protective factor for intracapsular fractures and a risk factor for trochanteric ones. Recently, Sugano et al. conducted a comparison study for bone strength of the proximal femur with and without hip OA using CT-based FEA. Their results indicated that the proximal femoral strength was affected by the severity of the osteoarthritis, and the femoral strength of patients with hip OA were significantly higher than that of patients without hip OA [25]. However, the potential fracture location of the hip OA patients was not available in details. In order to assess the femoral fracture risk, the investigation of strength and fracture sites could be clinically very useful. Therefore, in this study, 58 FE femoral models were analyzed under different boundary and loading conditions to investigate the optimum femoral strength and fracture location of the elderly OA patients.

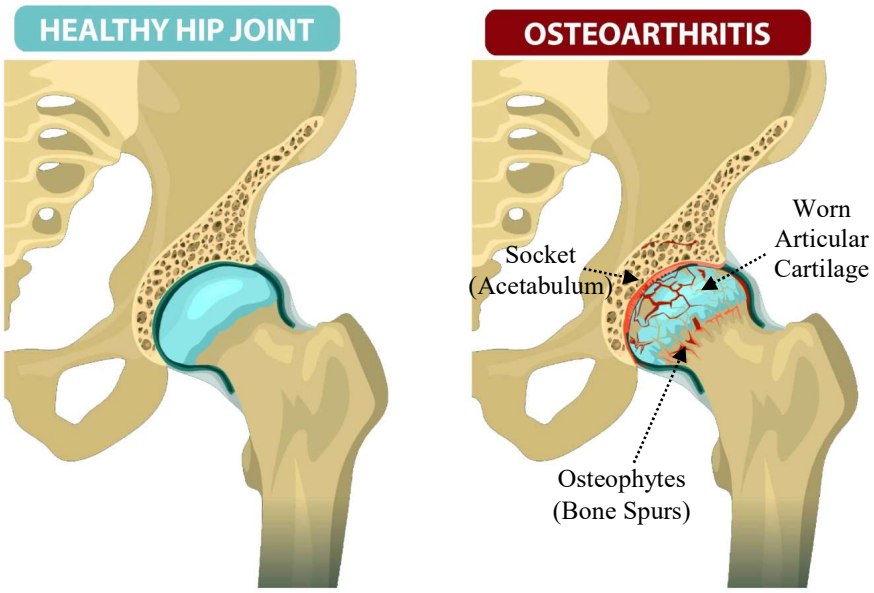

Figure 1.2: Description of osteoarthritis hip joint

1.1.3 Avascular Necrosis

Avascular necrosis (AVN), on the other hand, is also a common bone disease caused by the death of bone tissue due to a lack of blood supply to the affected area. AVN is also called aseptic necrosis, ischemic bone necrosis, or osteonecrosis. AVN affects most commonly the epiphyses (ends) of the femur. The affected femoral head is diagrammed in Figure 1.3. The upper arm, the shoulder, the knee, and the ankle are also other commonly affected areas by AVN. It tends to occur in men more often than women and typically is diagnosed between ages 30 and 50 [30,31]. Based on the X-rays and MRI findings on the AVN femoral head, it can be classified into various stages (stage I to IV) [32]. The higher the stage level is, the larger the extent of collapsed surface of the femoral head. The aetiology of osteonecrosis is complex about numerous contributing

agents: most markedly in trauma, high steroid dosage, excessive alcohol intake, etc [31,33].

Every year, 10,000-20,000 new patients are affected with osteonecrosis of the femoral head (ONFH) in the United States (US) [34]. In Japan and Korea, the annual prevalence is more than 10,000 [35,36]. Other studies pointed out that there have been about 50% of the total hip arthroplasties performed in Asia and sub-Saharan Africa [37–39] and more than 10% of those in the US [40]. Concerning the treatment, ONFH progression can be debilitated, and in severe cases, can necessitate total hip arthroplasty (THA). Furthermore, as the patients with nontraumatic ONFH tend to be young and active, their total hip arthroplasties generally have a higher rate of revision [41,42] and worse outcomes [43] than those performed for primary hip OA. Therefore, clinical researchers have attempted to develop effective treatments for joint preservation in ONFH patients. On the other hand, the increasing incidence and AVN debilitating progression also suggest a need for additional investigation of effective and novel treatments.

With the advancement of FEM technology, the *in vivo* CT scans models of live patients have been broadly applied in the current medical world, expecting for early diagnosis and interventions as well as the evaluation of biomechanics in AVN femoral head. Through an FEA study, Bahk et al. have recently reported that a stress concentration around AVN collapsed hips focused on the lateral pillar and primary compression trabecula, indicating a high probability of future collapse in ONFH [44]. Moreover, Huang et al. claimed that a silk protein rod implantation has less displacement and surface stress at the ONFH of weight-bearing area compared with simple core

decompression and suggested a silk protein as a suitable biomaterial in AVN surgery [45]. Along with these studies, it is considered that knowing femoral strength and fracture location may be clinically very helpful for a patient with AVN disease. For this purpose, in this study, 30 AVN FE femoral models were analyzed under different boundary and loading conditions to investigate the optimum femoral strength and fracture location of stage I to IV AVN patients.

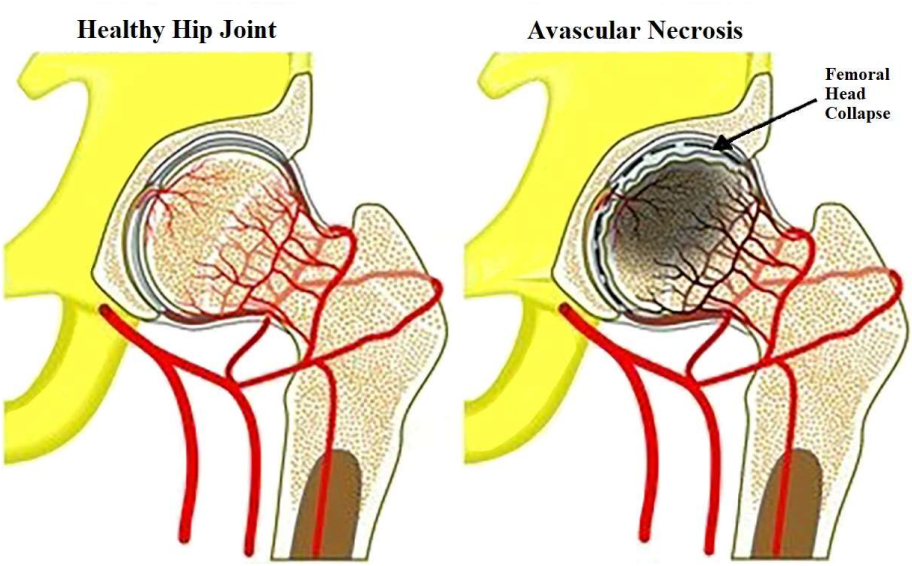

Figure 1.3: Description of hip avascular necrosis

1.2 CT Image Based Finite Element Method

Mechanical Finder (MF) is a powerful software that can construct and simulate various computational finite element (FE) models, especially in the fields of orthopaedics, dentistry, engineering and so on. It can evaluate bone strength by considering the entire bone as a 3D structure and applying FEA. MF includes all the functions required for CT based FEA, and thus, it can be used to perform the desired procedures such as DICOM import, segmentation, implant installation, mesh generation, material setting, boundary condition setting, analysis and result evaluation. The MF is currently using not only in the medical and dental fields but also in the engineering, and its usages are generally segmented in Figure 1.4. [46].

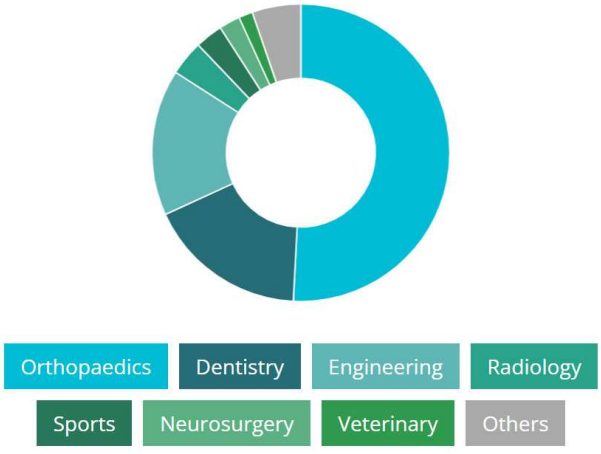

Figure 1.4: General usage of Mechanical Finder.

1.2.1 CT-based Modelling

Since 3D model can be constructed from DICOM data, it is possible to reflect the patient-specific bone geometry to the model. MF can create 3D model by extracting region of interest (ROI) such as bone from CT data by image processing or manual correction. Because it is a computerized model, the osteotomy models and bone defect models can be easily created. The reconstructed bone geometry from a CT image and related iso-surface are displayed in Figure 1.5 [47]. The CT scan represents tissue density values such as bone, soft tissue, air, etc. Therefore, it is possible to visualize a surface corresponding to the selected tissue type by choosing its density value.

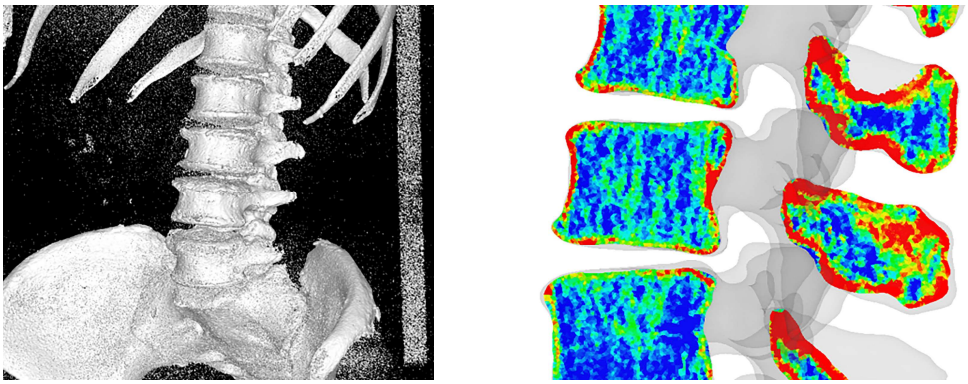

(a) Bone geometry (b) CT Iso-surface

Figure 1.5: Bone geometry and corresponding CT Iso-surface extracted by MF.

With size-controllable mesh generator, a tetrahedral mesh can be automatically generated on the constructed models after specifying the desired size. Moreover, in the

complex models, the mesh can also be accurately generated between the boundaries of bone material and multiple implants. Surface mesh and tetrahedral elements of a FE model with implants were shown in Figure 1.6. In addition to tetrahedral elements, both the shell and truss elements can also be set in MF. The shell elements can be used for modelling of 3D structures when the thickness of the element is neglected. Whereas, the truss elements are used for modelling ligaments where force works only in the tensile direction. The shell and truss elements generated by MF are shown in Figure 1.7 [47].

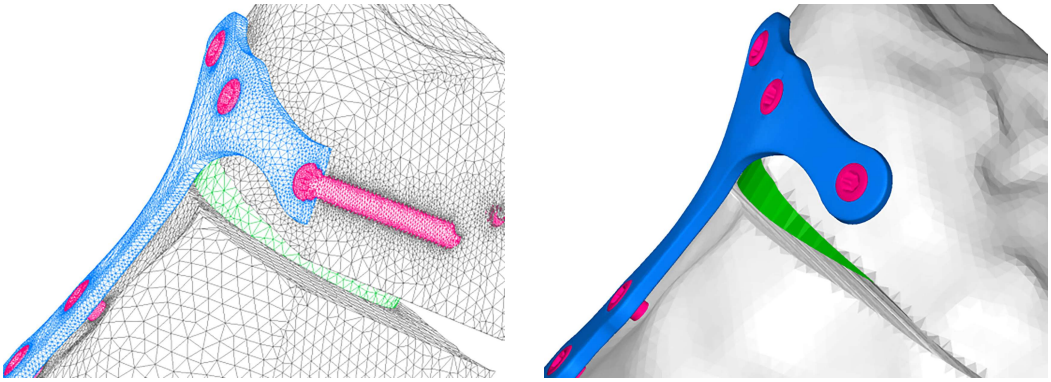

(a) Surface mesh (b) Tetrahedral elements

Figure 1.6: Surface mesh and tetrahedral elements of a FE model with implants

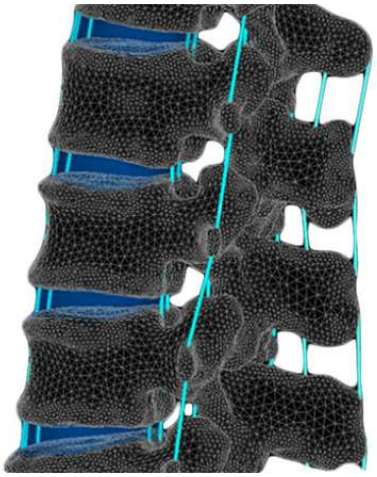

Figure 1.7: Shell and truss elements generated by MF.

Regarding material property, bone FEA has been performed with homogeneous material, or a two-layered model consisting of cortical bone and cancellous bone. However, inhomogeneity of the material is important to evaluate bone stress and fracture because each element in the model has different critical stress in practice. As the density of an element is converted from CT value, each material property such as Young's modulus (E) and yield strength (YS) values can be calculated from density value by referring to previous researches. In this study, those values were estimated from the corresponding density using the empirical formulae implemented by Keyak et al. [48].

1.2.2 Boundary Conditions

The boundary conditions, i.e., the constraints and loading directions, can be set based on the preset axis. The standard preset axis setting is relatively convenient to align

conditions between analyses with different CT data. Standard femoral and vertebral methods in MF would be a good option for comparison study in numerous models. In addition, the various fixed positions and load directions can also be set manually as needed, depending on the analysed models as depicted in Figure 1.8 (a) and (b) [49,50]. On top of these, when it is needed to set the muscle force by load in the model, its direction can also be set to always point from the origin to the insertion even if the bone positional relationship changes, as shown in Figure 1.8 (c) [47]. In this study, the FE femoral models of 73 patients were set by standard femoral method and analysed their fracture load and fracture sites.

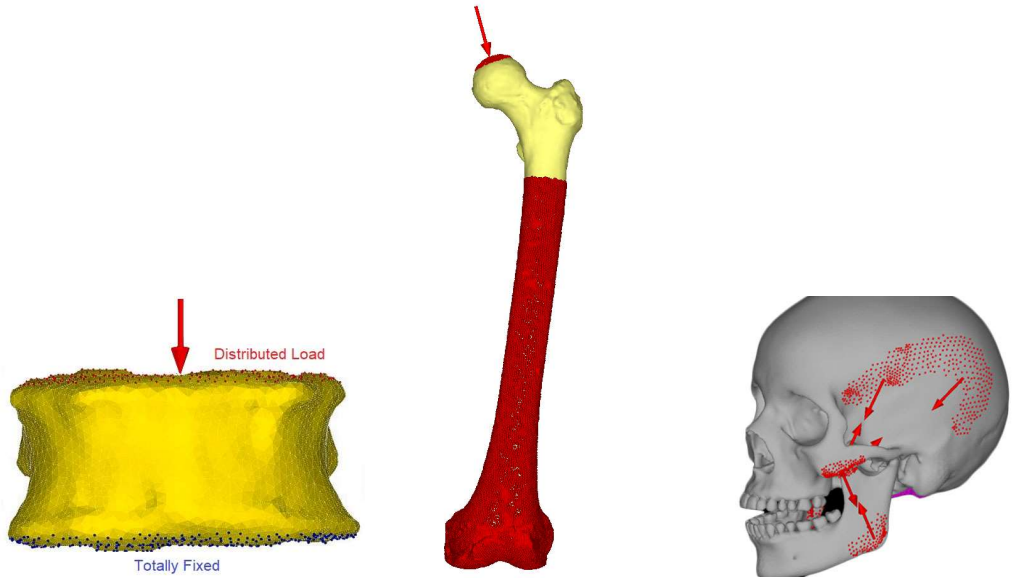

(a) (b) (c)

Figure 1.8: Boundary condition in 3D FE model of a vertebral body (a), a femur (b) and a skull, showing muscle force with its direction (c).

1.2.3 Nonlinear Analysis

In addition to elastic analysis, the material nonlinear analysis can also be performed by MF dealing with the plasticity and fracture of elements. To evaluate clinical fractures, it is necessary to define a fracture criterion in FEA, which is often found as bone strength from the load-displacement curve. The cadaveric experimental validations have been conducted by some researchers [51,52]. Along with material nonlinearity, not only analysis based on small deformation theory but also geometric nonlinear analysis is available. Especially in analysis with large deformation and rotation, analysis can be performed accurately by geometrical nonlinear analysis. Moreover, soft tissue such as intervertebral disc can be modelled as super-elastic element. With these superiorities, the FE femoral models were simulated by means of material nonlinearity and nonlinear geometry in this study aiming for reliable clinical models.

1.2.4 Evaluation of Material Property from CT Value

The inhomogeneous material properties of tetrahedral elements constructed from the CT images were evaluated by the process described in Figure 1.9, and the calculation process was as follows:

(1) One of the solid elements of the mesh was extracted.

(2) The bone density of the element was determined from the average number of Hounsfield units (HU) obtained for a total of 17 points in the element, shown in Figure 1.10. The CT data within the element has to be averaged because CT images have a lot of impulse noise (salt-and-pepper).

(3) The density was then calculated from obtained CT value with standard conversion equation.

(4) Using the calculated density, the material property of the element was evaluated by Keyak conversion equation.

(5) Repeat from (1) for all elements of the mesh.

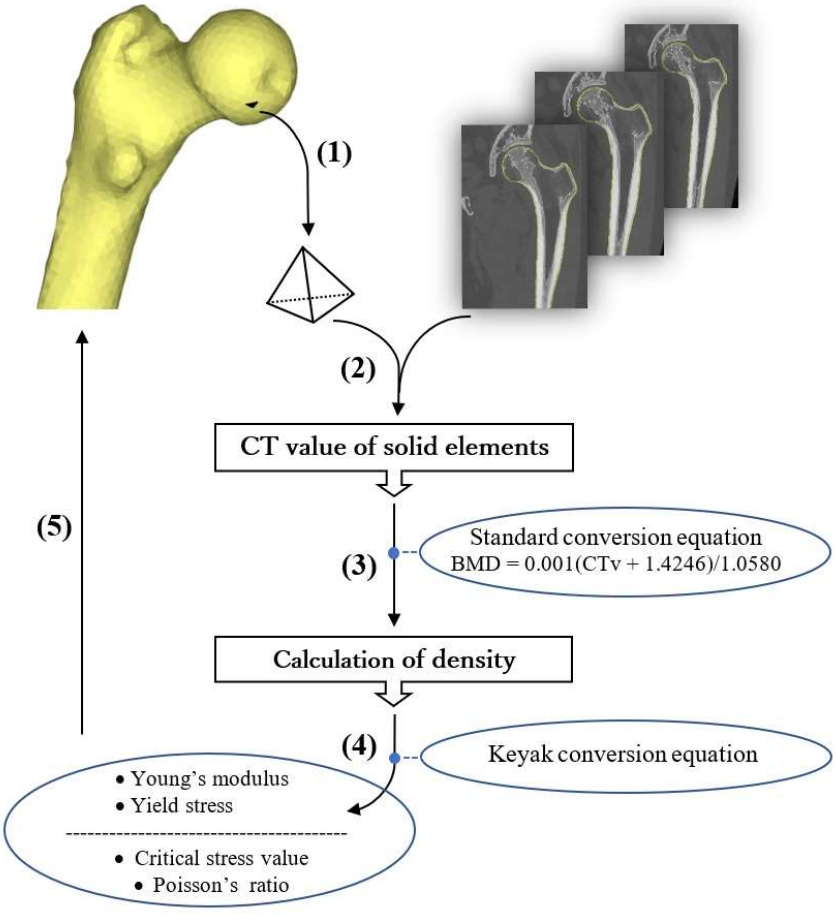

Figure 1.9: Internal calculation process of material property of inhomogeneous materials.

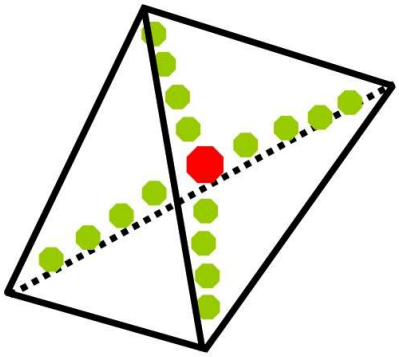

Figure 1.10: Determination of bone density in tetrahedral element from the CT value.

1.2.5 Fracture Analysis

In this study, the element failures in the femoral models constructed by MF were determined in terms of tensile and compressive failure criteria as shown in Figure 1.11. In the compressive direction, when equivalent stress of the element exceeds its yield stress, the element becomes plastic (Point A). And, when the minimum principal strain of plastic element exceeds crush strain (the specified strain is -10,000 μ strain in this study) [53,54], it becomes compression failure, i.e. element crushing (Point B). In tensile failure, when the maximum principal stress exceeds the critical stress, a crack occurs (Point C). The crack becomes perpendicular to the principal stress direction.

In Figure 1.11, both stress-relaxation coefficient and crush strain are parameters related to fracture behaviour on compression zone. Regarding elements changes from elastic into plastic behaviour during compression, the gradient of stress-strain curve after yielding is changed by the stress relaxation factor to get close to an actual behaviour.

Crush strain is then used for the judgment of crush of plastic element so that it becomes the crushed element if it exceeds the value of crush strain.

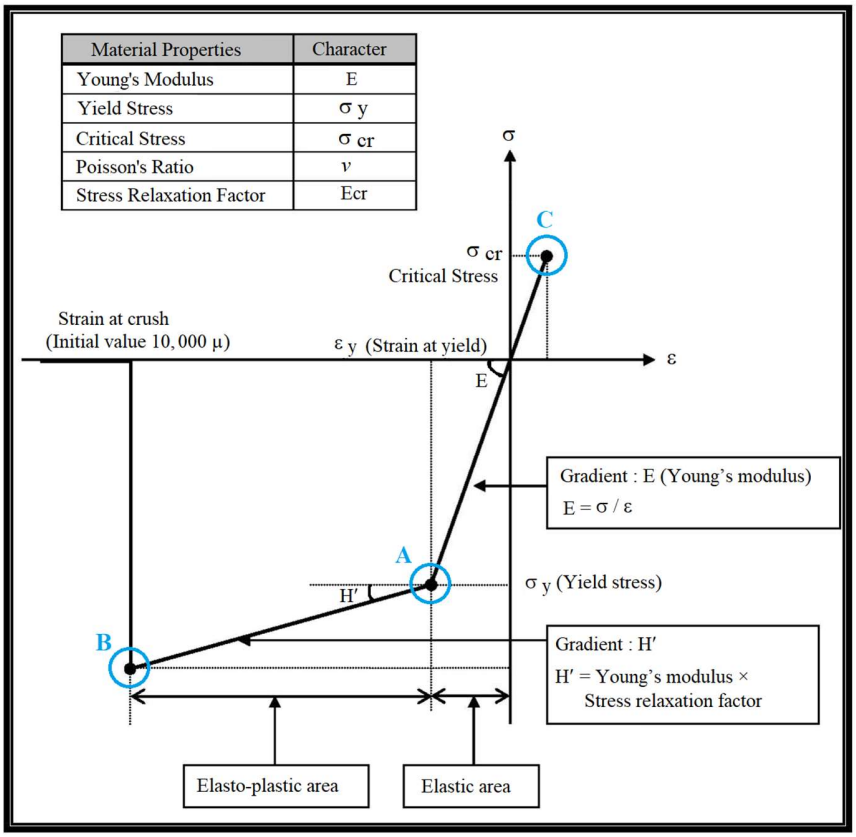

Figure 1.11: Stress-strain curve at the fracture.

1.2.6 Bone Strength Evaluation through Volumetric QCT

From a biomechanical point of view, fracture risk of a part of the bone is thought to be strongly correlated with its strength. It is however obvious that the direct in-vivo measurement of the failure load of bone so-called the bone strength (BS) is impracticable. Therefore, BS values of specific bones such as femurs and vertebrae have been evaluated effectively and biomechanically by using computed tomography images based finite

element analysis (CT-FEA) [55]. To evaluate the BS, the most direct approach could be a mechanical test on cadaver bones associated with the bone fracture analysis. The BS means the applied load at the final stage that element failure starts to appear under a given boundary and loading condition. While it is not feasible to conduct by direct methods, the CT-FEA is a technologically advanced method currently available for the noninvasive clinical assessment of BS [56]. The workflow of CT-FEA usually contains region of interest (ROI) extraction on QCT scan, 3D reconstruction and meshing, material property assignment, loading and boundary conditions setting, and, last, BS evaluation or mechanical properties analysis. This technique has been sufficiently verified by a number of mechanical experiments in cadaver studies [51,53,57–60]. Among these studies, a comprehensive description of fracture analysis performed on the fresh frozen femoral cadaver models and those of CT-FEA models are compared in Figure 1.2 [51].

In order to apply FEA methodology into the biomechanical simulation of bones, the homogenization theory and 3D constitutive models have been widely used to deal with the multiscale structure and the nonlinear behaviors [61–63]. In CT-FEA, cortical and trabecular bone can be constructed by stacking the elements with adjustable sizes and properties depending on local structure and materials. The usage of CT images has been established to provide the spatial distribution of bone mechanical properties such as the elastic modulus and the yield strength for the elements, especially after proposing the empirical formula by Keyak et al. [64] and Keller [65]. There was also a substantial progress has also been made with *in-vitro* bone strength experiment in accord with the femoral and vertebral FE models. For instance, the proximal femoral FE model has been

recorded with high correlation coefficients from 0.85 to 0.9 ($p < 0.05$) between the experimentally tested fracture load and the FEA-simulated load [57,59,66]. Likewise, in the case of vertebral BS, the correlation coefficients of the predicted strength and the experimental strength were ranged from 0.78 to 0.86 ($p < 0.05$) [67–70]. Overall, the accuracy and the reliability of CT-FEA has been validated in the field of computational bone biomechanics [49,71].

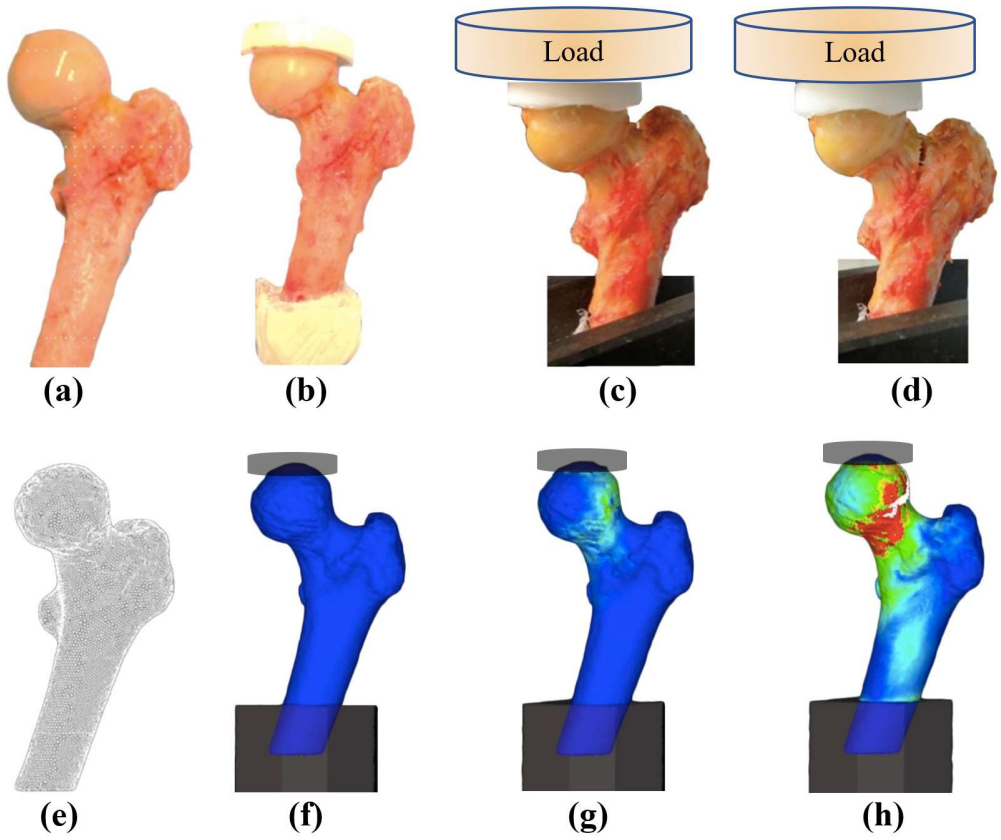

Figure 1.2: Fracture load prediction under mechanical test and FEA simulation for a validation study. The cadaver femoral models (a-d) and CT-FEA models (e-h).

1.3 Problem statements

Nowadays, aging population in Japan are growing at the fastest rate in the world. In 2018, 28.1% of the country's population was age 65 years or older, and 4.5% was 85 years or older [72], indicating a high possibility of femoral fracture risk in the future. With the hip fracture incidence increasing worldwide, for each of the osteoporotic patients, the estimation of fracture location and optimum strength of the femur have actively been performed. For example, the bone densitometry and the diagnostic imaging methods have generally been used to predict the risk of bone fracture. These methods usually provide regional bone density values for specific portions of the proximal femur and can visualize figures and shapes of the specific areas of the bone that may be related to the possibility of hip fracture [73]. However, these methods cannot provide a quantitative strength which is directly related to the fracture risk of the femur because the femoral strength depends on its 3D geometry, heterogeneity, distributed mechanical properties, and loading conditions.

In the meantime, a computer simulation method such as the CT-image based finite element method (CT-FEM) has been utilized to estimate the mechanical strength of femurs in order to assess the hip fracture risk of the elderly patient with osteoporosis [3-9]. Moreover, CT-FEM can analyze and predict not only the distributions of stress and strain within the bone model but also the fracture locations under the different boundary conditions [9,10].

Along with osteoporosis, some typical femoral diseases such as osteoarthritis (OA) and avascular necrosis (AVN) might significantly affect the femoral fracture behaviour

and therefore the femoral strength; however, the effects of such diseases on the mechanical performance of femurs have not been investigated yet. The computational FE analysis was therefore carried out in this study to evaluate the strength and fracture site of 3D FE models of 130 femurs with healthy, OA and AVN conditions. Moreover, there will be a wide range of the femoral head deformity in the OA and AVN femurs due to the femoral infringement in OA femurs and various disease levels in AVN type, indicating a necessity of optimum femoral strength and fracture location. Therefore, the patient-specific computational analysis will be biomechanically useful for clinical applications.

1.4 Goal of study

The objectives of this study were as follows:

(i) To investigate the correlation between the vBMD of femoral head and neck region and FEA-simulated femoral strength of the normal, OA and AVN femora under stance configuration and sideways falling by linear compressive loading,

(ii) To estimate the most vulnerable fracture location (fracture site) of these femora for both stance and sideways fall configurations, and

(iii) To conduct a bone fatigue analysis by means of cyclic loading and compare with the linear compressive loading analysis, expecting for a better clinical usage.

CHAPTER 2

BONE FRACTURE ANALYSIS UNDER STANCE CONFIGURATION

2.1 Overview

The CT data were collected from four different university hospitals located in the southern Kyushu Island, Japan. Through these CT images of lower limbs of 73 patients, 3D computational finite element (FE) models of 130 femurs with healthy (contralateral), OA and AVN conditions were constructed using MF software. Then, for each of the FE models, the mechanical testing was performed under a compressive loading condition in order to estimate its femoral strength and the fracture behaviour. Such fracture behaviour was recreated as the accumulation of element fracture under both the tensile and compressive stress conditions. The computational results exhibited that the fracture load tended to increase with increase of the volumetric bone mineral density (vBMD) estimated in the femoral head and neck region in all the three types of models, although AVN models showed much wider scatter in the data than the other two types. The bone fracture behaviour was expressed as appearing as the distribution pattern of failure elements in the head and neck region. The bone fracture mainly took place in the neck region for all types of femoral model. In addition, a combination of the head and neck fracture was also observed in all the models. A combination of neck and intertrochanteric fracture was also observed in the normal and AVN groups.

2.2 Analytical Methods

2.2.1 Finite Element Modelling

Femoral CT data of 73 patients (10 men aged 37-75 years old, the average age of 51.49 years old; and 63 women aged 19-87 years old, the average age of 65.06 years old) were collected from four different universities hospitals located in the northern Kyushu Island, Japan. From these CT images, a total of 130 computational femoral models were constructed. Based on the patient's clinical data confirmed by orthopaedic surgeons, the 130 femurs were classified into three groups; a normal of 42 femurs (N1 group), OA of 58 femurs (N2 group) and AVN of 30 femurs (N3 group). The three different types of the femur are illustrated in Figure 2.1.

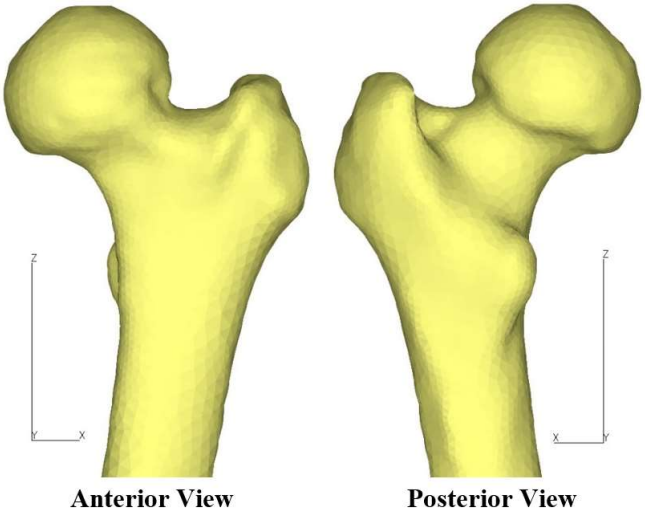

(a) Normal model

Figure 2.1: Three different types of femoral models.

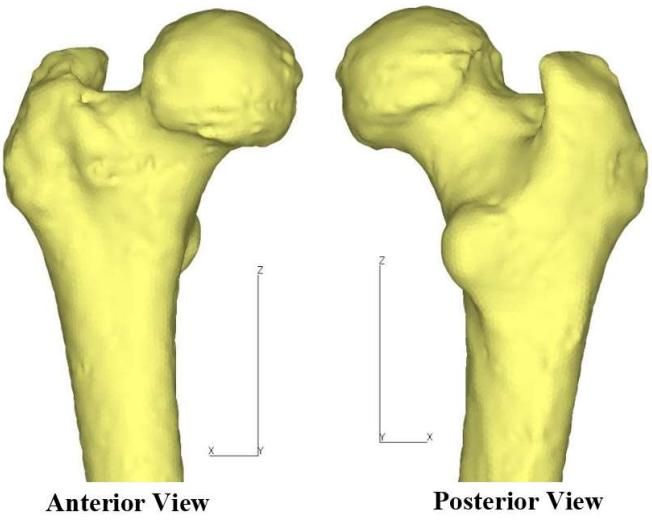

(b) OA model

Figure 2.1 (continued)

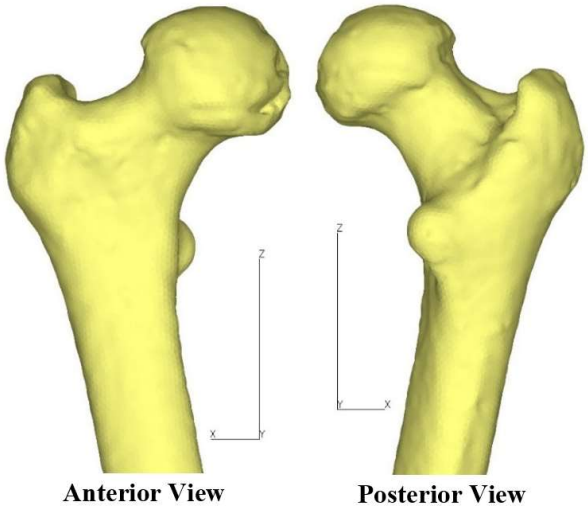

(c) AVN model

Figure 2.1 (continued)

Three-dimensional numerical and finite element models were constructed using Mechanical Finder v.11 (Research Center of Computational Mechanics Inc., Tokyo, Japan). Firstly, the two-dimensional contours of a femur were extracted from the corresponding CT images, and they were smoothly connected each other to construct 3D femoral model. Then, the inside of the femoral model was filled with the tetrahedral elements to create a finite element (FE) model for the computational mechanical analysis as shown in Figure 2.2 [74]. The size of the tetrahedral elements was set to 1 to 2 mm. The whole surface of the FE model was also generated using the shell elements to imitate the stiff outer surface of the cortical bone with the greatest bone mineral density [75]. The number of solid elements included in our models was an average of 745,060 and that of shell elements was of 57,520, depending on the size of the femur.

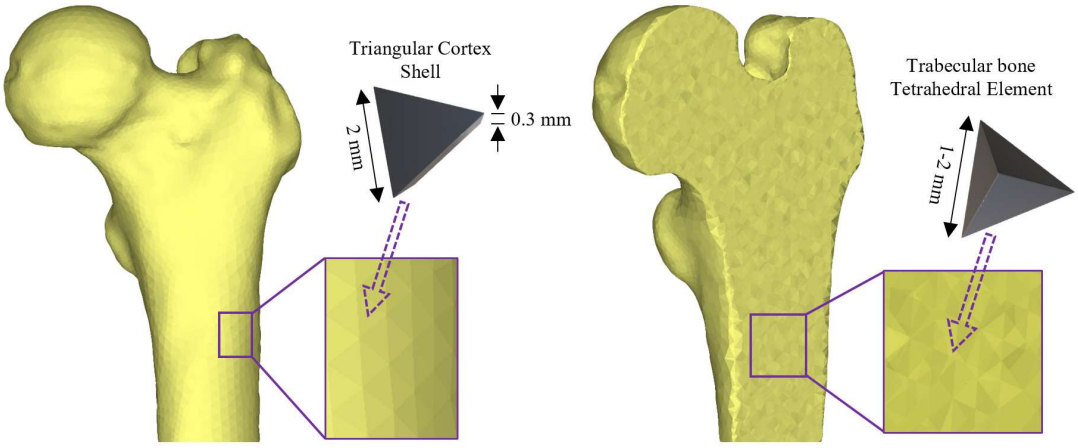

(a) Shell element (b) Trabecular solid element

Figure 2.2: Femoral finite element model. The triangular shell elements were used to model the outer cortex (a), and the trabecular bone and the inner portion of cortical bone were designed using linear tetrahedral elements (b).

2.2.2 Mechanical Modelling and Material Properties

The tensile deformation behaviour of all the femoral bone models was assumed to be linear elastic characterized by two material parameters such as Young's modulus and Poisson's ratio, while their compressive deformation behaviour was assumed to be characterized by an elastic-plastic response with four material parameters such as Young's modulus, Poisson's ratio, yield strength and the work hardening coefficient.

For each of the tetrahedral elements, its mean BMD was firstly calculated from the corresponding CT value (CTv) by using the following linear equation [76–78]:

$$BMD = 0.001(CTv + 1.4246)/1.0580 \quad (1)$$

where the units of BMD and CTv are given by g/cm^3 and Hounsfield Unit, respectively. Then Young's modulus of the element was estimated from the corresponding BMD by using the empirical formulae proposed by Keyak as shown in Table 2.1 [48]. For all the tetrahedral elements, Poisson's ratio was set to 0.4 [57]. On the contrary, for all the shell elements, Young's modulus and Poisson's ratio were fixed to 20.6 GPa and 0.167, respectively. The distribution patterns of Young's modulus in the three femoral models presented in Figure 2.1 are shown in Figure 2.3. Distribution of the higher moduli corresponded to the location of cortical bone, while the lower moduli expressed cancellous bone and marrow.

Table 2.1: Conversion of element's density into Young's modulus and yield strength

Density (g/cm^3)	Young's Modulus (MPa)
$\rho = 0$	$E = 0.001$
$0 < \rho \leq 0.27$	$E = 33900\rho^{2.20}$
$0.27 < \rho < 0.6$	$E = 5307\rho + 469$
$\rho \geq 0.6$	$E = 10200\rho^{2.01}$
Density (g/cm^3)	**Yield Strength (MPa)**
$\rho \leq 0.2$	$\sigma_{yield} = 1.0 \times 10^{20}$
$0.2 < \rho < 0.317$	$\sigma_{yield} = 137\rho^{1.88}$
$\rho \geq 0.317$	$\sigma_{yield} = 114\rho^{1.72}$

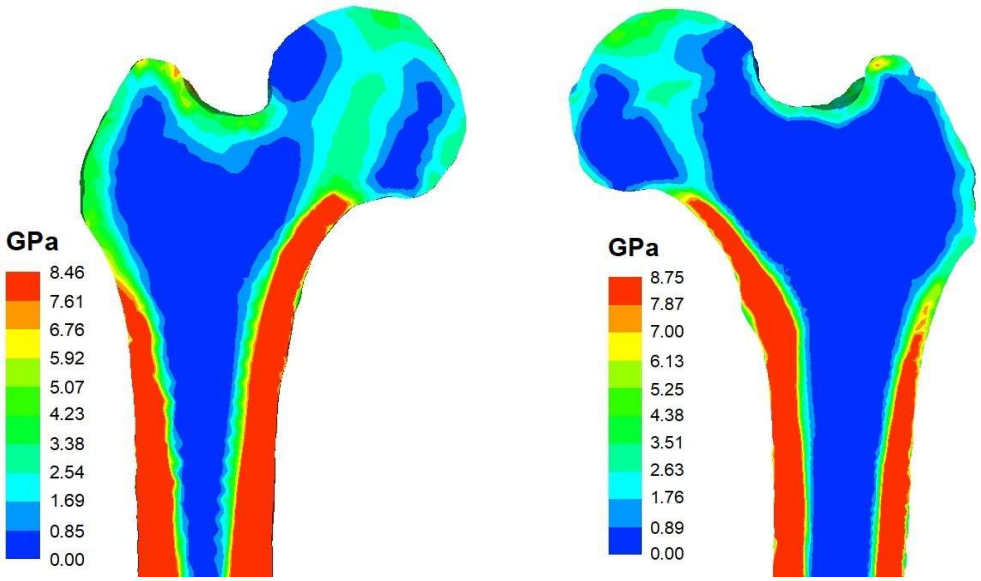

(a) Normal model (b) OA model

Figure 2.3: Distribution of Young's modulus in the cross-sectional area.

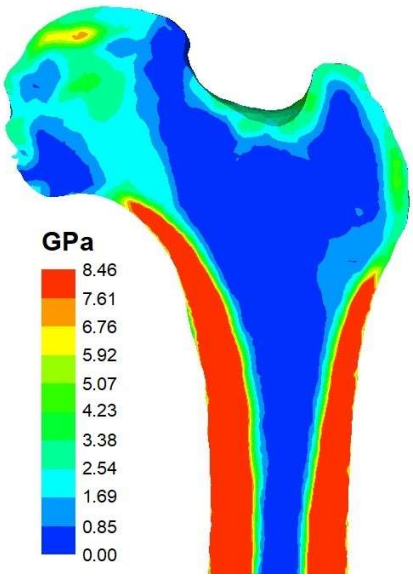

(c) AVN model

Figure 2.3 (continued)

Under the compressive deformation of all the elements, it was assumed that the onset of yielding took place when the Drucker-Prager equivalent stress reached the compressive yield strength (this is called 'Drucker-Prager yield criterion'). The yield strength of each element was also obtained from the element's BMD by using the empirical formulae proposed by Keyak, shown in Table 2.1 too, while the yield strength of all the shell elements was set to 20.6 MPa. The work hardening coefficient was set to 0.07 for all the elements.

2.2.3 Element Failure Criteria

In this FE analysis, bone fracture was reproduced as an aggregation of failure elements. Different failure criterions were used in the tensile and compressive stress conditions. Under the tensile stress condition, the maximum principal stress criterion was utilized to express the onset of tensile bone fracture. It was assumed that the tensile failure of an element took place when the maximum principal stress reached its critical value, which was equal to 0.8 × (compressive yield strength) [79]. On the contrary, under the compressive stress condition, the minimum principal strain criterion was used to express the compressive bone fracture. It was assumed that the compressive failure of an element took place when the minimum principal strain reached its critical value which was equal to -10,000 μ strain, following the yielding of the element [80]. The failure of the element under both tensile and compressive conditions was expressed by reducing the modulus down to the minimum value in the whole femoral model. The strength of the femoral model was then defined as a critical value of the applied load when 15 shell elements were failed [81].

2.2.4 Boundary and Loading Conditions

Firstly, the bone axes were set on the basis of the femoral method and then, the boundary conditions were determined accordingly. The boundary conditions, i.e., the fixed and loading conditions, are shown in Figure 2.4, respectively. As the fixed condition, the femoral surface from the bottom condylar surface to the line on the diaphysis located approximately 15 mm below the lesser trochanter was totally fixed as

shown in Figure 2.4(a). The distributed load was applied to the top surface of the femoral head under stance configuration as shown in Figure 2.4(b). The total value of the applied load was set to 10,000 N. The total load was divided into 10 main steps and each of the main steps was also divided into 4 sub-steps. Concerning the loading direction, α was defined as the degree tilt from the longitudinal axis, while β was the degree turn around the axis as shown in Figure 2.4(c) [48]. In this analysis, α and β were set to 20º and 160 º, respectively.

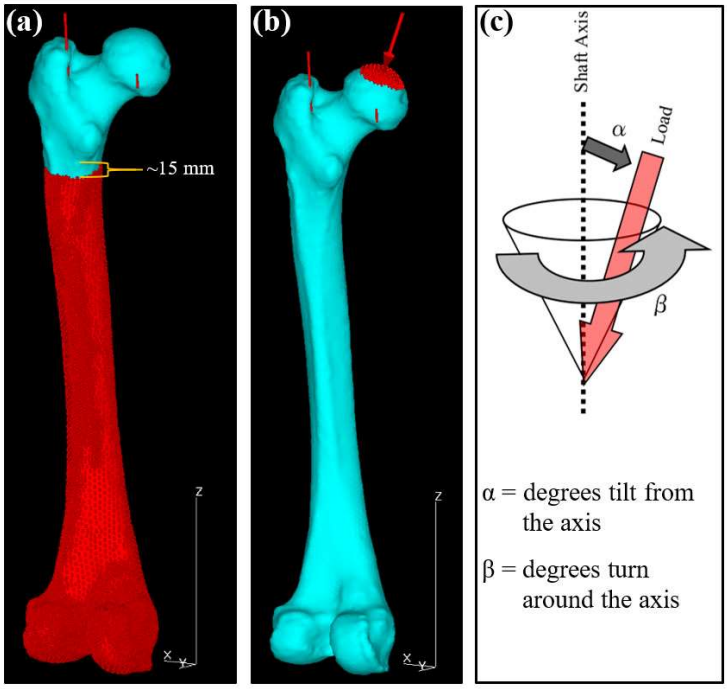

Figure 2.4: Boundary conditions: (a) fixed condition, (b) loading condition, and (c) angle specification in polar coordinate system to the bone axis.

2.3 Results and Discussion

2.3.1 Correlation Between Fracture Load and vBMD

It is well known that an average BMD has a strong correlation with the femoral strength; therefore, in this study, for each of the femoral models, the average volumetric BMD (vBMD) in the femoral head and neck region was obtained. The correlation between the fracture load and vBMD of the normal femurs is shown in Figure 2.5(a). After a linear regression was fitted on the data, Pearson's correlation coefficient was found to be r = 0.71, and it could be said that the higher vBMD tended to reuslt in the higher fracture load. Confidience interval (CI) statistics was also performed to precisely estimate the samples' mean. Both of 95% predicted bands and 95% confidence bands of the fitted curve are also shown in Figure 2.5(a) as well. The statistical results showed that the mean of 95% confidence interval was in a range from 3,308±682 to 3,872±667 N (mean±SD). This implyed that the mean fracture load of all 42 normal models existed within this range with 95% confident.

Similarly, for both the OA and AVN femurs, the correlations between the fracture load and vBMD are shown in Figure 2.5(b) and Figure 2.5(c), respectively. 95% CI means were observed in a range from 3,338±491 to 3,807±501 N for OA models and from 3,053±795 N to 4,414±692 N for AVN models, respectively. The Pearson's r values were also found to be 0.60 and 0.49, respectively. In contrast to the normal models, there were two outliers and one outlier from the 95% confidence band of OA and AVN models. These would affect the linear correlation of the fracture load and vBMD, and resulted in lower r values. It should be noted that the load range of AVN models was apparently

wider than those of the normal and OA models. This fact could be closely related to the peculiar structural and mechanical properties of AVN femurs, depending on their stage and severity such as the extent of crescent percentage of the articular surface and extent of collapsed surface [82]. The AVN femurs used in this study were classified in the 4 stages and therefore, the different stages could result in the broad range of fracture load. It was also to be noteworthy that the maximum value of vBMD of both OA and AVN femurs were significantly higher than that of the normal femur because of the severe deformation of the femoral head. The mean fracture loads of lower and upper 95% confidence interval and their descriptive statistical value for each femur type are listed in Table 2.2.

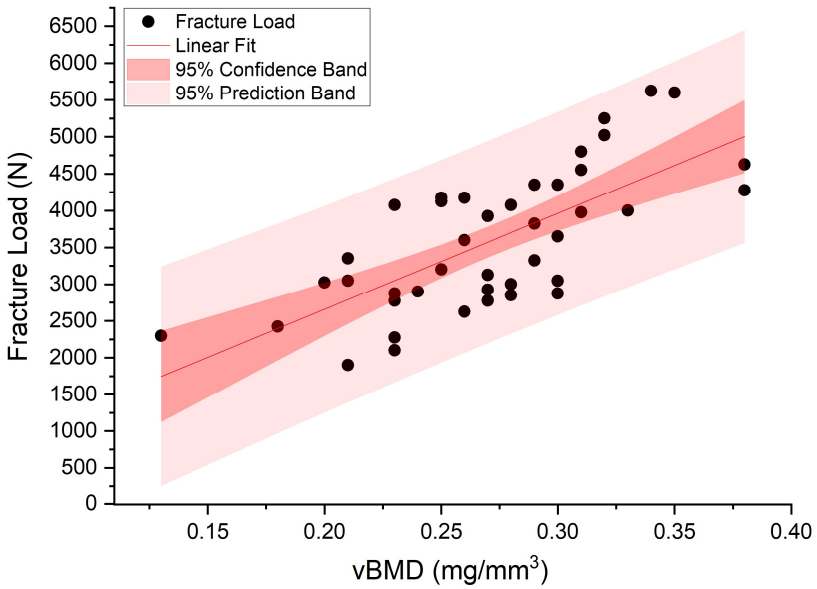

(a) Normal model

Figure 2.5: Correlation between fracture load and volumetric bone mineral density, including 95% interval of prediction band (pink color) and confidence band (light red color).

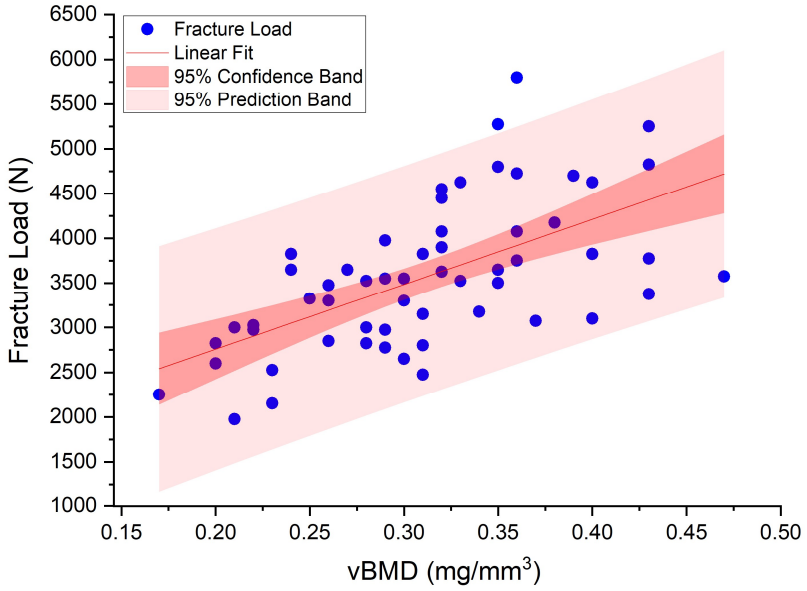

(b) OA model

Figure 2.5 (continued)

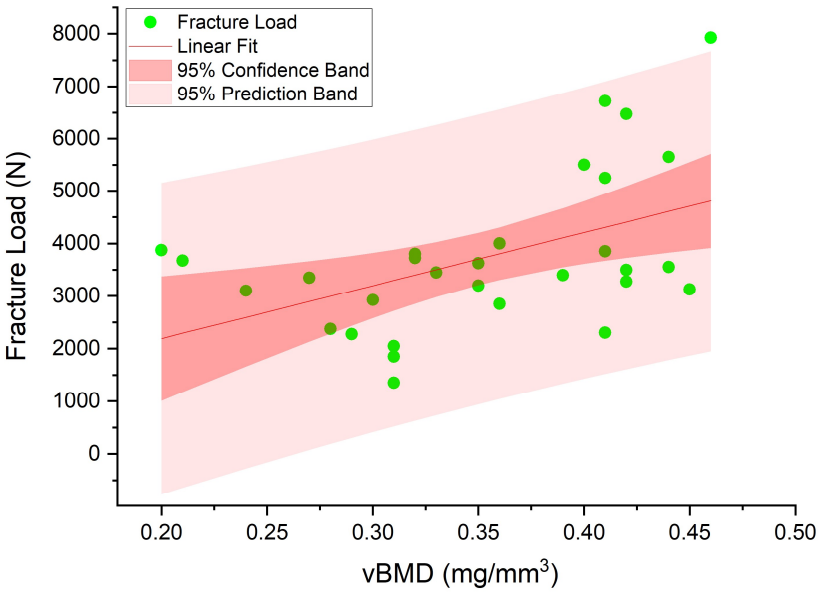

(c) AVN model

Figure 2.5 (continued)

Table 2.2: Mean fracture loads of individual femur group (unit: N)

Types of femur	Data	Mean	Standard Deviation	Minimum	Median	Maximum
Normal	Lower 95% Confidence Interval	3307	682	1125	3362	4510
	Upper 95% Confidence Interval	3872	667	2367	3781	5500
OA	Lower 95% Confidence Interval	3338	491	2136	3385	4280
	Upper 95% Confidence Interval	3807	501	2943	3730	5161
AVN	Lower 95% Confidence Interval	3053	795	1009	3256	3913
	Upper 95% Confidence Interval	4414	692	3373	4251	5711

2.3.2 Bone Fracture Behaviour

For each femoral model, the compressive fracture behaviour was expressed as the distribution of failure elements in the femoral head and neck region. Three different types of distribution of failure elements are shown for each of the femoral models in Figure 2.6. Those microdamages consisted of three different failure modes, that is, tensile fracture, compressive yielding, and compressive fracture. The fracture regions were classified into 4 different types as shown in Table 2.3. It was noted that the bone fracture mainly took place in the neck region (including at least one of subcapital, transcervical and basicervical areas) for all types of femoral model. In addition, a combination of the head and neck fracture was also observed in all the models. Especially, in which OA models showed as many as 16 out of 58 models. Moreover, 10 out of 58 OA models exhibited fractures in their head regions. It was reasonably considered that OA femurs have a higher fracture risk in the head region compared to the normal and AVN femurs. This might be related to the deformity of the femoral head due to OA. On the other hand, a

combination of neck and intertrochanteric fracture was also observed in the normal and AVN groups. This type of fracture highly happened in the AVN femurs (10 out of 30). More importantly, AVN femurs might fracture in all possible locations. It could be due to the variety of AVN stages. It is also to be noteworthy that the AVN femurs with potentially intertrochanteric fracture were mostly with stage 3 and above, whereas head fractured AVN femurs were all stage 4 with serious femoral head collapse.

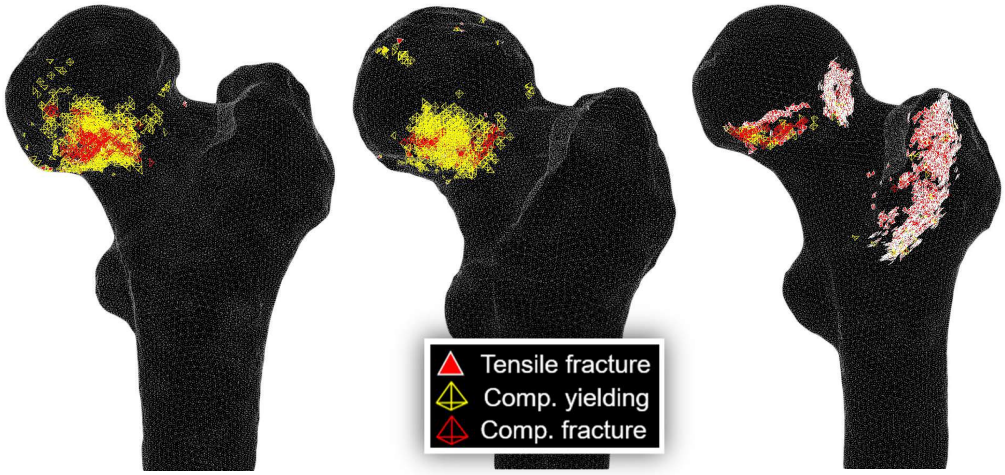

(a) Normal models

Figure 2.6: Three different types of bone fracture behaviour. Fracture patterns were expressed as the distribution of failure elements.

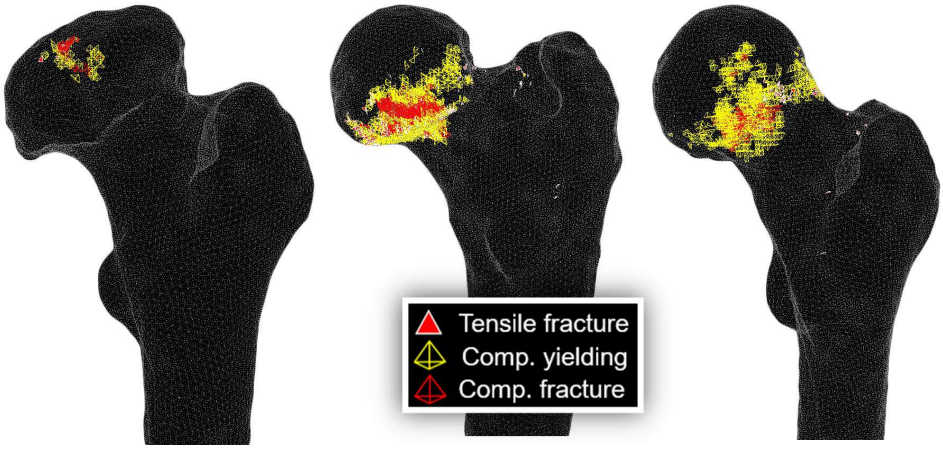

(b) OA models

Figure 2.6 (continued)

(c) AVN models

Figure 2.6 (continued)

Table 2.3: Classification of fracture regions

Type of Femur	Fracture Region			
	Head	Neck	Head + Neck	Neck + Intertrochanteric
Normal (N=42)	-	N=36 (86%)	N=3 (7%)	N=3 (7%)
OA (N=58)	N=10 (17.2%)	N=32 (55.2%)	N=16 (27.6%)	-
AVN (N=30)	N=3 (10%)	N=13 (43.4%)	N=4 (13.3%)	N=10 (33.3%)

2.3.3 Comparison of Fracture Mechanism of Three models with same vBMD

Among all the 130 femoral models, it was found that some of them had the same vBMD with very different fracture load. In order to understand the difference of fracture mechanism, three models denoted by A-normal, B-OA and C-AVN with the same vBMD of 0.31 mg/mm^3 were picked up. The fractue load values of the three models were 4,800, 3,825, and 1,850 N, respectively.

For each of the three models, accumulation of failure elements is shown as a function of load step in Figure 2.7. One step of load corresponded to 250 N. The strongest model, A-normal, reached up to 20 steps with low number of failure elements (1528), while the weakest model, C-AVN, reached only 8 steps with very large number of failure elements (13367). B-OA model reached 16 steps with the relatively low number of failure elements (1973). Distribution of strain energy density (SED) on the cross-sections of the three models at the fracture load are also shown in Figure 2.8. In A-normal and B-OA models, it was clearly seen that high SED smoothly distributed from the femoral head to the medial cortical bone, suggesting an ideal propagation of mechanical stress from the top surface of femoral head to the stiff and strong cortical

bone and resulting in the high fracture load. On the contrary, in C-AVN model, SED was unnaturally concentrated on the lateral side of neck where BMD and Young's modulus were much lower than the medial side, indicating that neck fracture occurred easily. This unnatural SED concentration was obviously owing to the unique leaning shape of the head and neck region, which caused greater bending moment under the compressive loading, resulting in the localized SED concentration.

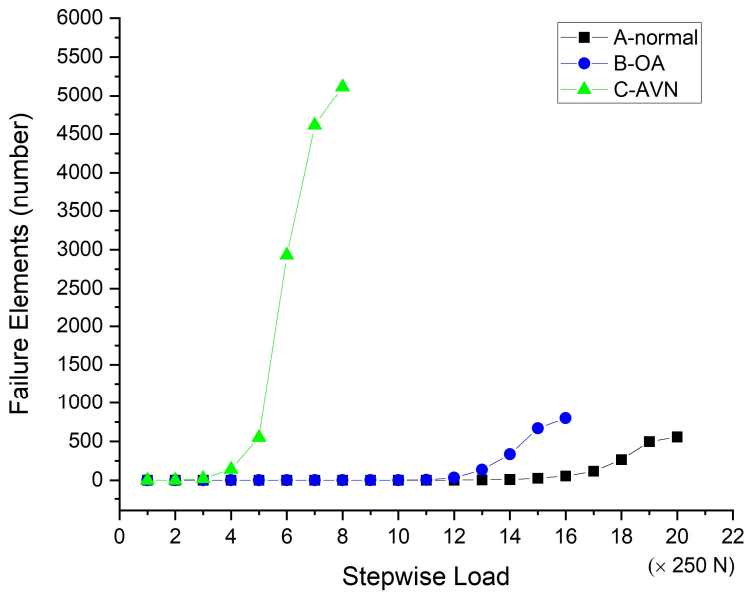

Figure 2.7: Failure elements against load steps in the three femoral models with the same vBMD.

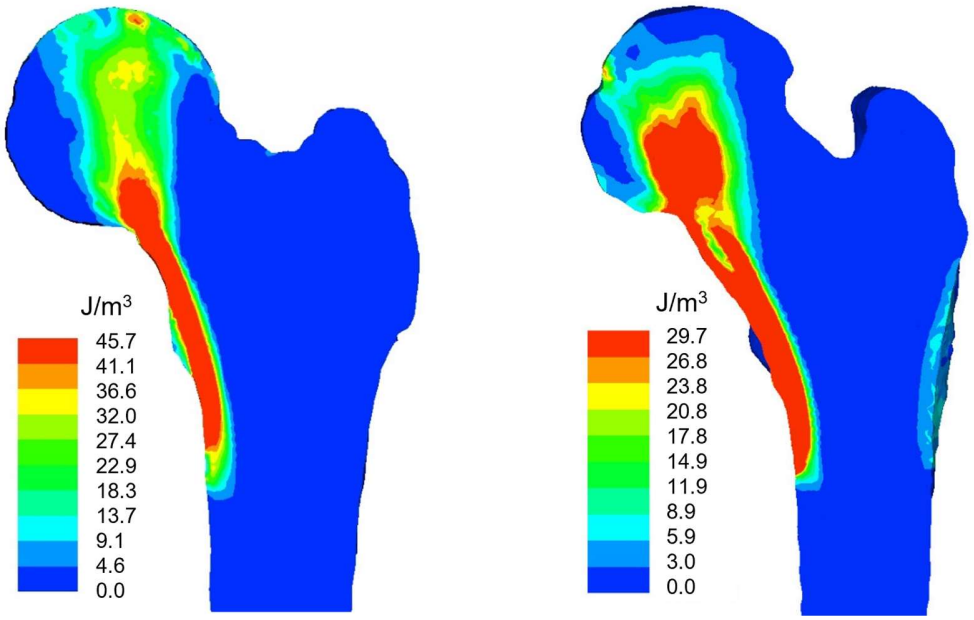

(a) A-normal model (b) B-OA model

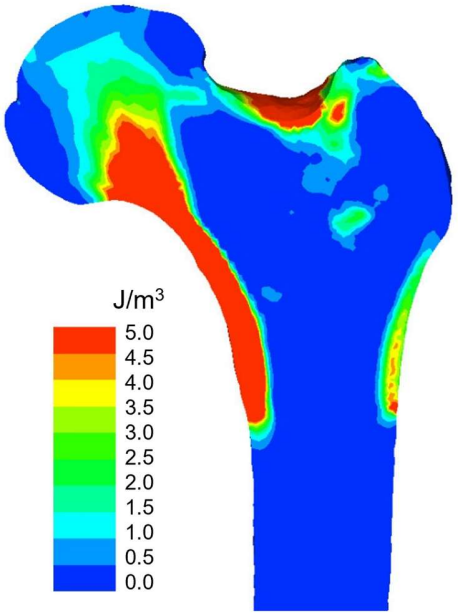

(c) C-AVN model

Figure 2.8: SED distribution patterns of three femoral models with the same vBMD.

2.4 Conclusion

In this study, normal, OA and AVN femoral FE models were constructed using medical CT images. Then, the fracture load as the patient-specific femoral strength and the fracture location were analyzed by the FEA combined with a damage mechanics analysis. The conclusions were obtained as follows:

(1) The fracture load tended to increase with increase of the average vBMD of the head and neck with wide scatters. The Pearson's r values of normal, OA and AVN models were evaluated as 0.71, 0.60 and 0.49, respectively, corresponding to the widest scatter observed in AVN models.

(2) The bone fracture behaviour was expressed as appearing as the distribution of failure elements in the head and neck region. It was noted that the bone fracture mainly took place in the neck region for all types of femoral model. In addition, a combination of the head and neck fracture was also observed in all the models.

(3) A combination of neck and intertrochanteric fracture was also observed in the normal and AVN groups. This type of fracture highly happened in the AVN femurs.

(4) Three models, A-normal, B-OA and C-AVN model, with the same vBMD were compared. C-AVN exhibited the lowest fracture load with the largest number of failure elements generated at the low level of load. In C-AVN model, SED was unnaturally concentrated on the lateral side of neck where BMD and Young's

modulus were much lower than the medial side, indicating that neck fracture occurred easily.

CHAPTER 3

BONE FRACTURE ANALYSIS UNDER SIDEWAYS FALL

3.1 Overview

Sideways falling has been considered as a leading cause of hip fracture in elderly people with a high risk of morbidity and mortality. It has been reported that the impact forces encountered during a sideways resulted in over 90% of hip fractures [83,84]. Early investigation of optimum femoral strength and fracture location of people at greatest risk can therefore be clinically useful for the preventive measures. In this Chapter, 130 computational femoral models of the normal, OA and AVN femurs were constructed using CT images of 73 patients. Then, CT image based finite element method (CT-FEM) combined with a damage mechanics analysis was applied to predict the fracture load as the femoral strength and the fracture location of the femoral models. The computational results exhibited that the fracture load tended to increase with increase of the volumetric bone mineral density (vBMD) estimated in the femoral head and neck region in all the three types of models. The bone fracture behaviour was expressed as expressed as the distribution of failure elements in the head and neck region. Under fall loading, the bone fracture mainly took place in the greater trochanter region for all types of femoral model. In addition, a combination of the greater trochanter and multifarious neck fracture was also observed in all the models. A combination of greater trochanter and intertrochanteric fracture was also observed in the AVN group.

3.2 Analytical Methods

3.2.1 Finite Element Modelling

Femoral CT data of 73 patients (10 men aged 37-75 years old, the average age of 51.49 years old; and 63 women aged 19-87 years old, the average age of 65.06 years old) were collected from four different universities hospitals located in the northern Kyushu Island, Japan. From these CT images, a total of 130 computational femoral models were constructed. Based on the patient's clinical data confirmed by orthopaedic surgeons, the 130 femurs were classified into three groups; a normal of 42 femurs (N1 group), OA of 58 femurs (N2 group) and AVN of 30 femurs (N3 group). The three different types of the femur are illustrated in Figure 3.1.

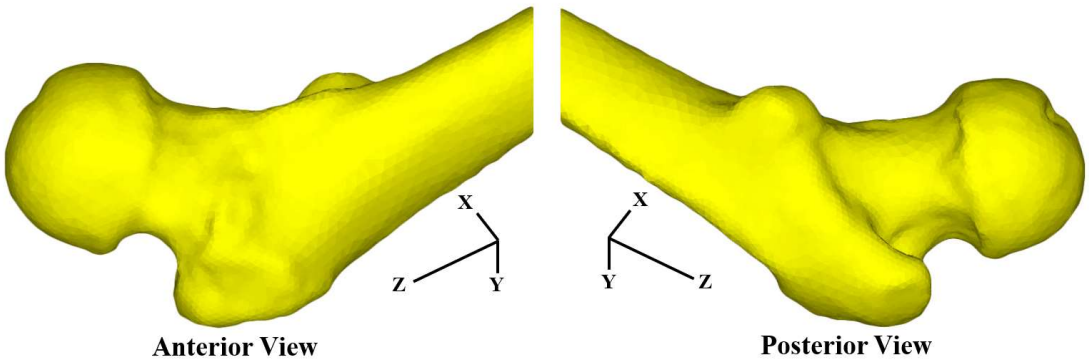

(a) Normal model

Figure 3.1: Three different types of femoral models.

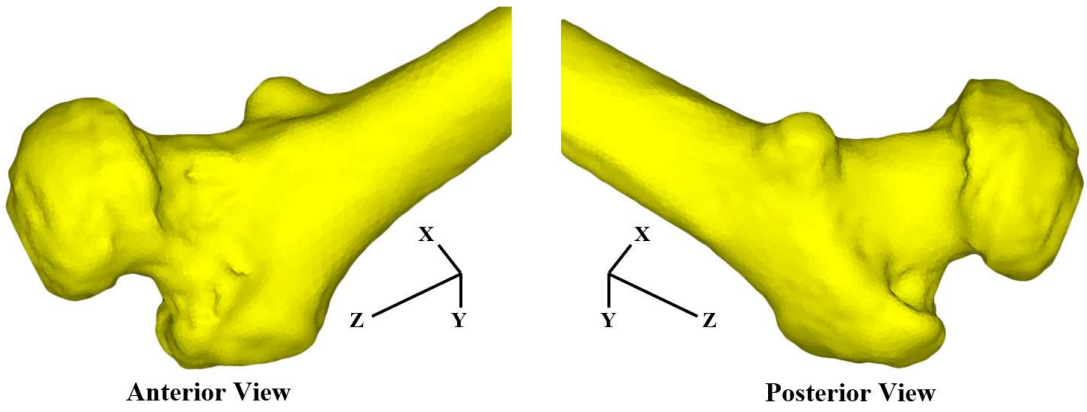

(b) OA model

Figure 3.1 (continued)

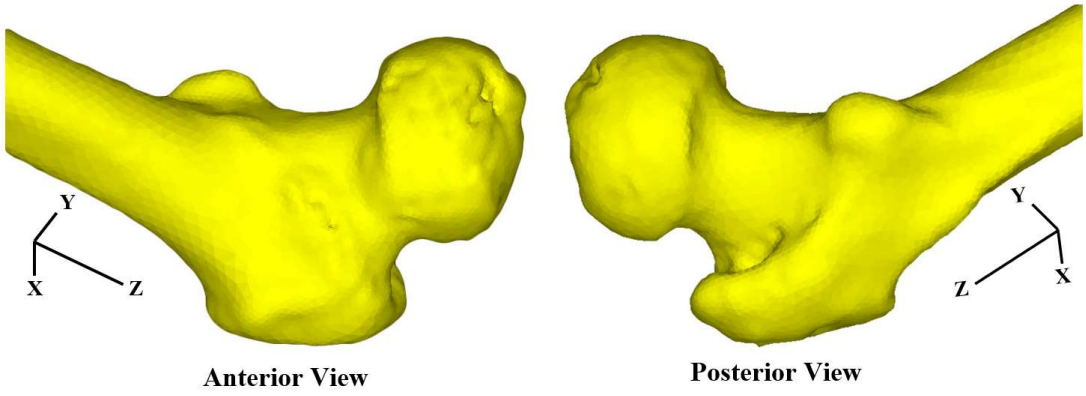

(c) AVN model

Figure 3.1 (continued)

Three-dimensional numerical and finite element models were constructed using Mechanical Finder v.11 (Research Center of Computational Mechanics Inc., Tokyo, Japan). Firstly, the two-dimensional contours of a femur were extracted from the corresponding CT images, and they were smoothly connected each other to construct 3D femoral model. Then, the inside of the femoral model was filled with the tetrahedral elements to create a finite element (FE) model for the computational mechanical analysis as shown in Figure 3.2 [74]. The size of the tetrahedral elements was set to 2 to 4 mm. The whole surface of the FE model was also generated using the shell elements to imitate the stiff outer surface of the cortical bone with the greatest bone mineral density [75]. The number of solid elements included in our models was an average of 178,259, and that of shell elements was of 28,475, depending on the size of the femur.

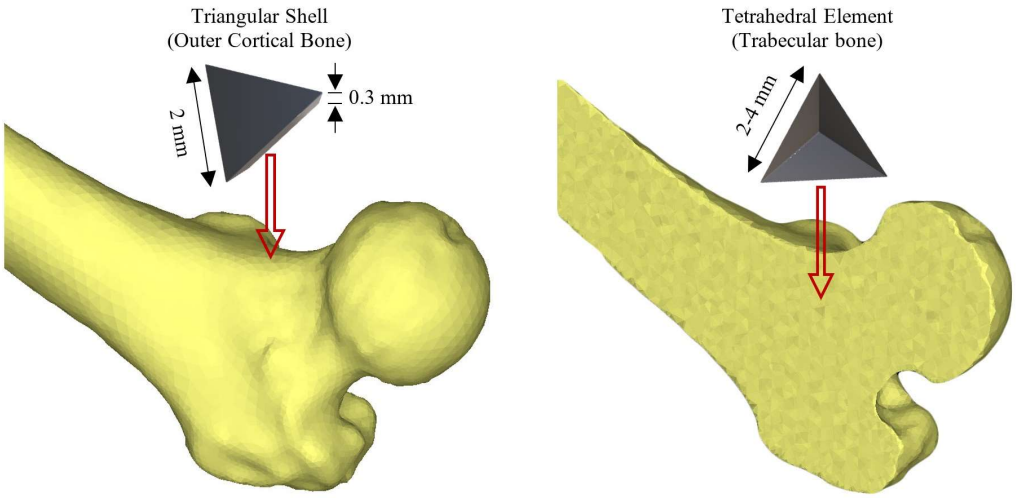

(a) Shell element (b) Trabecular solid element

Figure 3.2: FE Femoral model. The triangular shell elements were used to model the outer cortex. (a), and the trabecular bone and the inner portion of cortical bone were designed using linear tetrahedral elements (b).

3.2.2 Mechanical Modelling and Material Properties

The tensile deformation behaviour of all the femoral bone models was assumed to be linear elastic characterized by two material parameters such as Young's modulus and Poisson's ratio, while their compressive deformation behaviour was assumed to be characterized by an elastic-plastic response with four material parameters such as Young's modulus, Poisson's ratio, yield strength and the work hardening coefficient.

For each of the tetrahedral elements, its mean BMD was firstly calculated from the corresponding CT value (CTv) by using the linear equation (1) that was mentioned in Chapter 2. Then, Young's modulus of the element was estimated from the corresponding BMD by using the empirical formulae proposed by Keyak as described Chapter 2 as well. For all the tetrahedral elements, Poisson's ratio was set to 0.4 [57]. On the contrary, for all the shell elements, Young's modulus and Poisson's ratio were fixed to 20.6 GPa and 0.167, respectively. The distribution patterns of Young's modulus in the three femoral models presented in Figure 3.1 are shown in Figure 3.3. Distribution of the higher moduli corresponded to the location of cortical bone, while the lower moduli expressed cancellous bone and marrow.

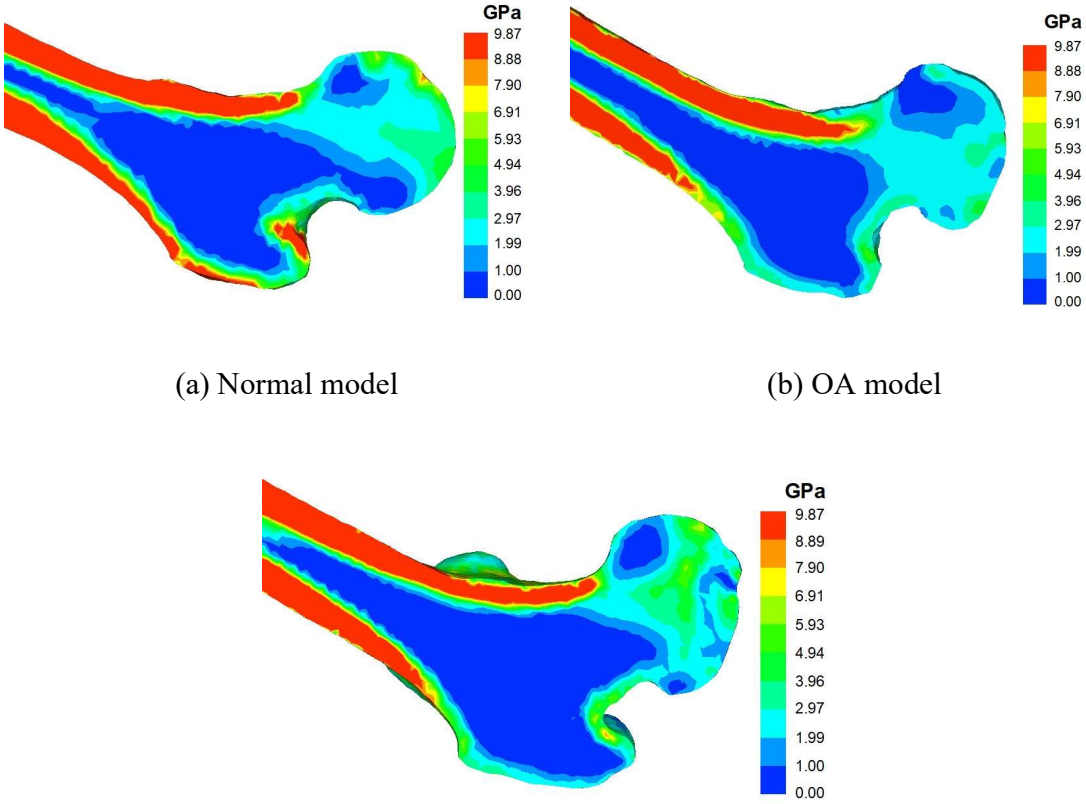

(a) Normal model (b) OA model

(c) AVN model

Figure 3.3: Distribution of Young's modulus in the cross-sectional area.

Under the compressive deformation of all the elements, it was assumed that the onset of yielding took place when the Drucker-Prager equivalent stress reached the compressive yield strength (this is called 'Drucker-Prager yield criterion'). The yield strength of each element was also obtained from the element's BMD by using the empirical formulae proposed by Keyak too, while the yield strength of all the shell elements was set to 20.6 MPa. The work hardening coefficient was set to 0.07 for all the elements.

3.2.3 Element Failure Criteria

In this FE analysis under sideways falling, bone fracture was reproduced as an aggregation of failure elements. Different failure criterions were used in the tensile and compressive stress conditions. Under the tensile stress condition, the maximum principal stress criterion was utilized to express the onset of tensile bone fracture. It was assumed that the tensile failure of an element took place when the maximum principal stress reached its critical value, which was equal to 0.8 × (compressive yield strength) [79]. On the contrary, under the compressive stress condition, the minimum principal strain criterion was used to express the compressive bone fracture. It was assumed that the compressive failure of an element took place when the minimum principal strain reached its critical value which was equal to -10,000 μ strain, following the yielding of the element [80]. The failure of the element under both tensile and compressive conditions was expressed by reducing the modulus down to the minimum value in the whole femoral model. The strength of the femoral model was then defined as a critical value of the applied load when 15 shell elements were failed [81].

3.2.4 Boundary and Loading Conditions

Firstly, the bone axes were set on the basis of the femoral method and then, the boundary conditions were determined accordingly. The boundary conditions, i.e., the fixed and loading conditions, are shown in Figure 3.4, respectively. As the fixed condition, the femoral surface from the bottom condylar surface to the line on the diaphysis located approximately 15 mm below the lesser trochanter and the base of the

greater trochanter were totally fixed as shown in Figure 3.4(a). The distributed load was applied to the femoral head vertically to the floor with the femoral shaft slanted by 60° and internally rotated by 15° in reference to the floor as shown in Figure 3.4(b). The total value of the applied load was set to 10,000 N. The total load was divided into 10 main steps and each of the main steps was also divided into 4 sub-steps. Concerning the loading direction, α was defined as the angle between the long axis of the femur and the horizontal floor while β is the angle regarding the femoral neck axis in the horizontal floor as shown in Figure 3.4(c) [54,85].

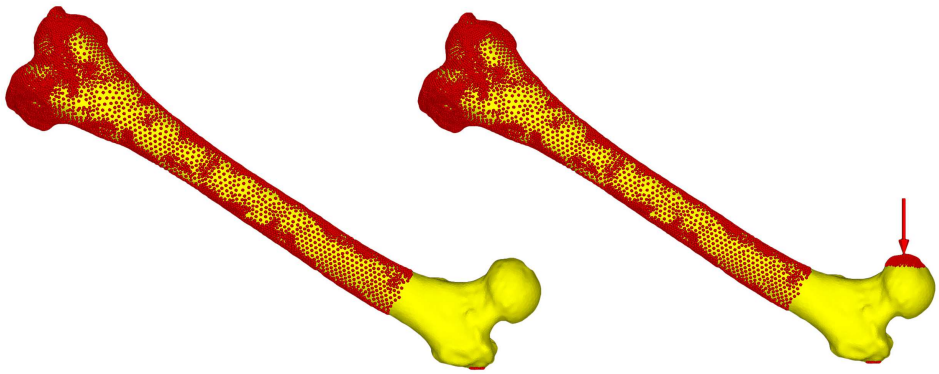

(a) fixed condition (b) loading condition

Figure 3.4: Boundary conditions under fall configuration.

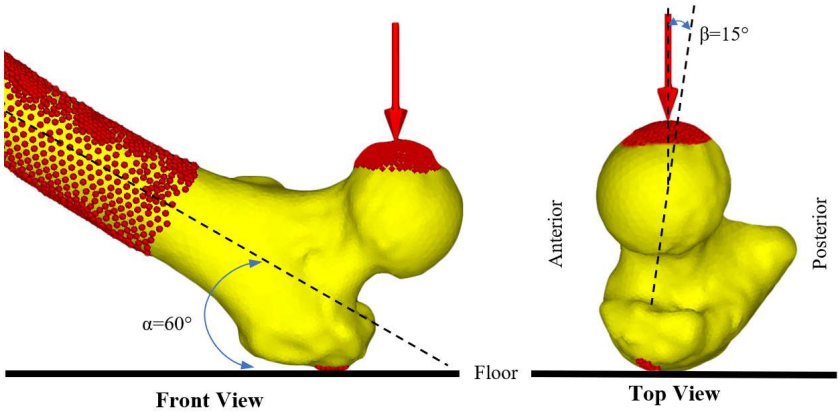

(c) angle specification

Figure 3.4 (continued)

3.3 Results and Discussion

3.3.1 Correlation Between Fracture Load and vBMD

It is well known that an average BMD has a strong correlation with the femoral strength; therefore, in this study, for each of the femoral models, the average volumetric BMD (vBMD) in the femoral head and neck region was obtained. The correlation between the fracture load and vBMD of the normal femurs is shown in Figure 3.5(a). After a linear regression was fitted on the data, Pearson's correlation coefficient was found to be r = 0.53, and it could be said that the higher vBMD tended to reuslt in the higher fracture load. Confidience interval (CI) statistics was also performed to precisely estimate the samples' mean. Both of 95% predicted bands and 95% confidence bands of the fitted curve are also shown in Figure 3.5(a) as well. The statistical results showed that the mean of 95% confidence interval was in a range from 896±186 to 1,157±151 N

(mean±SD). This implyed that the mean fracture load of all 42 normal models existed within this range with 95% confident.

Similarly, for both the OA and AVN femurs, the correlations between the fracture load and vBMD are shown in Figure 3.5(b) and 3.5(c), respectively. 95% CI means were observed in a range from 1,054±154 to 1359±170 N for OA models and from 962±222 to 1,369±166 N for AVN models, respectively. The Pearson's r values were also found to be 0.42 and 0.43, respectively. It should also be noted that the load ranges of OA and AVN models were apparently wider than that of the normal models. This fact could be closely related to the peculiar structural and mechanical properties of OA and AVN femurs, depending on the extra bone growths induced by femoroacetabular impingement (FAI) in OA femurs and various stages of collapsed femoral head surface in the AVN femurs [82]. The AVN femurs used in this study were classified in the 4 stages and therefore, the different stages could result in the broad range of fracture load. The mean fracture loads of lower and upper 95% confidence interval and their descriptive statistical value for each femur type are listed in Table 3.1.

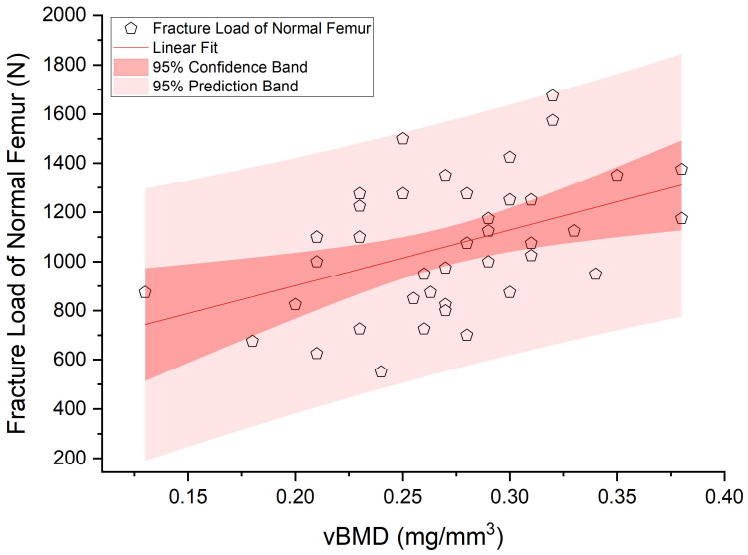

(a) Normal model

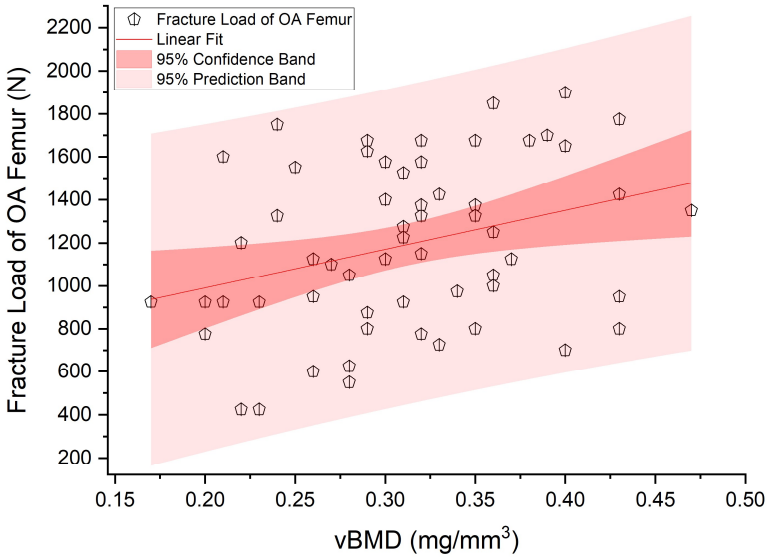

(b) OA model

Figure 3.5: Correlation between fracture load and volumetric bone mineral density, including 95% interval of prediction band (pink color) and confidence band (light red color).

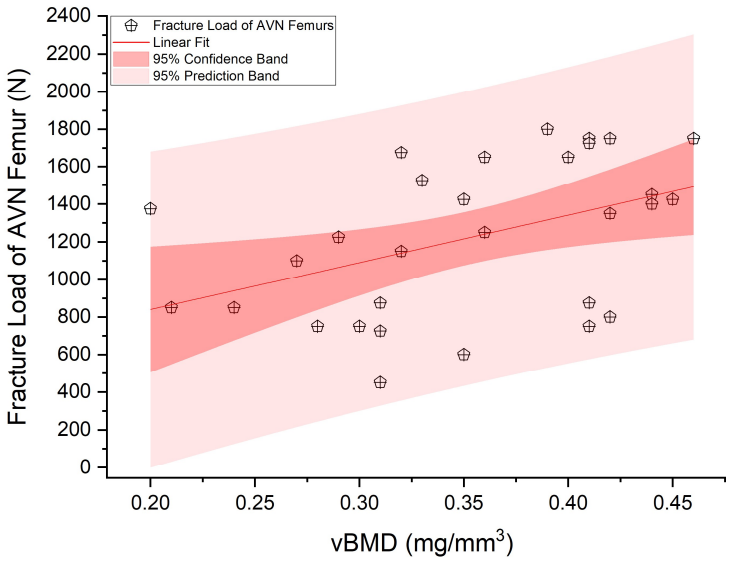

(c) AVN model

Figure 3.5 (continued)

Table 3.1: Mean fracture loads of individual femoral group (unit: N)

Types of femur	Data	Mean	Standard Deviation	Minimum	Median	Maximum
Normal	Lower 95% CI	896	186	513	945	1127
	Upper 95% CI	1157	151	973	1108	1493
OA	Lower 95% CI	1054	154	710	1109	1229
	Upper 95% CI	1359	170	1163	1304	1724
AVN	Lower 95% CI	962	222	504	1018	1237
	Upper 95% CI	1369	166	1175	1314	1747

3.3.2 Fracture Characteristics

For each femoral model, the compressive fracture behaviour was expressed as the distribution of failure elements. Three different types of these failure elements are shown for each of the femoral models in Figure 3.6. Those microdamages consisted of three different failure modes, that is, tensile fracture, compressive yielding, and compressive fracture. The fracture regions were classified into 5 different types as shown in Table 3.2. It was noted that the bone fracture mainly took place in the greater trochanter region, and which was secondly followed by a combination of greater trochanter and basicervical neck region for all types of femoral model. In addition, a combination of the greater trochanter and either subcapital neck or transcervical neck fracture was also observed in all models. Especially, in which OA models showed as many as 15 out of 58 models. On the other hand, a combination of the greater trochanter and intertrochanteric fracture was significantly occurred in the AVN group. This type of fracture only happened in the AVN femurs (4 out of 30) among the 3 groups. More importantly, AVN femurs might fracture in all possible locations. It could be due to the variety of AVN stages. It is also to be noteworthy that the AVN femurs with potentially intertrochanteric fracture mixed with greater trochanter were of stage-3 and stage-4.

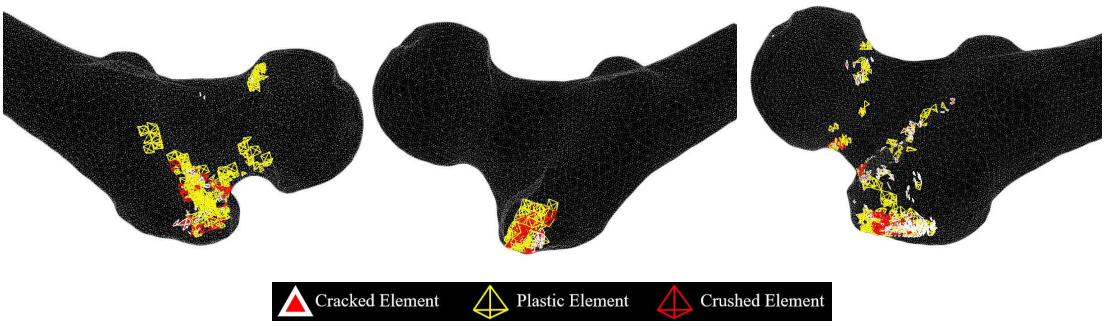

(a) Normal models

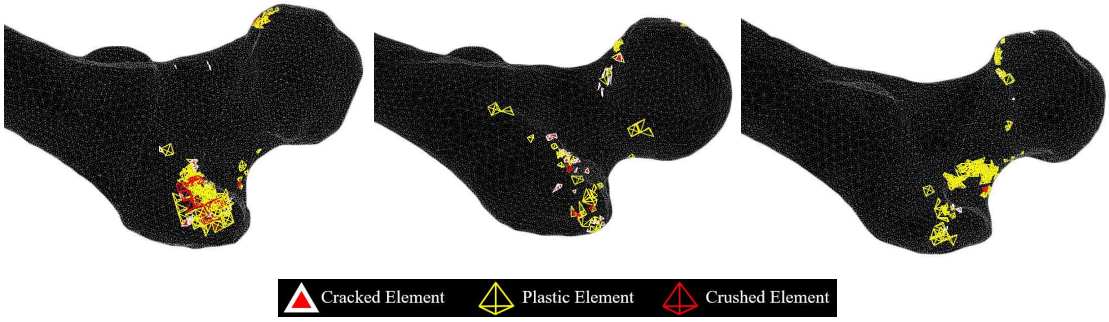

(b) OA models

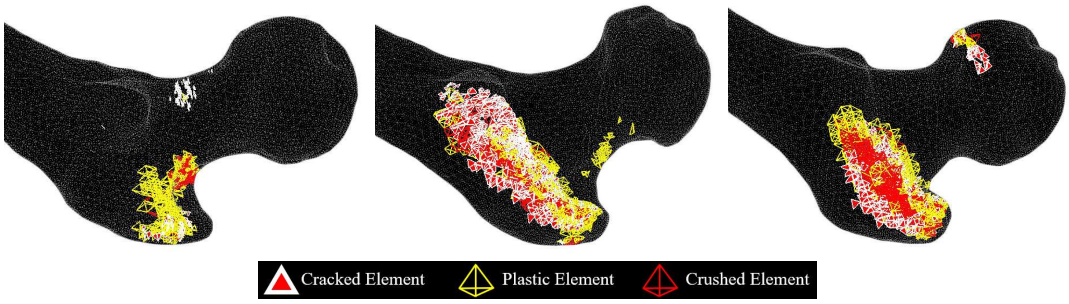

(c) AVN models

Figure 3.6: Three different types of bone fracture behaviour. Fracture patterns were expressed as the distribution of failure elements.

Table 3.2: Classification of fracture regions

Type of Femur (Sample Size)	Estimated Fracture Location				
	Greater Trochanter	Greater Trochanter + Neck (Subcapital)	Greater Trochanter + Neck (Transcervical)	Greater Trochanter + Neck (Basicervical)	Greater Trochanter + Intertrochanteric Region
Normal (N=42)	N=26, *61.9%*	N=3, *7.1%*	N=1, *2.4%*	N=12, *28.6%*	N=0
OA (N=58)	N=27, *46.5%*	N=12, *20.7%*	N=3, *5.2%*	N=16, 27.6%	N=0
AVN (N=30)	N=14, *46.7%*	N=1, *3.3%*	N=1, *3.3%*	N=10, *33.3%*	N=4, *13.3%*

* Neck (Subcapital) = the femoral head and neck junction
* Neck (Transcervical) = the mid portion of femoral neck
* Neck (Basicervical) = the base of femoral neck

3.3.3 Comparison of Fracture Mechanism of Three models with same vBMD

Among all the 130 femoral models, it was found that some of them had the same vBMD with very different fracture load. In order to understand the difference in fracture mechanism, three models denoted by A-Normal, B-OA and C-AVN with the same vBMD of 0.32 mg/mm^3 were picked up. The fractue load values of the three models were 1,650, 1,375, and 1,150 N, respectively. Their corresponding volumes of the head and neck region were compared in Figure 3.7, and it was obvious that the A-Normal model had a smallest volume but the highest femoral strength. On the contrary, the B-OA and C-AVN belonged to larger volumes with apparently lower fracture strengths. It is, therefore, well confirmed that the strength of a bone is greatly dependent on not only its geometry but also its matrix mineralization and microstructure of the trabecular network.

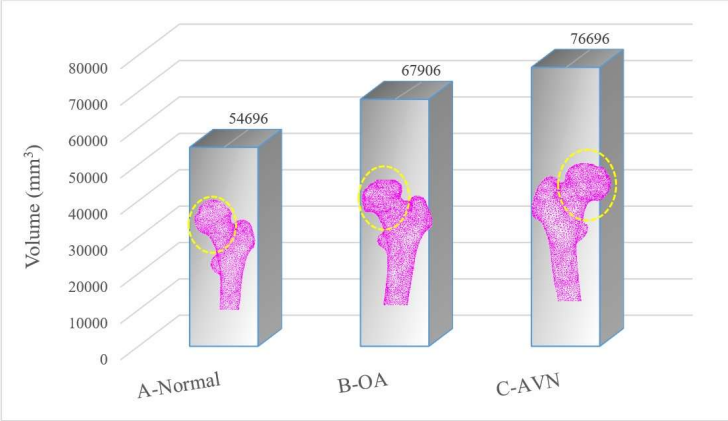

Figure 3.7: Comparison between the volumes of femoral head and neck region of three femoral models.

For each of the three models, accumulation of failure elements is shown as a function of load step in Figure 3.8. One step of load corresponded to 250 N. The strongest model, A-normal, reached up to 7, while the moderate model, B-OA, and the weakest model, C-AVN, reached only 6 and 5 steps, respectively. Distribution of strain energy density (SED) on the cross-sections of the three models at the fracture load are also shown in Figure 3.9. In A-normal and B-OA models, it was clearly seen that high SED smoothly distributed from the femoral head to the base of greater trochanter, suggesting an ideal propagation of mechanical stress and resulting in the high fracture load. On the contrary, in C-AVN model, SED was largely concentrated on the greater trochanter region with low BMD and Young's modulus, indicating a higher fracture risk.

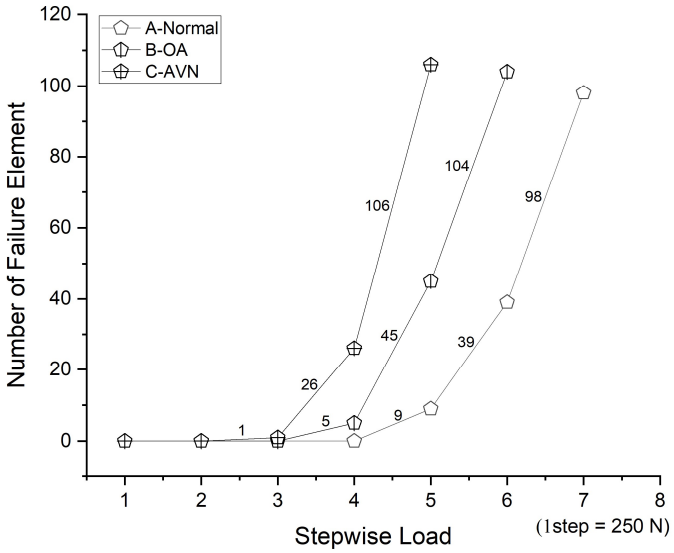

Figure 3.8: Failure elements against load steps in the three femoral models with the same vBMD.

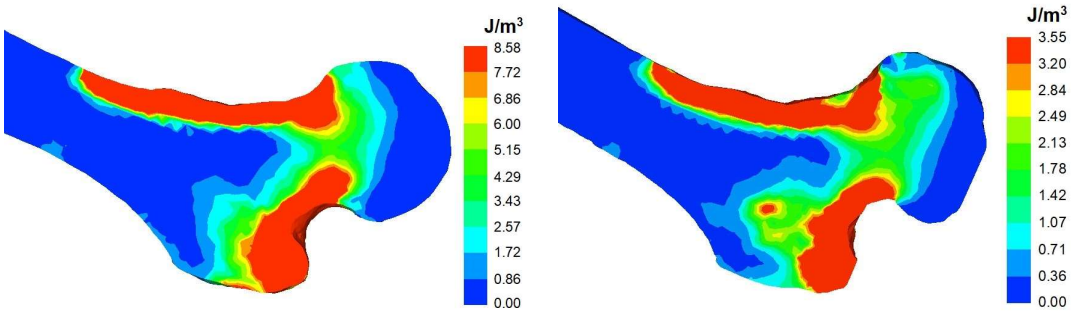

(a) A-Normal model (b) B-OA model

Figure 3.9: SED distribution patterns of three femoral models with the same vBMD.

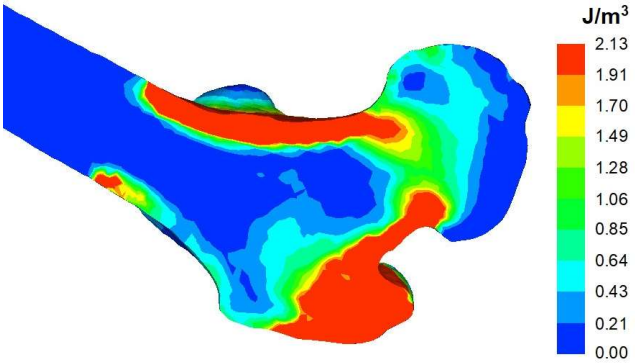

(c) C-AVN model

Figure 3.9 (continued)

Again, the correlations between the fracture behaviour and the compressive as well as shear stress were shown in Figure 3.10. The distribution patterns of the three femoral models revealed that the compressive stress (minimum principal stress) of the A-Normal femur was significantly higher than that of the B-OA and C-AVN femurs, and similarly for shear stresses. The corresponding values of compressive stress were -2.16 MPa, -1.38 MPa, and -0.98 MPa, respectively, and those of shear stress were 1.85 MPa, 1.13 MPa and 0.85 MPa, respectively. Shearing forces are unaligned forces pushing one part of a body in one direction, and another part of the body in the opposite direction. With this grasp, the most vulnerable area under shear forces could be in the neck region of the A-Normal femur, specifically at the subcapital portion. The high compressive stress as well as shear stress may result in an increase of fracture elements in this region, illustrated by dotted rectangular boxes and arrows in Figure 3.10 (a). On the other hand, such kind of fracture did not occur in the B-OA and C-AVN femurs with lower compressive and shear

stresses, indicating a potential fracture at the greater trochanter or/and basicervical neck region.

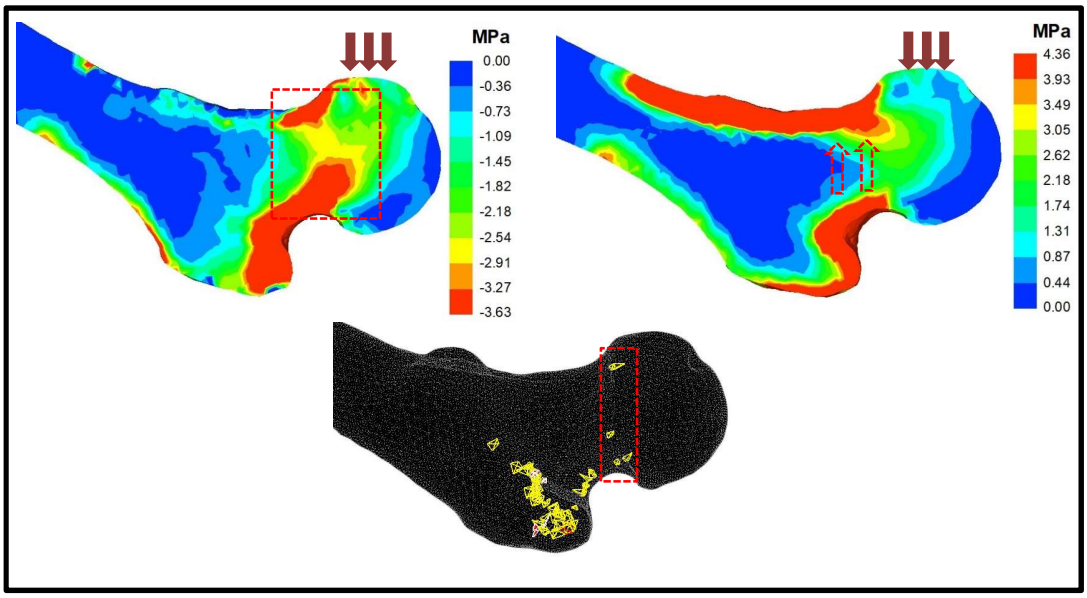

(a) A-Normal model

Figure 3.10: Distribution patterns of compressive stress (minimum principal stress), maximum shear stress and failure elements of three femoral models

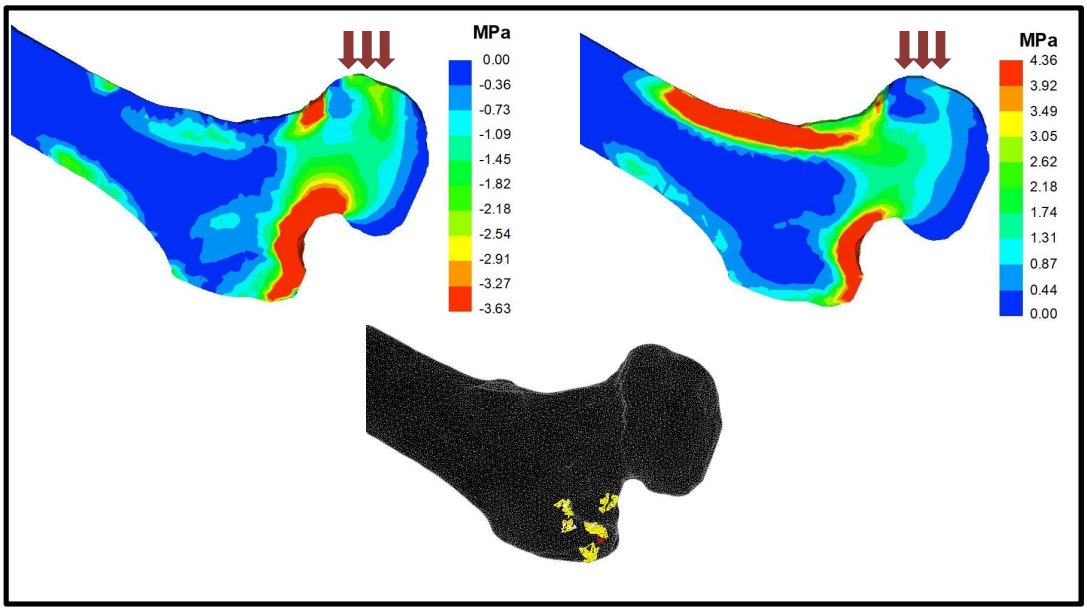

(b) B-OA model

Figure 3.10 (continued)

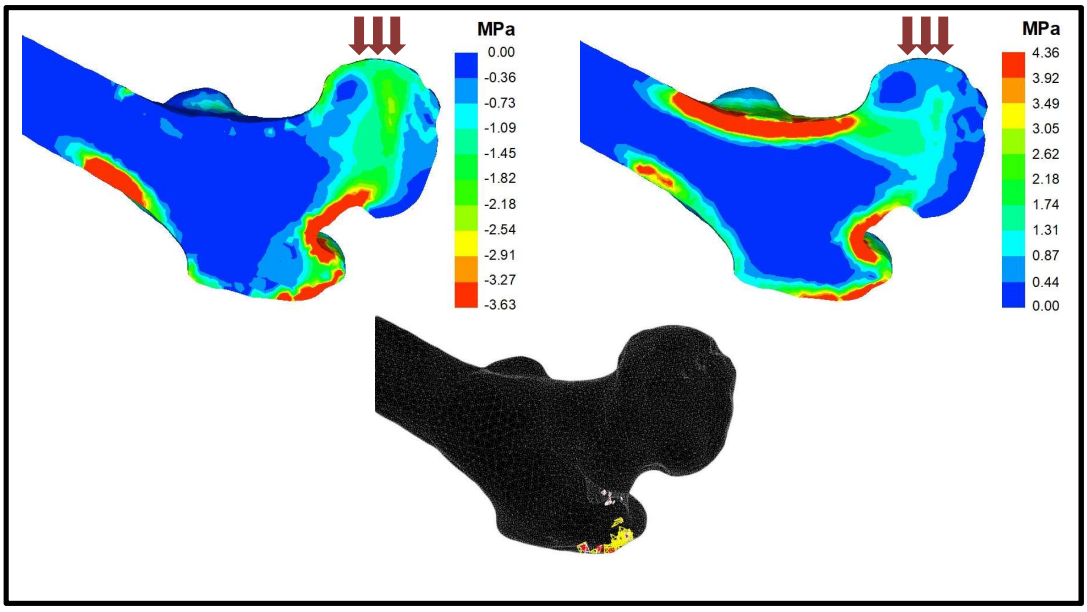

(c) C-AVN model

Figure 3.10 (continued)

3.4 Conclusion

In this study, normal, OA and AVN femoral FE models were constructed using medical CT images. Then, the fracture load as the patient-specific femoral strength and the fracture location were analyzed by the FEA combined with a damage mechanics analysis. Under the fall loading configuration, the conclusions were obtained as follows:

(1) The fracture load tended to increase with increase of the average vBMD of the head and neck with wide scatters. The Pearson's *r* values of normal, OA and AVN models were evaluated as 0.53, 0.42 and 0.43, respectively, corresponding to the wide scatters observed in OA and AVN models.

(2) The bone fracture behaviour was expressed as expressed as the distribution of failure elements in the neck and trochanteric regions. It was noted that the bone fracture mainly took place in the greater trochanter region for all types of femoral model. In addition, a combination of the greater trochanter and neck fracture was also observed in all the models.

(3) A combination of greater trochanter and intertrochanteric fracture was also observed in the AVN models, associated with disease level stage-3 and stage-4.

(4) Three models, A-normal, B-OA and C-AVN model, with the same vBMD were compared. C-AVN exhibited the lowest fracture load with unnatural SED distribution which concentrated on the greater trochanter side, indicating a higher risk of fracture than the other regions.

CHAPTER 4

BONE FRACTURE ANALYSIS UNDER CYCLIC LOADING

4.1 Overview

When a nominal load was repeatedly applied and then removed to and from a part of the material such as metal (known as cyclic load), the part would break after a certain number of load-unload cycles. However, the resultant maximum cyclic stress level was much lower than the ultimate tensile stress (UTS), and in fact, even lower than the yield stress (YS). The cyclic loading (fatigue analysis) was therefore considered to be useful for adapting more realistic FE femoral models, promising a better clinical usage. Therefore, along with compressive linear loading analysis, the cyclic loading analysis was also carried out in this study.

In Chapter 4, the standard models of elderly patients from each femoral group were analyzed in term of cyclic loading behaviour. The result showed that the normal and AVN models could resist the applied load until three cycles, and the average fracture load were 1,780 N and 1,520 N, respectively. As a matter of fact, the fracture loads were decreased to ≈ 26% for these models, and it was suggested that the strength in cyclic analysis was ≈ 0.74 times of the previous linear analysis. However, in the OA models, the fracture was occurred at two cycles, and the average fracture load was 1564 N. In addition, the average fracture load was largely decreased to ≈ 38% and it was supposed that its cyclic strength was ≈ 0.62 times of its previous linear one. These data of realistic FEM femoral models may be very useful for patient-specific clinical applications.

4.2 Analytical Methods

4.2.1 Modelling and Material Properties

In this study, 3 standard models from each femoral group; the normal, OA and AVN, total of 9 models, aged from 57 to 78 (average of 69.6 years) were selected and subjected to the cyclic loading. 3D FE models were constructed using MF v.11. The tetrahedral elements for filling inside of the femoral model and the triangular shell elements for imitating the stiff outer surface of cortical bone, were set in accordance with the physical and mechanical properties used in Chapter 2. The criteria for tensile and compressive deformation behaviour were also used accordingly. Using the empirical formulae proposed by Keyak, the Young's modulus and YS of the elements were estimated from the corresponding BMD that was calculated by the equation (1). The 3D FE models of the standard femora from the normal, OA and AVN types were shown in Figure 4.1, 4.2 and 4.3, respectively.

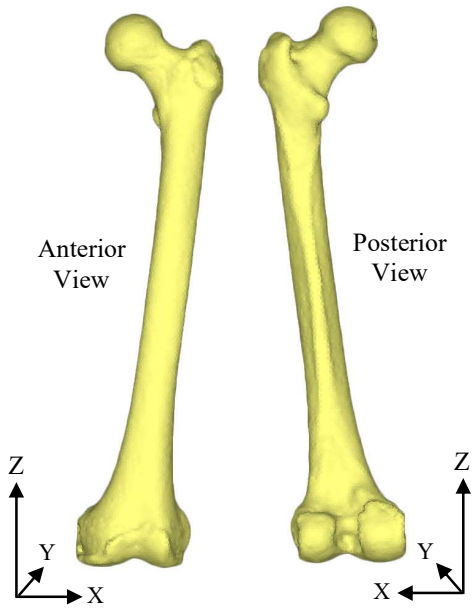

(a) normal-1 model

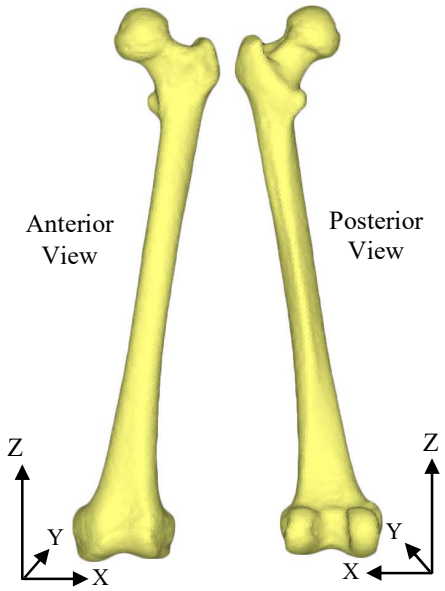

(b) normal-2 model

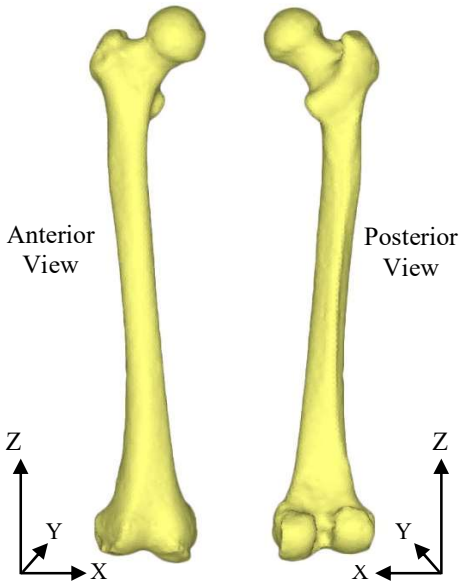

(c) normal-3 model

Figure 4.1: 3D FE models of the standard normal femora.

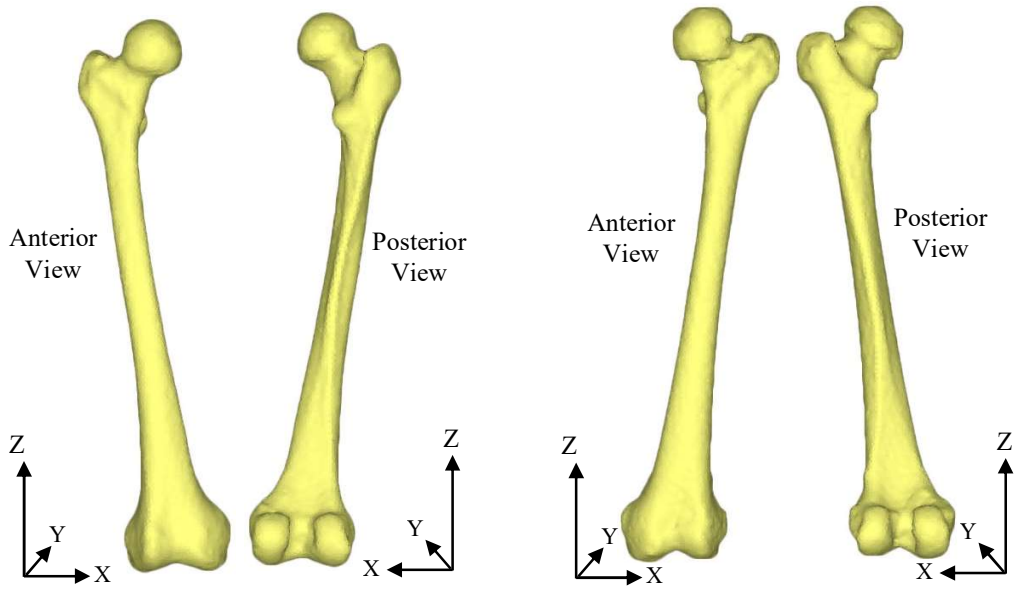

(a) OA-1 model

(b) OA-2 model

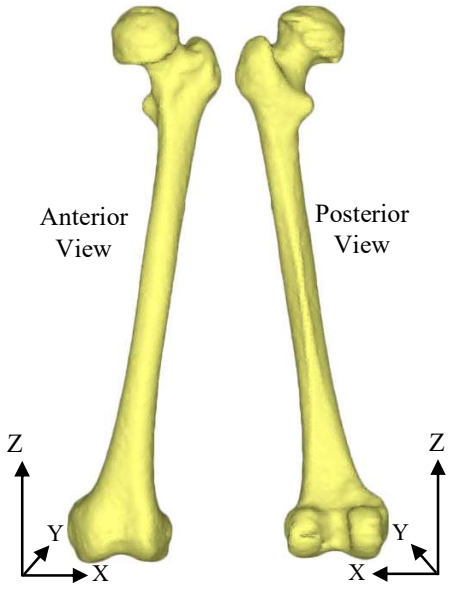

(c) OA-3 model

Figure 4.2: 3D FE models of the standard OA femora.

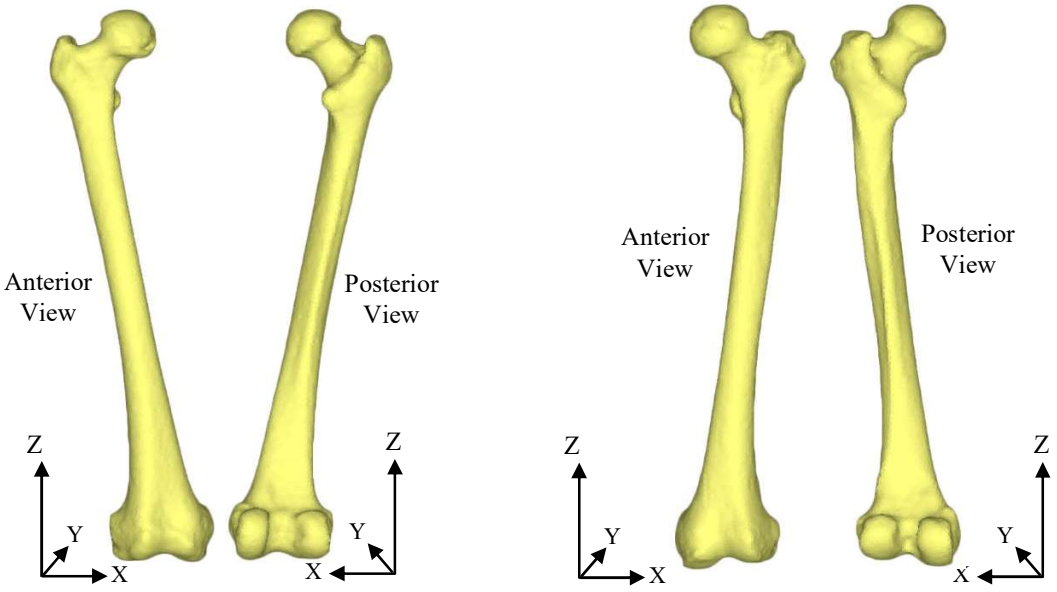

(a) AVN-1 model

(b) AVN-2 model

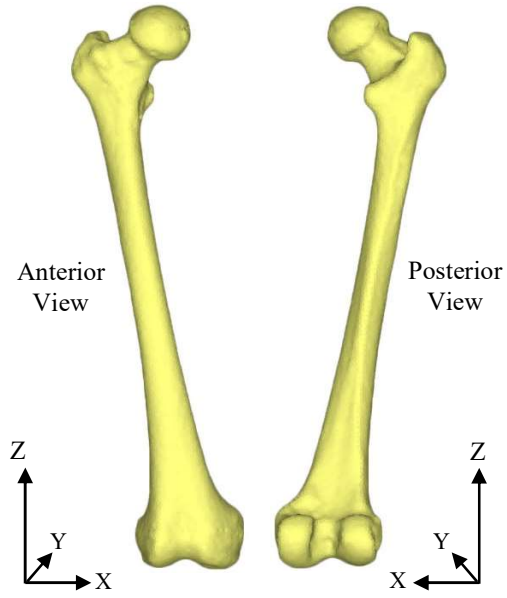

(c) AVN-3 model

Figure 4.3: 3D FE models of the standard AVN femora.

The distribution patterns of Young's modulus in each femoral model presented in Figure 4.1, 4.2 and 4.3 are shown in Figure 4.4, 4.5 and 4.6 accordingly. Distribution of the higher moduli corresponded to the location of cortical bone, while the lower moduli expressed cancellous bone and marrow.

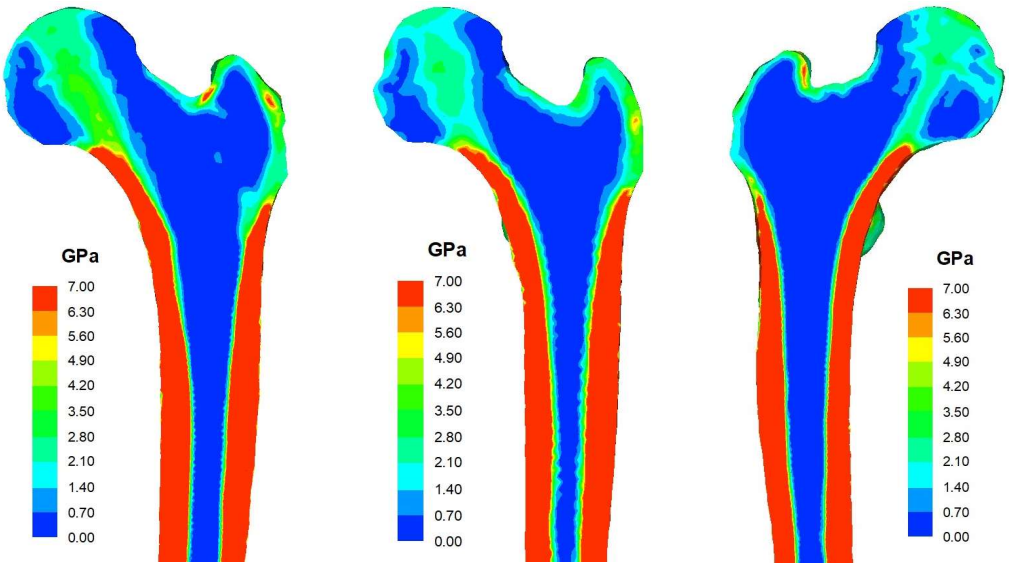

(a) normal-1 model (b) normal-2 model (c) normal-3 model

Figure 4.4: Young's modulus distribution in the mid-section of standard normal femurs.

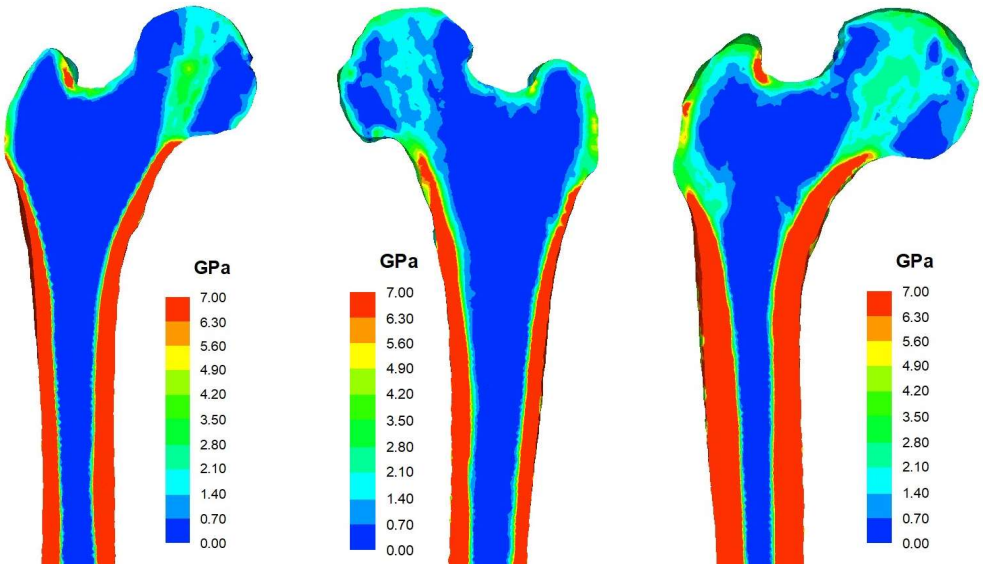

(a) OA-1 model (b) OA-2 model (c) OA-3 model

Figure 4.5: Young's modulus distribution in the mid-section of standard OA femurs.

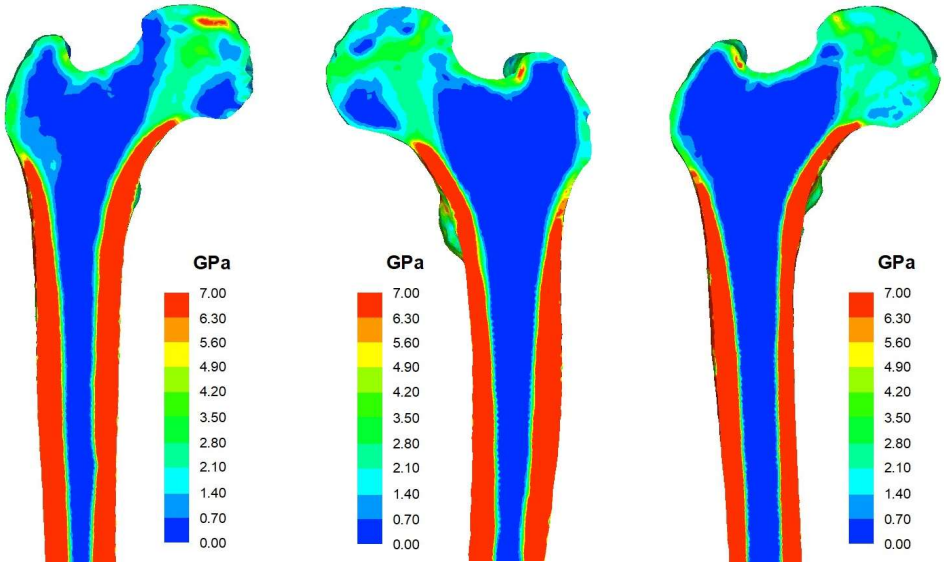

(a) AVN-1 model (b) AVN-2 model (c) AVN-3 model

Figure 4.6: Young's modulus distribution in the mid-section of standard OA femurs.

4.2.2 Description of Loading Profiles

In this cyclic loading analysis, there was a loading part and an unloading part in a one cycle of load, and the former was subsequently divided into 10 sub-steps so that the total output loops were 55 with total of five cycles. The time taken for each loading part with 10 sub-steps and each unloading part was set to 0.1 s. The constructed FE femoral models were subjected to the compressive load ranged from 1,380 N to 2,000 N depending on the onset of failure solid elements occurred in the previous linear loading analysis. The linear loading profile that was used in previous chapters and the cyclic loading profile were distinguished in Figure 4.7.

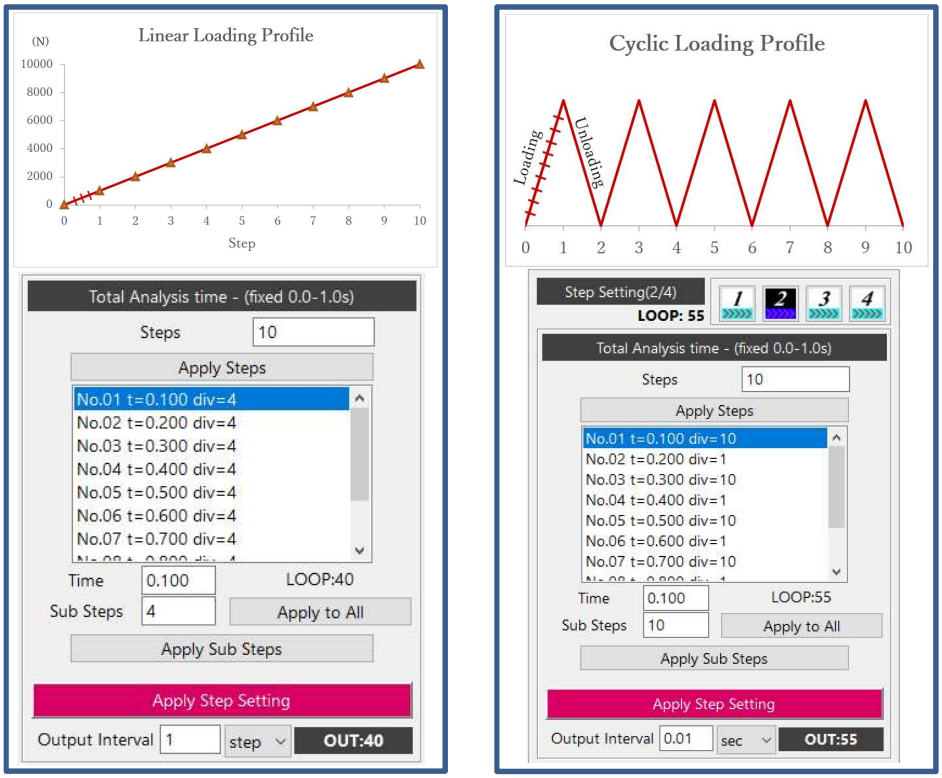

Figure 4.7: Description of different loading profiles.

4.2.3 Determination of Cyclic Strengths

The cyclic strength of the individual model was determined by following criteria:

(1) A maximum load for cyclic process was firstly investigated from the vicinity of onset point of failure elements resulted from the linear loading analysis under stance configuration as displayed in Figure 4.8. It was then used as a virtual compressive load for the specific model.

(2) When the investigated maximum load was applied to the corresponding model, the solid failure elements (crack, crush and plastic) at the onset and termination steps were monitored with 15 shell elements limitation. Subsequently, the cyclic fracture load was determined as a cyclic strength.

(3) If the termination/fracture point occurred during 1st cycle as shown in Figure 4.9, it was assumed that the applied load was still in a state of high level for bone fatigue failure. Then, the load was step-wisely reduced by 5%, and reanalyzed the process.

(4) Starting from 2nd cycle, the fracture load at the final failure point was determined as the cyclic strength of the model.

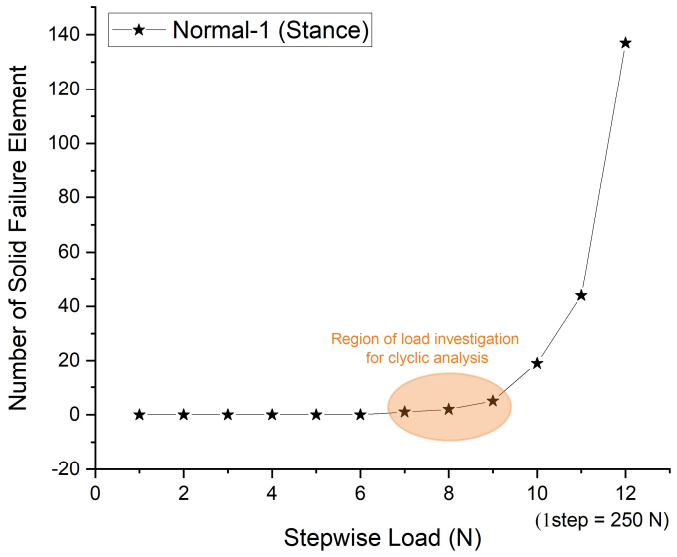

Figure 4.8: Investigation of maximum applied load for cyclic analysis

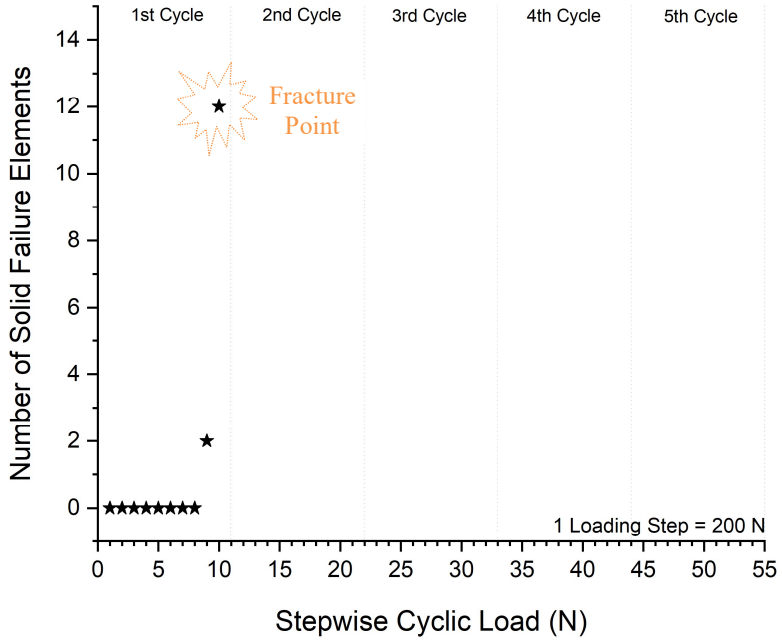

Figure 4.9: Cancellation of cyclic strength determination in which the final fracture occurred during 1st cycle.

4.3 Results and Discussion

4.3.1 Cyclic Strength of different femoral models

When the virtual compressive load was applied to the normal models in accord with cyclic profile, the fracture points were found at the 3rd cycle of a given continuous and repeated loading range in each model. The cyclic fracture loads of the normal-1, normal-2 and normal-3 models were 2,000 N, 1,820 N and 1,383 N, respectively as shown in Figure 4.10. Accordingly, the number of accumulated failure elements were 61, 2079 and 39043, respectively, indicating the stronger bone with the lesser element failure. Although both the tensile and compression failure were observed in all models, the normal-1, normal-2 models seemed to yield their compressive strength without element crushing. In contrast, the normal-3 model showed a compressive fracture with a plenty of crushed element, indicating a high vulnerability with poorest mechanical properties.

On the other hand, the fracture loads of the OA-1, OA-2 and OA-3 models were found to be 1,600 N, 1,436 N and 1,656 N, respectively as shown in Figure 4.11. The number of failure elements were not many and much different from one model to another. Among them, OA-3 model showed a highest cyclic strength resulted from its greater physical and mechanical properties such as BMD and Young' modulus. It is also to be noted that all OA models encountered their final fracture at the 2nd cycles of a given loading range, indicating low mechanical strength compared to the other types. Moreover, there were no plastic and crushed failure elements but cracked elements only were observed in OA-2 and OA-3 models, and it was obvious that their cyclic strengths were significantly lower than corresponding compressive yield strength.

For the AVN models; AVN-1, AVN-2 and AVN-3, the fracture loads were found to be 1,700 N, 1,695 N and 1,214 N, respectively as shown in Figure 4.12. Their correlated number of accumulated failure elements were 268, 7574 and 59395, respectively. The trend was therefore relatively similar to the normal models. However, the fatigue fracture in the AVN-1 model is just associated with tensile failure as there was no compressive failure elements. The AVN-2 and AVN-3 models, on the other side, showed not only tensile but also compressive fracture with a number of cracked, plastic and crushed element failures. Therefore, it was realized that AVN-1 model achieved its maximum strength before yielding, while the other AVN models got their highest strengths after yielding.

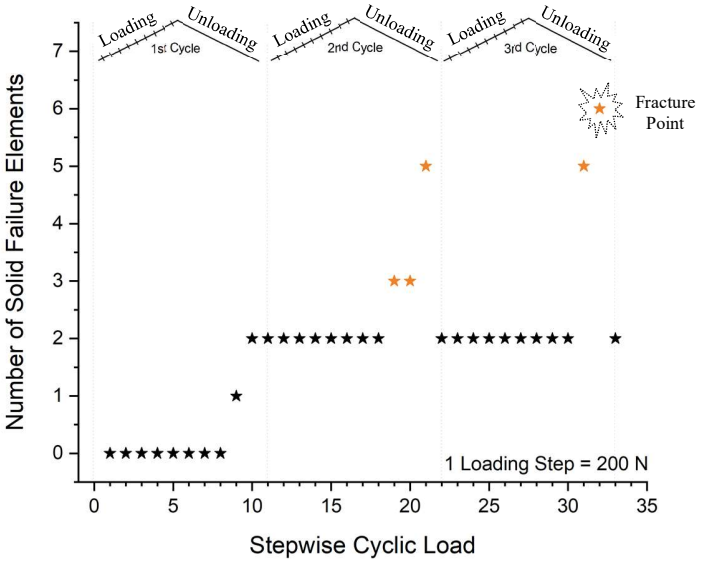

(a) normal-1 model.

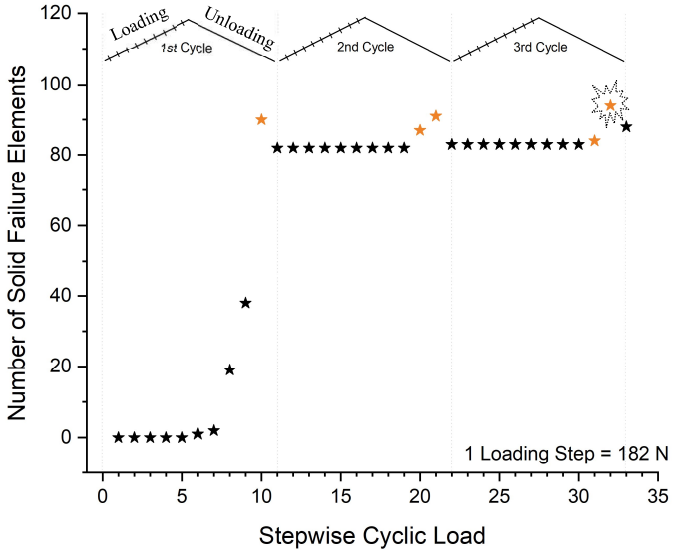

(b) normal-2 model.

Figure 4.10: Investigation for the cyclic strengths of standard normal femora. The black color represents the cracked and/or crushed elements while the orange color corresponds to containing plastic element (yielding).

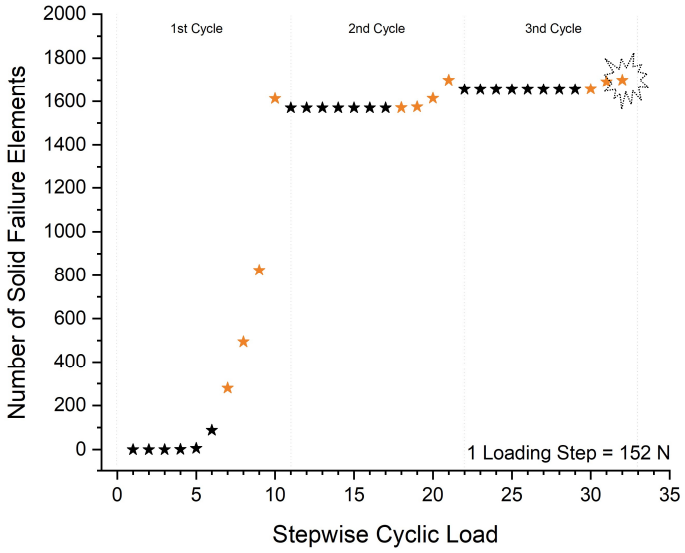

(c) normal-3 model.

Figure 4.10: (Continued).

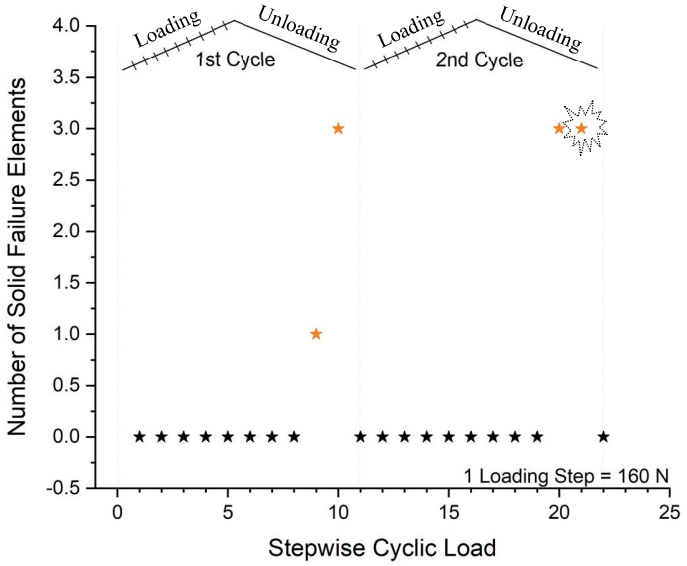

(a) OA-1 model.

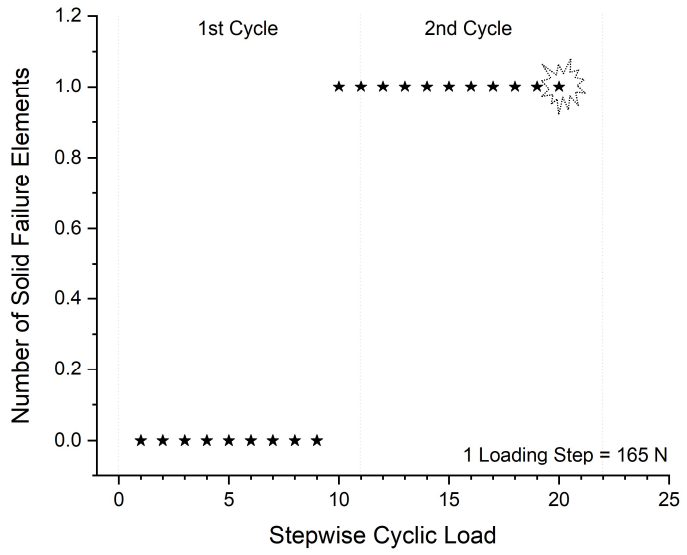

(b) OA-2 model.

Figure 4.11: Investigation for the cyclic strengths of standard OA femora. The black color represents the cracked and/or crushed elements while the orange color corresponds to containing plastic element (yielding).

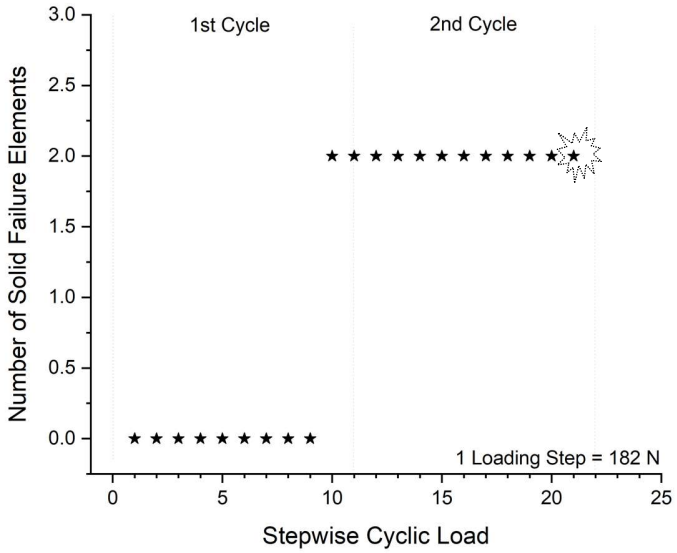

(c) OA-3 model.

Figure 4.11: (Continued).

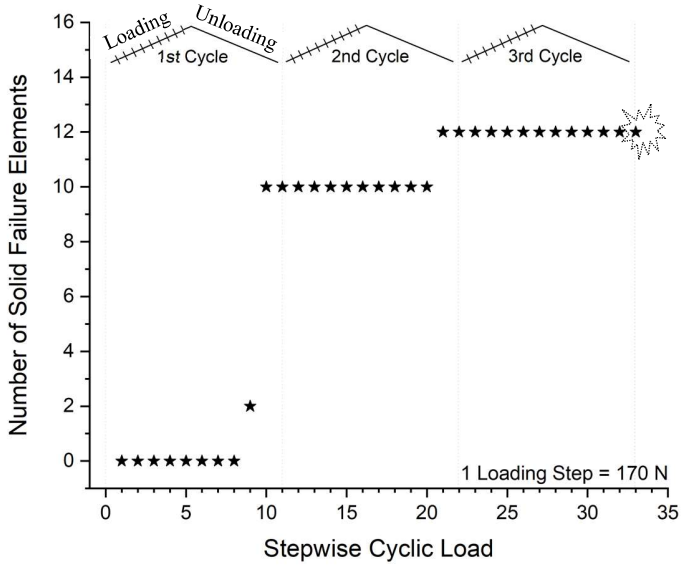

(a) AVN-1 model.

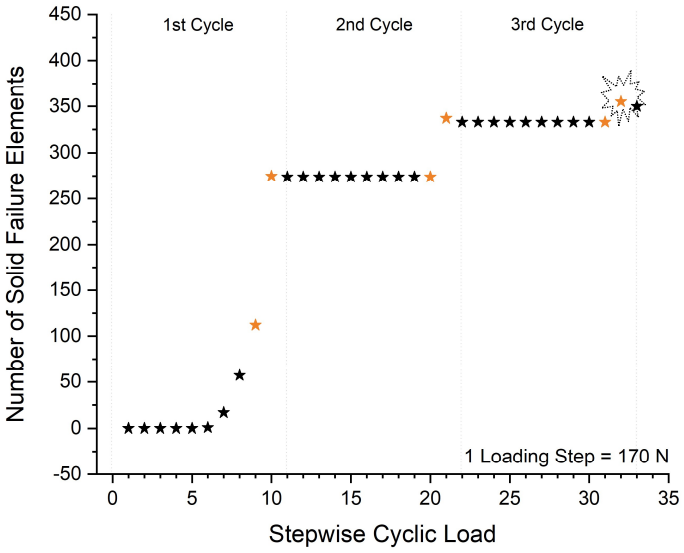

(b) AVN-2 model.

Figure 4.12: Investigation for the cyclic strengths of standard AVN femora. The black color represents the cracked and/or crushed elements while the orange color corresponds to containing plastic element (yielding).

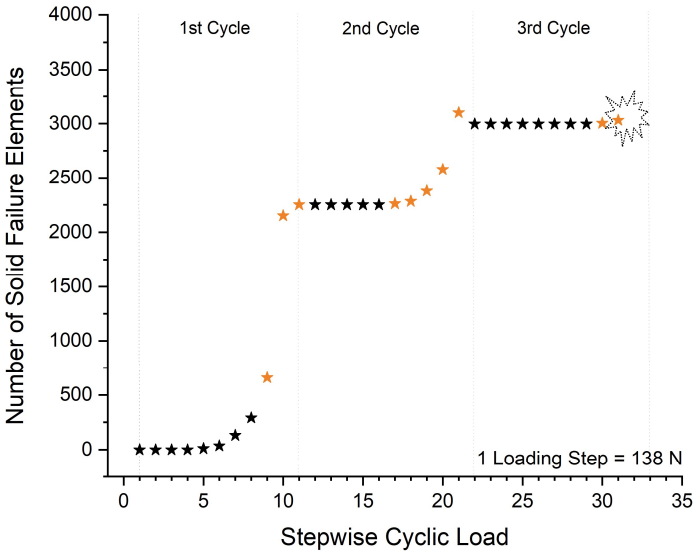

(c) AVN-3 model.

Figure 4.12: (Continued).

4.3.2 Comparison of Fracture Mechanism under the Linear and Cyclic Loading

Under the linear loading analysis, the average fracture strength of three normal femurs was found to be 2,392±559 N (ranged from 1,900 to 3,000 N), whereas the average fracture strength under cyclic loading was of 1,734±317 N (ranged from 1,383 to 2,000 N). It was estimated that the cyclic strength is approximately equal to 0.73 times of the linear strength. In another word, the strength of three standard normal models in previous linear loading analysis decreased to ≈ 27% when they were subjected to cyclic loading.

Similarly, the average linear fracture strength of three OA femurs were 2,525±344 N (ranged from 2,150 to 2,825 N) while the average fracture strength under cyclic

loading was of 1,564±114 N (ranged from 1,436 to 1,656 N). Therefore, the linear strength of the OA models decreased to ≈ 38% in the cyclic loading. For the AVN models, the average linear fracture strength of three AVN femurs were 2,058±213 N (ranged from 1,850 to 2,275 N), whereas the average fracture strength under cyclic loading was of 1,536±279 N (ranged from 1,214 to 1,700 N). It is also noteworthy that the AVN models decreased to ≈ 25% in cyclic process.

To compare the fracture mechanism under linear and cyclic loading analyses, the normal-1, OA-1 and AVN-1 models were selected. Their cross-sectional SED distributions were shown in Figure 4.13, 4.14 and 4.15, respectively. These figures revealed that the SED values were sharply decreased in all cyclic models, indicating the degradation of energy stored in the elements. This is one of the reasons why the load needed for fatigue failure is far less than that for compressive failure in previous linear analysis. Moreover, the compression stress ratios of the models under the linear and cyclic analysis were also displayed in Figure 4.16, 4.17 and 4.18, respectively. These ratios are the ratios of equivalent stress to yield stress and they expressed the location to reach the compressive fracture. It was therefore realized that the compressive stresses of the cyclic models were significantly low due to the progressive and localized damage of the elements inside. Especially in the OA-1 model, this phenomenon was distinct and it could lead to fracture at a smaller number of cycles compared to the other type of models.

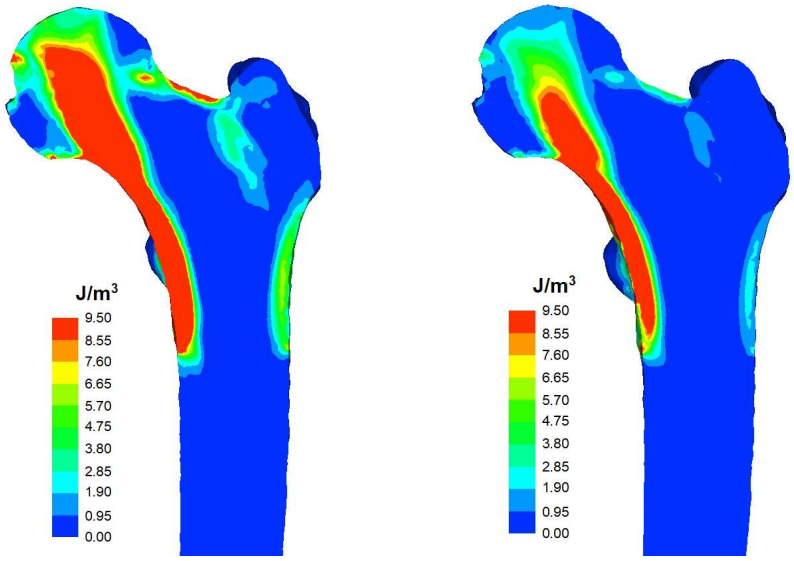

(a) Linear Loading (b) Cyclic Loading

Figure 4.13: SED distributions in the mid-section of the normal-1 model.

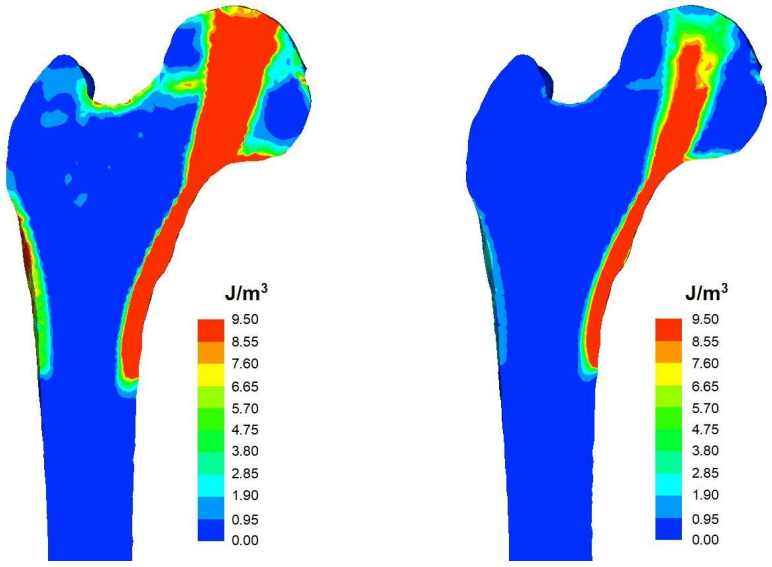

(a) Linear Loading (b) Cyclic Loading

Figure 4.14: SED distributions in the mid-section of the OA-1 model.

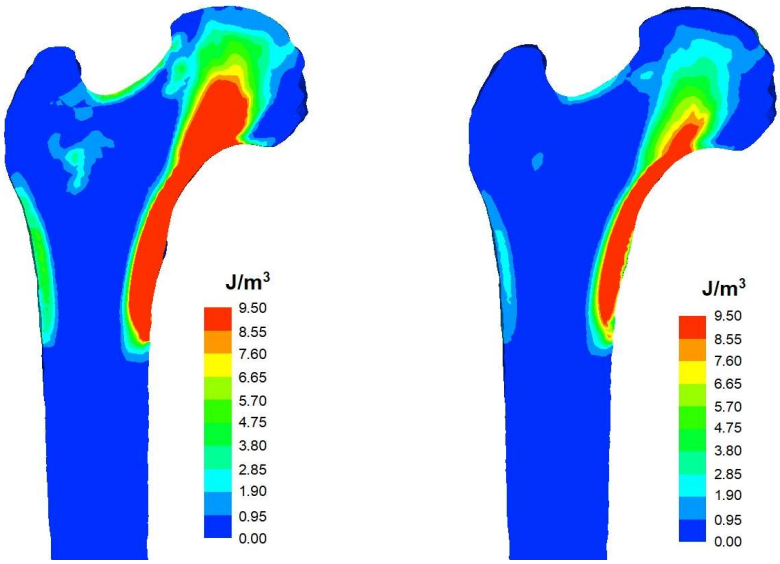

(a) Linear Loading (b) Cyclic Loading

Figure 4.15: SED distributions in the mid-section of the AVN-1 model.

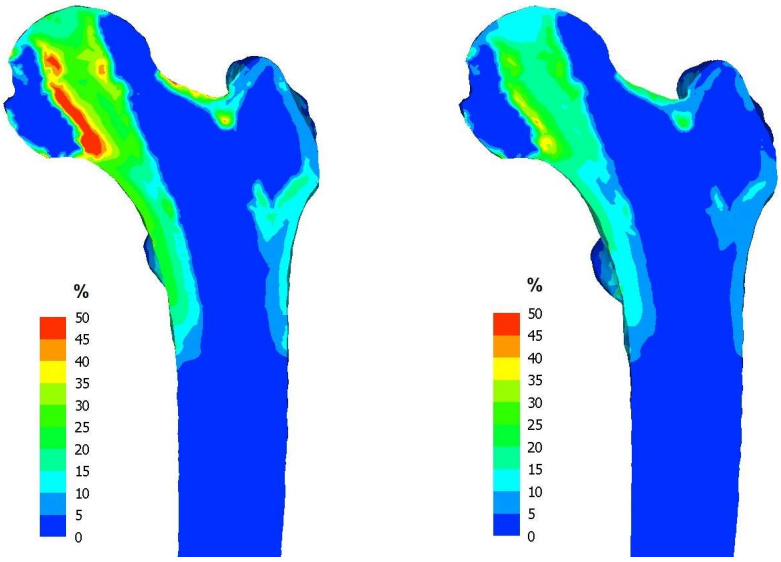

(a) Linear Loading (b) Cyclic Loading

Figure 4.16: Compressive stress ratios of the normal-1 model.

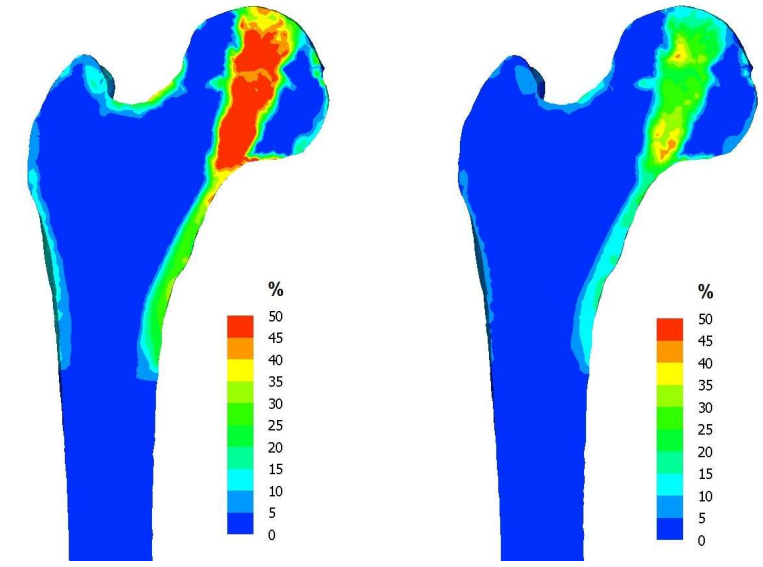

(a) Linear Loading (b) Cyclic Loading

Figure 4.17: Compressive stress ratios of the OA-1 model.

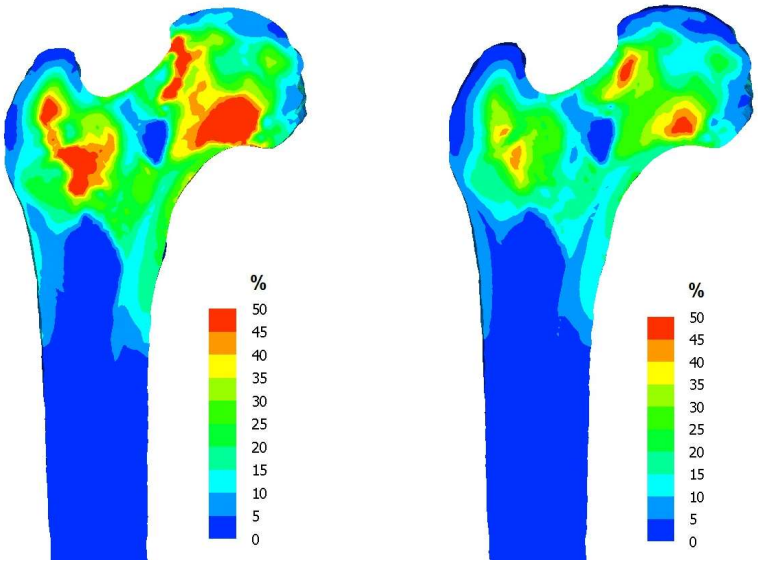

(a) Linear Loading (b) Cyclic Loading

Figure 4.18: Compressive stress ratios of the AVN-1 model.

4.3.3 Failure Element Accumulation under the Linear and Cyclic Loading

For each femoral model, the compressive fracture behaviour was expressed as the distribution of failure elements in the femoral head and neck region. The distributions of failure element in the normal-1, OA-1 and AVN-1 models under linear and cyclic loading were shown in Figure 4.19, 4.20 and 4.21, respectively. Those micro-damages consisted of three different failure modes, that is, tensile fracture, compressive yielding, and compressive fracture.

In the normal-1 model, under linear analysis, the crack and plastic elements were largely distributed on the subcapital portion of the neck area. Besides, a few elements also appeared on the transcervical portion because of high compressive load. However, in

fatigue analysis, only subcapital portion was indicated as potential fracture. The similar characteristics were observed in the OA-1 model, in which plastic failure elements were spotted on the subcapital portion. In the AVN-1 model, on the other hand, fracture locations appeared on transcervical portion and intertrochanteric area under fatigue analysis. Therefore, under a high compression stress (10,000 N load) with 15 shell elements limitation, the solid elements will fail as many as described in corresponding figures (Figure 4.19(a), Figure 4.20(a) and Figure 4.21(a)) with a high-visuality. At here, only fatigue elements resulted from the repeated stresses will fail in the models under cyclic loading (Figure 4.19(b), 4.20(b) and 4.21(b). Moreover, these fatigue failure elements seemed to be more accurately appeared on the fracture site comparing to the compressive failure element under linear loading. It can therefore be said that these elements would be very important for bone fracture sites specification.

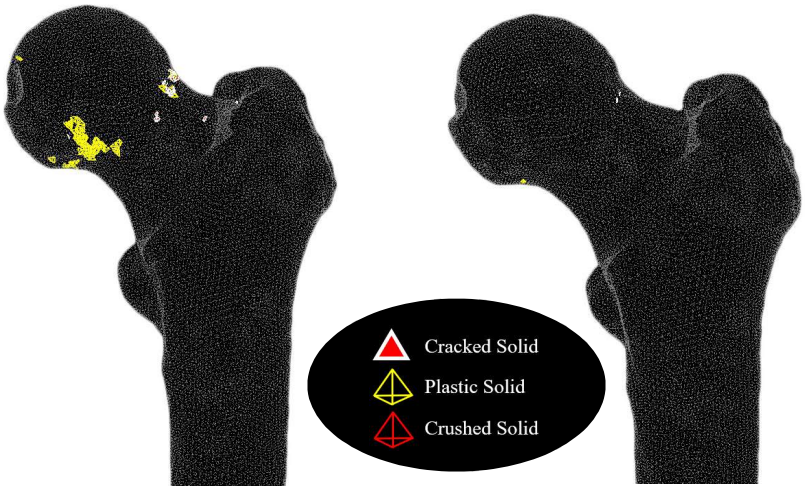

(a) Linear Loading (b) Cyclic Loading

Figure 4.19: Accumulation of failure elements in the normal-1 model.

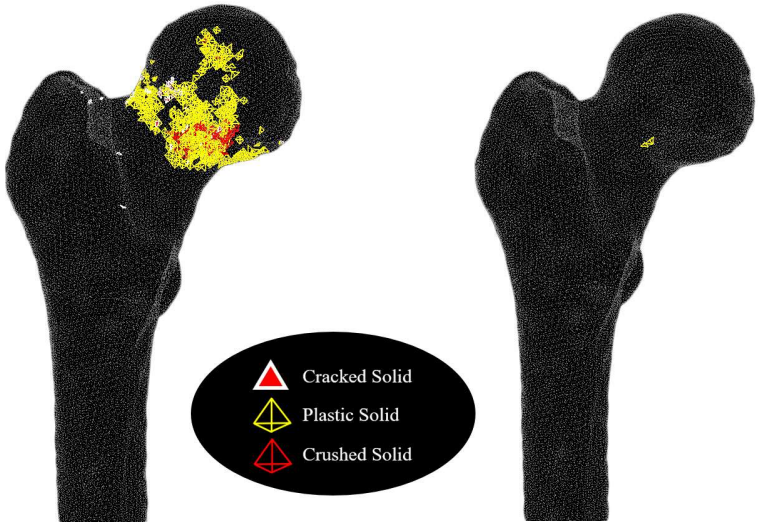

(a) Linear Loading (b) Cyclic Loading

Figure 4.20: Accumulation of failure elements in the OA-1 model.

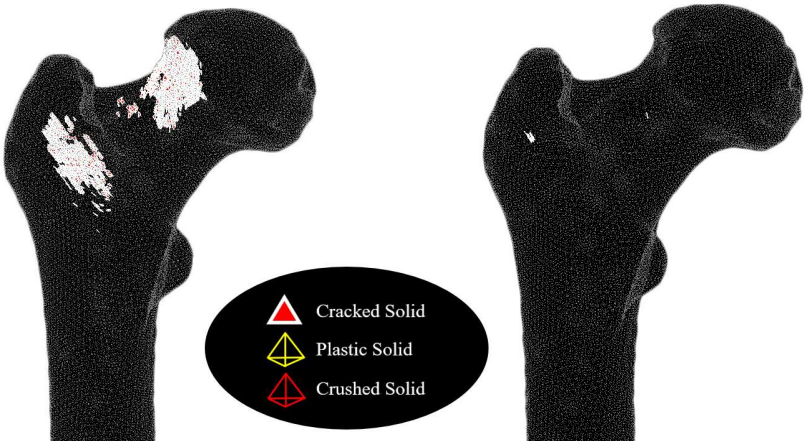

(a) Linear Loading (b) Cyclic Loading

Figure 4.21: Accumulation of failure elements in the AVN-1 model.

4.4 Conclusion

In this study, normal, OA and AVN femoral FE models were analyzed by cyclic/fatigue loading procedure applying FEA, and compared with the previous linear loading analysis. Based on the damage mechanics by FE analysis, the following conclusions can be drawn:

(1) The average cyclic fracture strengths of the standard normal, OA and AVN models of elderly patients were 1734±317 N, 1,564±114 N and 1,536±279 N, respectively. By comparison with linear loading analysis, the strength in cyclic loading significantly decreased to ≈ 27%, 38% and 25% accordingly.

(2) The fracture sites observed in the cyclic loading was congruous with the linear loading. Furthermore, the fatigue failure elements seemed more precisely appeared on the fracture region comparing to the previous compressive failure elements. Therefore, it can also be considered that those elements would be one of the fundamental indicators for consideration of bone fracture sites specifically.

(3) Along with fatigue properties, the FEM femoral models implemented with cyclic loading behaviour could result in more realistic models for real-life applications such as walking in daily activity.

CHAPTER 5

GENERAL CONCLUSION

In this study, CT-image based FE models of the normal, OA and AVN femora were constructed using Mechanical Finder v.11. The inhomogeneous material properties were used for the elements inside the models, and Drucker-Prager yield criterion was applied for compressive deformation. Subsequently, the fracture risks of the models were analyzed by means of compressive loading under stance configuration and sideways falling, as well as cyclic/fatigue loading. The results of this research can be summarized as follows:

1. In chapter 2, the 3D femoral FE models of 130 femurs with healthy (contralateral femur), OA and AVN conditions were constructed from the CT images of lower limbs of 73 patient. To estimate their femoral strengths and the fracture behaviours, the mechanical testing was performed under a compressive loading condition by means of standing position. Such fracture behaviours were recreated as the accumulation of element fracture under both the tensile and compressive stress conditions. The computational results exhibited that the fracture load tended to increase with increasing the volumetric bone mineral density (vBMD) estimated in the femoral head and neck region in all the three types of models, although AVN models showed much wider scatter in the data than the other two types. Regarding bone fracture risk, the fracture behaviour was expressed as appeared in the distribution pattern of failure elements in the head and neck region. Under

stance configuration, the bone fracture mainly took place in the neck region for all types of femoral model. In addition, a combination of the head and neck fracture was also observed in all the models. A combination of neck and intertrochanteric fracture was also observed in the normal and AVN groups.

2. In chapter 3, the above 130 FE models were also performed by means of sideways falling as it was one of the leading causes for hip fracture in elderly people. Along with damage mechanics, the strength and fracture behaviours were also investigated. The computational results exhibited that the fracture load tended to increase with increase of the vBMD as well. Under fall loading, the bone fracture mainly took place in the greater trochanter region for all types of femoral model. Furthermore, a combination of the greater trochanter and multifarious neck fracture was also observed in all the models. A combination of greater trochanter and intertrochanteric fracture was also observed in the AVN group.
3. In chapter 4, the standard FE models of elderly patients were selected form each femoral group (i.e. the normal, OA and AVN) and conducted by cyclic/fatigue loading. The computational results showed that the normal and AVN models could bear the applied load until three cycles of a given loading range, and the average fracture strengths were 1,734±317 N and 1,536±279 N, respectively, indicating a significant decrease from the linear compressive strengths (2,392±559 N and 2,058±213 N). Therefore, the fracture strengths were decreased to ≈ 26% for these models, and it was suggested that the femoral strength in cyclic analysis was ≈ 0.74 times of the previous linear

analysis. However, in the case of OA models, the fracture was occurred at two cycles of applied loading range, and the average fracture load was 1,564±114 N. The average fracture load was largely decreased to ≈ 38%, indicating 0.62 times of previous linear loading. About the fracture location, the potential fracture sites in cyclic models were congruous with the previous linear loading models. Furthermore, fatigue failure elements resulted from repeated stress might be one of the indicators for considering bone fracture sites specifically. Along with fatigue effects, the FEM femoral models implemented with cyclic loading process could produce more realistic models with respect to real-life applications such as walking in daily activity. In addition, the models might also be useful for patient-specific clinical trials and studies.

SUPPLEMENTARY MATERIALS

A: BMD Measurement in the Femoral Head and Neck regions

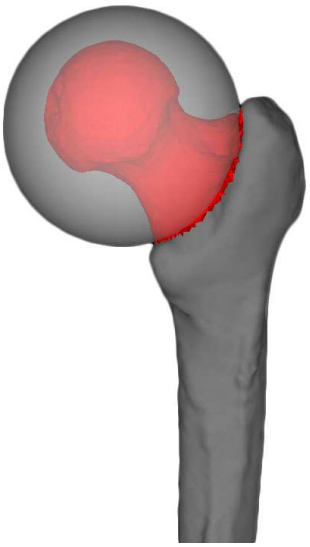

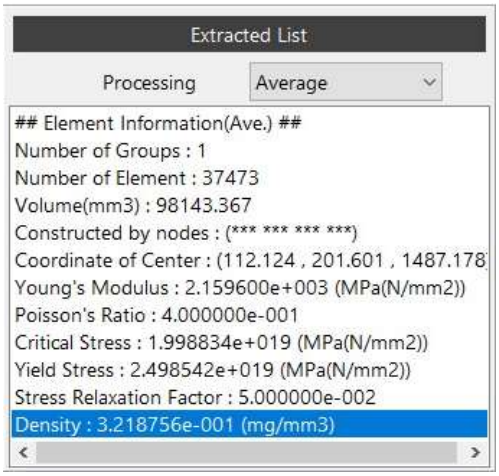

B: Types of Osteonecrosis (AVN)

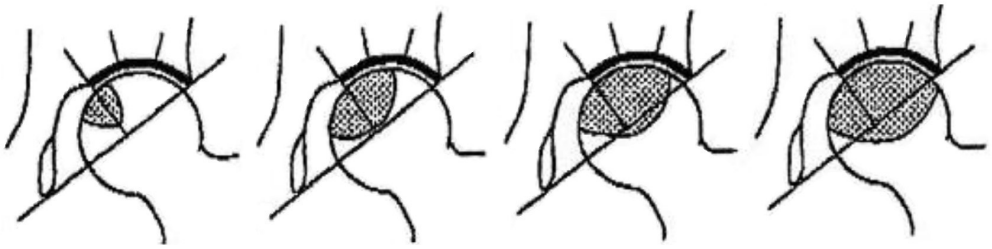

REFERENCES

[1] Chang A, Breeland G, Hubbard JB. Anatomy, Bony Pelvis and Lower Limb, Femur. StatPearls. StatPearls Publishing; 2021.

[2] Standring S, editor. Pelvic Girdle and Lower Limb. In: Gray's Anatomy:The Anatomical Basis of Clinical Practice. 41st ed. Elsevier; 2016.

[3] Drake R, Vogl AW, Mitchell AWM. Gray's Anatomy for Students. 1st ed. Churchill Livingstone; 2004.

[4] Oscar Rodrigo Ariza. A Novel Approach to Finite Element Analysis of Hip Fractures Due To Sideways Falls. University of British Columbia; 2014. https://doi.org/10.14288/1.0166898.

[5] Fox KM, Magaziner J, Hebel JR, Kenzora JE, Kashner TM. Intertrochanteric versus femoral neck hip fractures: Differential characteristics, treatment, and sequelae. Journals of Gerontology-Series A, Biological Sciences and Medical Sciences. 1999;54(12):M635-40. https://doi.org/10.1093/gerona/54.12.M635.

[6] Zuckerman JD. Hip Fracture. New England Journal of Medicine. 1996;334(23): 1519–25. https://doi.org/10.1056/NEJM199606063342307.

[7] Courtney AC, Wachtel EF, Myers ER, Hayes WC. Effects of loading rate on strength of the proximal femur. Calcified Tissue International. 1994;55(1):53–8. https://doi.org/10.1007/BF00310169.

[8] Pinilla TP, Boardman KC, Bouxsein ML, Myers ER, Hayes WC. Impact direction from a fall influences the failure load of the proximal femur as much as age-related bone loss. Calcified Tissue International. 1996;58(4):231–5. https://doi.org/ 10.1007/bf02508641.

[9] Cheng XG, Lowet G, Boonen S, Nicholson PHF, Brys P, Nijs J, Dequeker J. Assessment of the strength of proximal femur in vitro: Relationship to femoral

bone mineral density and femoral geometry. Bone. 1997;20(3):213–8. https://doi.org/10.1016/S8756-3282(96)00383-3.

[10] Bouxsein ML, Szulc P, Munoz F, Thrall E, Sornay-Rendu E, Delmas PD. Contribution of trochanteric soft tissues to fall force estimates, the factor of risk, and prediction of hip fracture risk. Journal of Bone and Mineral Research. 2007;22(6):825–31. https://doi.org/10.1359/jbmr.070309.

[11] Roberts BJ, Thrall E, Muller JA, Bouxsein ML. Comparison of hip fracture risk prediction by femoral aBMD to experimentally measured factor of risk. Bone. 2010;46(3):742–6. https://doi.org/10.1016/j.bone.2009.10.020.

[12] Nawathe S, Akhlaghpour H, Bouxsein ML, Keaveny TM. Microstructural failure mechanisms in the human proximal femur for sideways fall loading. Journal of Bone and Mineral Research. 2014;29(2):507–15. https://doi.org/10.1002/jbmr.2033.

[13] Abraham AC, Agarwalla A, Yadavalli A, McAndrew C, Liu JY, Tang SY. Multiscale Predictors of Femoral Neck in Situ Strength in Aging Women: Contributions of BMD, Cortical Porosity, Reference Point Indentation, and Nonenzymatic Glycation. Journal of Bone and Mineral Research. 2015;30(12):2207–14. https://doi.org/10.1002/jbmr.2568.

[14] Johannesdottir F, Thrall E, Muller J, Keaveny TM, Kopperdahl DL, Bouxsein ML. Comparison of non-invasive assessments of strength of the proximal femur. Bone. 2017;105:93–102. https://doi.org/10.1016/j.bone.2017.07.023.

[15] Rezaei A, Giambini H, Rossman T, Carlson KD, Yaszemski MJ, Lu L, Dragomir-Daescu D. Are DXA/aBMD and QCT/FEA Stiffness and Strength Estimates Sensitive to Sex and Age? Annals of Biomedical Engineering. 2017;45(12):2847–56. https://doi.org/10.1007/s10439-017-1914-5.

[16] Keaveny TM. Biomechanical computed tomography- Noninvasive bone strength analysis using clinical computed tomography scans. Annals of the New York

Academy of Sciences. 2010;1192:57–65. https://doi.org/10.1111/j.1749-6632.2009.05348.x.

[17] Imai K, Ohnishi I, Bessho M, Nakamura K. Nonlinear finite element model predicts vertebral bone strength and fracture site. Spine. 2006;31(16):1789–94. https://doi.org/10.1097/01.brs.0000225993.57349.df.

[18] Graeff C, Chevalier Y, Charlebois M, Varga P, Pahr D, Nickelsen TN, Morlock MM, Glüer CC, Zysset PK. Improvements in vertebral body strength under teriparatide treatment assessed in vivo by finite element analysis: Results from the EUROFORS study. Journal of Bone and Mineral Research. 2009;24(10):1672–80. https://doi.org/10.1359/jbmr.090416.

[19] Osteoarthritis vs Osteoporosis : Different Diseases , Different Treatments [Internet]. [cited 2022 Jun 8]. Available from: https://www.sonoranspine.com/article-layout/97-conditions-and-treatments/diseases-and-conditions/1342-osteoarthritis-vs-osteoporosis-different-diseases-different-treatments

[20] Summa Health - 5 Common Types of Arthritis [Internet]. [cited 2022 Jun 8]. Available from: https://www.summahealth.org/flourish/entries/2019/06/5-common-types-of-arthritis

[21] Kloppenburg M, Berenbaum F. Osteoarthritis year in review 2019: epidemiology and therapy. Osteoarthritis and Cartilage. 2020;28(3):242–8. https://doi.org/10.1016/j.joca.2020.01.002.

[22] Osteoarthritis Research Society International (OARSI). OA as a Serious Disease-White Paper. 2016.

[23] Vestergaard P, Rejnmark L, Mosekilde L. Osteoarthritis and risk of fractures. Calcified Tissue International. 2009;84(4):249–56. https://doi.org/10.1007/s00223-009-9224-z.

[24] Weintroub S, Papo J, Ashkenazi M, Tardiman R, Weissman SL, Salama R. Osteoarthritis of the hip and fractures of the proximal end of the femur. Acta

Orthopaedica. 1982;53(2):261–4. https://doi.org/10.3109/17453678208992213.

[25] Sugano M, Hagiwara S, Nakamura J, Matsuura Y, Suzuki T, Wako Y, Miura M, Kawarai Y, Nawata K, Yoshino K, Konno K, Yoh S, Ohtori S. Comparison study of bone strength of the proximal femur with and without hip osteoarthritis by computed tomography-based finite element analysis. Journal of Biomechanics. 2020;105:109810. https://doi.org/10.1016/j.jbiomech.2020.109810.

[26] Chudyk AM, Ashe MC, Gorman E, Al Tunaiji HO, Crossley KM. Risk of hip fracture with hip or knee osteoarthritis: A systematic review. Clinical Rheumatology. 2012;31(5):749–57. https://doi.org/10.1007/s10067-012-1970-z.

[27] Maluta T, Toso G, Negri S, Samaila EM, Magnan B. Correlation between hip osteoarthritis and proximal femoral fracture site: could it be protective for intracapsular neck fractures? A retrospective study on 320 cases. Osteoporosis International. 2019;30(8):1591–6. https://doi.org/10.1007/s00198-019-05015-5.

[28] Calderazzi F, Groppi G, Ricotta A, Ceccarelli F. Does hip osteoarthritis have a protective effect against proximal femoral fractures? A retrospective study. HIP International. 2014;24(3):231–6. https://doi.org/10.5301/hipint.5000116.

[29] Robstad B, Frihagen F, Nordsletten L. The rate of hip osteoarthritis in patients with proximal femoral fractures versus hip contusion. Osteoporosis International. 2012;23(3):901–5. https://doi.org/10.1007/s00198-011-1628-8.

[30] Dahab KS. Avascular Necrosis [Internet]. Encyclopedia Britannica,. 2022 [cited 2022 Jun 22]. Available from: https://www.britannica.com/science/avascular-necrosis

[31] Mont MA, Jones LC, Hungerford DS. Nontraumatic Osteonecrosis of the Femoral Head: Ten Years Later. The Journal of Bone & Joint Surgery. 2006;88(5):117–1132.

[32] Yoon BH, Mont MA, Koo KH, Chen CH, Cheng EY, Cui Q, Drescher W, Gangji V, Goodman SB, Ha YC, Hernigou P, Hungerford MW, Iorio R, Jo WL, Jones LC,

Khanduja V, Kim HKW, Kim SY, Kim TY, Lee HY, Lee MS, Lee YK, Lee YJ, Nakamura J, Parvizi J, Sakai T, Sugano N, Takao M, Yamamoto T, Zhao DW. The 2019 Revised Version of Association Research Circulation Osseous Staging System of Osteonecrosis of the Femoral Head. Journal of Arthroplasty. 2020;35(4):933–40. https://doi.org/10.1016/j.arth.2019.11.029.

[33] George G, Lane JM. Osteonecrosis of the Femoral Head. Journal of the American Academy of Orthopaedic Surgeons Global research & reviews. 2022;6(5):e21.00176. https://doi.org/10.1302/0301-620x.95b11.32644.

[34] Mont MA, Cherian JJ, Sierra RJ, Jones LC, Lieberman JR. Nontraumatic osteonecrosis of the femoral head: Where do we stand today? A ten-year update. Journal of Bone and Joint Surgery-American Volume. 2014;97(19):1604–27. https://doi.org/10.2106/JBJS.O.00071.

[35] Ikeuchi K, Hasegawa Y, Seki T, Takegami Y, Amano T, Ishiguro N. Epidemiology of nontraumatic osteonecrosis of the femoral head in Japan. Modern Rheumatology. 2015;25(2):278–81. https://doi.org/10.3109/14397595.2014.932038.

[36] Kang JS, Moon KH, Kwon DG, Shin BK, Woo MS. The natural history of asymptomatic osteonecrosis of the femoral head. International orthopaedics. 2013;37:379–84. https://doi.org/10.1007/s00264-013-1775-y.

[37] Chan VWK, Chan PK, Chiu KY, Yan CH, Ng FY. Why do Hong Kong patients need total hip arthroplasty? An analysis of 512 hips from 1998 to 2010. Hong Kong Medical Journal. 2016;22(1):11–5. https://doi.org/10.12809/hkmj144483.

[38] Lai YS, Wei HW, Cheng CK. Incidence of hip replacement among national health insurance enrollees in Taiwan. Journal of Orthopaedic Surgery and Research. 2008;3(42):1–10. https://doi.org/10.1186/1749-799X-3-42.

[39] Lubega N, Mkandawire NC, Sibande GC, Norrish AR, Harrison WJ. Joint replacement in Malawi: Establishment of a national joint registry. Journal of Bone

and Joint Surgery-Series B. 2009;91(3):341–3. https://doi.org/10.1302/0301-620X.91B3.21706.

[40] Mankin HJ. Nontraumatic Necrosis of Bone (Osteonecrosis). New England Journal of Medicine. 1992;326(22):1473–9. https://doi.org/10.1056/nejm199205283262206.

[41] Ancelin D, Reina N, Cavaignac E, Delclaux S, Chiron P. Total hip arthroplasty survival in femoral head avascular necrosis versus primary hip osteoarthritis: Case-control study with a mean 10-year follow-up after anatomical cementless metal-on-metal 28-mm replacement. Orthopaedics and Traumatology: Surgery and Research. 2016;102(8):1029–34. https://doi.org/10.1016/j.otsr.2016.08.021.

[42] Conroy JL, Whitehouse SL, Graves SE, Pratt NL, Ryan P, Crawford RW. Risk Factors for Revision for Early Dislocation in Total Hip Arthroplasty. Journal of Arthroplasty. 2008;23(6):867–72. https://doi.org/10.1016/j.arth.2007.07.009.

[43] Singh JA, Chen J, Inacio MCS, Namba RS, Paxton EW. An underlying diagnosis of osteonecrosis of bone is associated with worse outcomes than osteoarthritis after total hip arthroplasty. BMC Musculoskeletal Disorders. 2017;18(8):1–9. https://doi.org/10.1186/s12891-016-1385-0.

[44] Bahk JH, Jo WL, Kim SC, Kwon SY, Lim YW. Lateral pillar is the key in supporting pre-collapse osteonecrosis of the femoral head: a finite element model analysis of propensity-score matched cohorts. Journal of Orthopaedic Surgery and Research. 2021;16(728):1–6. https://doi.org/10.1186/s13018-021-02875-8.

[45] Huang L, Chen F, Wang S, Wei Y, Huang G, Chen J, Shi J, Naidu RK, Xia J, Tao TH. Three-dimensional finite element analysis of silk protein rod implantation after core decompression for osteonecrosis of the femoral head. BMC Musculoskeletal Disorders. 2019;20(544):1–10. https://doi.org/10.1186/s12891-019-2914-4.

[46] MECHANICAL FINDER: Quantitative CT-based Finite Element Analysis

Software [Internet]. 計算力学研究センター. [cited 2022 May 31]. Available from: https://mechanical-finder.com/

[47] MECHANICAL FINDER: the functions required for Quantitative CT-based Finite Element Analysis [Internet]. 計算力学研究センター. [cited 2022 May 31]. Available from: https://mechanical-finder.com/functions/

[48] Keyak JH, Skinner HB, Fleming JA. Effect of force direction on femoral fracture load for two types of loading conditions. Journal of Orthopaedic Research. 2001;19(4):539–44. https://doi.org/10.1016/S0736-0266(00)00046-2.

[49] Wu S, Todo M, Umebayashi D, Yamamoto Y. Risk assessment of vertebral compressive fracture using bone mass index and strength predicted by computed tomography image based finite element analysis. Clinical Biomechanics (Bristol, Avon). 2021;85:105365. https://doi.org/10.1016/j.clinbiomech.2021.105365.

[50] Htun ZL, Todo M. Computational Study on Femoral Fracture using CT-Image based Finite Element Method. Proceedings of International Exchange and Innovation Conference on Engineering & Sciences (IEICES). 2021;7:58–63. https://doi.org/10.5109/4738567.

[51] Miura M, Nakamura J, Matsuura Y, Wako Y, Suzuki T, Hagiwara S, Orita S, Inage K, Kawarai Y, Sugano M, Nawata K, Ohtori S. Prediction of fracture load and stiffness of the proximal femur by CT-based specimen specific finite element analysis: Cadaveric validation study. BMC Musculoskeletal Disorders. 2017;18(536):1–8. https://doi.org/10.1186/s12891-017-1898-1.

[52] Nishi K, Endo D, Hasegawa T, Moriuchi T, Ogami-Takamura K, Saiki K, Murai K, Higashi T, Tsurumoto T, Manabe Y, Oyamada J. Similarities and Differences in Bone Mineral Density between Multiple Sites in the Same Individual: An Elderly Cadaveric Study. Du J, editor. BioMed Research International. 2022;2022(Article ID 6094663):1–10. https://doi.org/10.1155/2022/6094663.

[53] Bessho M, Ohnishi I, Matsuyama J, Matsumoto T, Imai K, Nakamura K.

Prediction of strength and strain of the proximal femur by a CT-based finite element method. Journal of Biomechanics. 2007;40(8):1745–53. https://doi.org/10.1016/j.jbiomech.2006.08.003.

[54] Bessho M, Ohnishi I, Matsumoto T, Ohashi S, Matsuyama J, Tobita K, Kaneko M, Nakamura K. Prediction of proximal femur strength using a CT-based nonlinear finite element method: Differences in predicted fracture load and site with changing load and boundary conditions. Bone. 2009;45(2):226–31. https://doi.org/10.1016/j.bone.2009.04.241.

[55] Engelke K, van Rietbergen B, Zysset P. FEA to Measure Bone Strength: A Review. Clinical Reviews in Bone and Mineral Metabolism. 2016;14:26–37. https://doi.org/10.1007/s12018-015-9201-1.

[56] Keaveny TM, Kopperdahl D, Melton L, Hoffmann P, Amin S, Riggs B, Khosla S. Age-Dependence of Femoral Strength in White Women and Men. Journal of Bone and Mineral Research. 2009;25(5):994–1001. https://doi.org/10.1359/jbmr.091033.

[57] Keyak JH, Rossi SA, Jones KA, Skinner HB. Prediction of femoral fracture load using automated finite element modeling. Journal of Biomechanics. 1997;31(2):125–33. https://doi.org/10.1016/S0021-9290(97)00123-1.

[58] Roberts BJ, Kopperdahl D, Thrall E, Muller JA, Keaveny TM, Bouxsein ML. Prediction of femoral strength in a sideways fall configuration using QCT-based finite element analysis. Bone. 2009;44(Supplement 1):S72. https://doi.org/10.1016/j.bone.2009.01.158.

[59] Dall'Ara E, Luisier B, Schmidt R, Kainberger F, Zysset P, Pahr D. A nonlinear QCT-based finite element model validation study for the human femur tested in two configurations in vitro. Bone. 2013;52(1):27–38. https://doi.org/10.1016/j.bone.2012.09.006.

[60] Dragomir-Daescu D, Salas C, Uthamaraj S, Rossman T. Quantitative computed tomography-based finite element analysis predictions of femoral strength and

stiffness depend on computed tomography settings. Journal of Biomechanics. 2015;48(1):153–61. https://doi.org/10.1016/j.jbiomech.2014.09.016.

[61] Crolet JM, Aoubiza B, Meunier A. Compact bone: Numerical simulation of mechanical characteristics. Journal of Biomechanics. 1993;26(6):677–87. https://doi.org/10.1016/0021-9290(93)90031-9.

[62] Hollister SJ, Kikuchi N. Homogenization theory and digital imaging: A basis for studying the mechanics and design principles of bone tissue. Biotechnology and Bioengineering. 1994;43(7):586–96. https://doi.org/10.1002/bit.260430708.

[63] Zysset PK, Curnier A. A 3D damage model for trabecular bone based on fabric tensors. Journal of Biomechanics. 1996;29(12):1549–58. https://doi.org/10.1016/S0021-9290(96)80006-6.

[64] Keyak JH, Lee IY, Skinner HB. Correlations between orthogonal mechanical properties and density of trabecular bone: Use of different densitometric measures. Journal of Biomedical Materials Research. 1994;28(11):1329–36. https://doi.org/10.1002/jbm.820281111.

[65] Keller TS. Predicting the compressive mechanical behavior of bone. Journal of Biomechanics. 1994;27(9):1159–68. https://doi.org/10.1016/0021-9290(94)90056-6.

[66] Koivumäki JEM, Thevenot J, Pulkkinen P, Kuhn V, Link TM, Eckstein F, Jämsä T. Ct-based finite element models can be used to estimate experimentally measured failure loads in the proximal femur. Bone. 2012;50(4):824–9. https://doi.org/10.1016/j.bone.2012.01.012.

[67] Crawford RP, Cann CE, Keaveny TM. Finite element models predict in vitro vertebral body compressive strength better than quantitative computed tomography. Bone. 2003;33(4):744–50. https://doi.org/10.1016/S8756-3282(03) 00210-2.

[68] Martin H, Werner J, Andresen R, Schober HC, Schmitz KP. Noninvasive Assessment of Stiffness and Failure Load of Human Vertebrae from CT-Data.

Biomedical Technique (Berl). 1998;43(4):82–8. https://doi.org/10.1515/bmte.1998.43.4.82.

[69] Dall'Ara E, Schmidt R, Pahr D, Varga P, Chevalier Y, Patsch J, Kainberger F, Zysset P. A nonlinear finite element model validation study based on a novel experimental technique for inducing anterior wedge-shape fractures in human vertebral bodies in vitro. Journal of Biomechanics. 2010;43(12):2374–80. https://doi.org/10.1016/j.jbiomech.2010.04.023.

[70] Buckley JM, Loo K, Motherway J. Comparison of quantitative computed tomography-based measures in predicting vertebral compressive strength. Bone. 2007;40(3):767–74. https://doi.org/10.1016/j.bone.2006.10.025.

[71] Zysset PK, Dall'Ara E, Varga P, Pahr DH. Finite element analysis for prediction of bone strength. BoneKEy Reports. 2013;2:386. https://doi.org/10.1038/bonekey.2013.120.

[72] National Institute of Population and Social Security Research 2017 [Internet]. Population projections for Japan (January 2017). [cited 2022 Jun 8]. Available from: https://www.ipss.go.jp/index-e.asp

[73] Lang TF, Keyak JH, Heitz MW, Augat P, Lu Y, Mathur A, Genant HK. Volumetric quantitative computed tomography of the proximal femur: Precision and relation to bone strength. Bone. 1997;21(1):101–8. https://doi.org/10.1016/S8756-3282(97)00072-0.

[74] Ulrich D, van Rietbergen B, Weinans H, Rüegsegger P. Finite element analysis of trabecular bone structure: A comparison of image-based meshing techniques. Journal of Biomechanics. 1998;31(12):1187–92. https://doi.org/10.1016/S0021-9290(98)00118-3.

[75] Dalstra M, Huiskes R, van Erning L. Development and validation of a three-dimensional finite element model of the pelvic bone. Journal of Biomechanical Engineering. 1995;117(3):272–8. https://doi.org/10.1115/1.2794181.

[76] Hirata Y, Inaba Y, Kobayashi N, Ike H, Yukizawa Y, Fujimaki H, Tezuka T, Tateishi U, Inoue T, Saito T. Correlation between mechanical stress by finite element analysis and 18f-fluoride pet uptake in hip osteoarthritis patients. Journal of Orthopaedic Research. 2015;33(1):78–83. https://doi.org/10.1002/jor.22717.

[77] Miyamura S, Oka K, Abe S, Shigi A, Tanaka H, Sugamoto K, Yoshikawa H, Murase T. Altered bone density and stress distribution patterns in long-standing cubitus varus deformity and their effect during early osteoarthritis of the elbow. Osteoarthritis and Cartilage. 2018;26(1):72–83. https://doi.org/10.1016/j.joca. 2017.10.004.

[78] Kitamura K, Fujii M, Utsunomiya T, Iwamoto M, Ikemura S, Hamai S, Motomura G, Todo M, Nakashima Y. Effect of sagittal pelvic tilt on joint stress distribution in hip dysplasia: A finite element analysis. Clinical Biomechanics. 2020;74:34–41. https://doi.org/10.1016/j.clinbiomech.2020.02.011.

[79] Abdullah AH, Todo M, Nakashima Y. Prediction of damage formation in hip arthroplasties by finite element analysis using computed tomography images. Medical Engineering and Physics. 2017;44:8–15. https://doi.org/10.1016/ j.medengphy.2017.03.006.

[80] Sato T, Yonezawa I, Todo M, Takano H, Kaneko K. Biomechanical Effects of Implant Materials on Posterior Lumbar Interbody Fusion: Comparison of Polyetheretherketone and Titanium Spacers Using Finite Element Analysis and Considering Bone Density. Journal of Biomedical Science and Engineering. 2018;11(04):45–59. https://doi.org/10.4236/jbise.2018.114005.

[81] Oba M, Kobayashi N, Inaba Y, Choe H, Ike H, Kubota S, Saito T. Mechanical Strength of the Proximal Femur After Arthroscopic Osteochondroplasty for Femoroacetabular Impingement: Finite Element Analysis and 3-Dimensional Image Analysis. Arthroscopy - Journal of Arthroscopic and Related Surgery. 2018;34(8):2377–86. https://doi.org/10.1016/j.arthro.2018.03.036.

[82] Murphey MD, Roberts CC, Bencardino JT, Appel M, Arnold E, Chang EY,

Dempsey ME, Fox MG, Fries IB, Greenspan BS, Hochman MG, Jacobson JA, Mintz DN, Newman JS, Rosenberg ZS, Rubin DA, Small KM, Weissman BN. ACR Appropriateness Criteria Osteonecrosis of the Hip. Journal of the American College of Radiology. 2016;13(2):147–55. https://doi.org/10.1016/j.jacr.2015.10.033.

[83] Grisso JA, Kelsey JL, Strom BL, Ghiu GY, Maislin G, O'Brien LA, Hoffman S, Kaplan F. Risk Factors for Falls as a Cause of Hip Fracture in Women. New England Journal of Medicine. 1991;324(19):1326–31. https://doi.org/10.1056/nejm199105093241905.

[84] Nevitt MC, Cummings SR, Kidd S, Black D. Risk Factors for Recurrent Nonsyncopal Falls: A Prospective Study. JAMA: The Journal of the American Medical Association. 1989;261(18):2663–8. https://doi.org/10.1001/jama.1989.03420180087036.

[85] Abdullah AH, Todo M, Nakashima Y, Iwamoto Y. Risk of Femoral Bone Fractures in Hip Arthroplasties during Sideway Falls. International Journal of Applied Physics and Mathematics. 2014;4(4):286–9. https://doi.org/10.7763/ijapm.2014.v4.300.